Defense Threat Reduction Agency
8725 John J. Kingman Road, MS
6201 Fort Belvoir, VA 22060-6201

DTRA-TR-17-21

TECHNICAL REPORT

Fragmentation of Solid Materials Using Shock Tubes. Part 1: First Test Series in a Small-Diameter Shock Tube

Distribution Statement A. Approved for public release; distribution is unlimited.

January 2017

HDTRA1-14-C-0001

Bryan Bewick, et al.

Prepared by:
Protection Engineering Consultants
P.O. Box 781607
San Antonio, TX 78278

DESTRUCTION NOTICE:

Destroy this report when it is no longer needed.
Do not return to sender.

PLEASE NOTIFY THE DEFENSE THREAT REDUCTION AGENCY, ATTN: DTRIAC/ J9STT, 8725 JOHN J. KINGMAN ROAD, MS-6201, FT BELVOIR, VA 22060-6201, IF YOUR ADDRESS IS INCORRECT, IF YOU WISH IT DELETED FROM THE DISTRIBUTION LIST, OR IF THE ADDRESSEE IS NO LONGER EMPLOYED BY YOUR ORGANIZATION.

REPORT DOCUMENTATION PAGE

Form Approved
OMB No. 0704-0188

Public reporting burden for this collection of information is estimated to average 1 hour per response, including the time for reviewing instructions, searching existing data sources, gathering and maintaining the data needed, and completing and reviewing this collection of information. Send comments regarding this burden estimate or any other aspect of this collection of information, including suggestions for reducing this burden to Department of Defense, Washington Headquarters Services, Directorate for Information Operations and Reports (0704-0188), 1215 Jefferson Davis Highway, Suite 1204, Arlington, VA 22202-4302. Respondents should be aware that notwithstanding any other provision of law, no person shall be subject to any penalty for failing to comply with a collection of information if it does not display a currently valid OMB control number. **PLEASE DO NOT RETURN YOUR FORM TO THE ABOVE ADDRESS.**

1. REPORT DATE *(DD-MM-YYYY)*	**2. REPORT TYPE**	**3. DATES COVERED** *(From - To)*
00-01-2017	Technical	N/A

4. TITLE AND SUBTITLE

Fragmentation of Solid Materials Using Shock Tubes. Part 1: First Test Series in a Small-Diameter Shock Tube

5a. CONTRACT NUMBER
HDTRA1-14-C-0001

5b. GRANT NUMBER

5c. PROGRAM ELEMENT NUMBER

6. AUTHOR(S)

Bryan Bewick (a), Greg Rolater (a), Joeny Bui (a), Matt Barsotti (a), Adam Ziemba (b), Mohsen Sanai (b) and Culbert Laney (c)

5d. PROJECT NUMBER

5e. TASK NUMBER

5f. WORK UNIT NUMBER

7. PERFORMING ORGANIZATION NAME(S) AND ADDRESS(ES)

(a) Protection Engineering Consultants, PO Box 781607, San Antonio, TX 78278
(b) SRI International, 333 Ravenswood Ave., Menlo Park, CA 94025
(c) Engility Corporation, 8211 Terminal Road, Suite 1000, Lorton, VA 22079

8. PERFORMING ORGANIZATION REPORT NUMBER

9. SPONSORING / MONITORING AGENCY NAME(S) AND ADDRESS(ES)

Defense Threat Reduction Agency
8725 John J. Kingman Road, STOP 6201
Fort Belvoir, VA 22060-6201

10. SPONSOR/MONITOR'S ACRONYM(S)
DTRA

11. SPONSOR/MONITOR'S REPORT NUMBER(S)
DTRA-TR-17-21

12. DISTRIBUTION / AVAILABILITY STATEMENT

Distribution Statement A. Approved for public release; distribution is unlimited.

13. SUPPLEMENTARY NOTES

14. ABSTRACT

This report describes a series of tests that used an explosively-driven small-diameter shock tube to shatter simply-supported plates with relatively high-pressure, long-duration blast loads. To determine how the fragment size distribution changed with time due to, e.g., collisions between the fragments and the collector, the fragment size distribution was measured at three different times using three different techniques. Despite the wide of range test conditions, all of the tests in this series, surprisingly, produced a single universal mass distribution, after normalizing by the average fragment mass, to within the limited resolution of the measurement and analysis techniques used.

15. SUBJECT TERMS

fragmentation, size distributions, velocity distributions, Weibull distributions

16. SECURITY CLASSIFICATION OF:			**17. LIMITATION OF ABSTRACT**	**18. NUMBER OF PAGES**	**19a. NAME OF RESPONSIBLE PERSON**
a. REPORT	**b. ABSTRACT**	**c. THIS PAGE**	UU	128	MAJ Jayna Reichert
Unclassified	Unclassified	Unclassified			**19b. TELEPHONE NUMBER** *(include area code)* 703-767-6934

UNIT CONVERSION TABLE

U.S. customary units to and from international units of measurement*

U.S. Customary Units	Multiply by → / ← Divide by†		International Units
Length/Area/Volume			
inch (in)	2.54	$\times 10^{-2}$	meter (m)
foot (ft)	3.048	$\times 10^{-1}$	meter (m)
yard (yd)	9.144	$\times 10^{-1}$	meter (m)
mile (mi, international)	1.609 344	$\times 10^{3}$	meter (m)
mile (nmi, nautical, U.S.)	1.852	$\times 10^{3}$	meter (m)
barn (b)	1	$\times 10^{-28}$	square meter (m^2)
gallon (gal, U.S. liquid)	3.785 412	$\times 10^{-3}$	cubic meter (m^3)
cubic foot (ft^3)	2.831 685	$\times 10^{-2}$	cubic meter (m^3)
Mass/Density			
pound (lb)	4.535 924	$\times 10^{-1}$	kilogram (kg)
unified atomic mass unit (amu)	1.660 539	$\times 10^{-27}$	kilogram (kg)
pound-mass per cubic foot (lb ft^{-3})	1.601 846	$\times 10^{1}$	kilogram per cubic meter (kg m^{-3})
pound-force (lbf avoirdupois)	4.448 222		newton (N)
Energy/Work/Power			
electron volt (eV)	1.602 177	$\times 10^{-19}$	joule (J)
erg	1	$\times 10^{-7}$	joule (J)
kiloton (kt) (TNT equivalent)	4.184	$\times 10^{12}$	joule (J)
British thermal unit (Btu) (thermochemical)	1.054 350	$\times 10^{3}$	joule (J)
foot-pound-force (ft lbf)	1.355 818		joule (J)
calorie (cal) (thermochemical)	4.184		joule (J)
Pressure			
atmosphere (atm)	1.013 250	$\times 10^{5}$	pascal (Pa)
pound force per square inch (psi)	6.984 757	$\times 10^{3}$	pascal (Pa)
Temperature			
degree Fahrenheit (^oF)	$[T(^oF) - 32]/1.8$		degree Celsius (^oC)
degree Fahrenheit (^oF)	$[T(^oF) + 459.67]/1.8$		kelvin (K)
Radiation			
curie (Ci) [activity of radionuclides]	3.7	$\times 10^{10}$	per second (s^{-1}) [becquerel (Bq)]
roentgen (R) [air exposure]	2.579 760	$\times 10^{-4}$	coulomb per kilogram (C kg^{-1})
rad [absorbed dose]	1	$\times 10^{-2}$	joule per kilogram (J kg^{-1}) [gray (Gy)]
rem [equivalent and effective dose]	1	$\times 10^{-2}$	joule per kilogram (J kg^{-1}) [sievert (Sv)]

*Specific details regarding the implementation of SI units may be viewed at http://www.bipm.org/en/si/.

†Multiply the U.S. customary unit by the factor to get the international unit. Divide the international unit by the factor to get the U.S. customary unit.

EXECUTIVE SUMMARY

The test series described here is part of an overall effort to develop a probabilistic, physics-based model for the fragmentation of building components. More specifically, this report describes tests on plates constructed from conventional façade construction materials, in which fragment distributions for mass, size, and velocity were measured.

This test series used a small-diameter explosively-driven shock tube to shatter simply-supported plate samples with relatively high-pressure, long-duration blast loads. Shock tubes have rarely, if ever, been used to systematically study fragmentation prior to this work. One limitation is a tradeoff between high overpressures and extended durations. This test series favors high overpressures. Companion studies in a larger shock tube favor long durations. Another limitation is that placing test articles inside small shock tubes risks ejecting the test articles whole, almost regardless of support technique, rather than fragmenting them. This test series used a novel 'punch out' technique, wherein the test article was mounted outside the shock tube. In other words, the test articles were made deliberately larger than the shock tube diameter, to allow for a simple external support structure. The test setup was designed to preferentially capture fragments originating from the shock-loaded circular center of the target.

The first objective of this test series was to explore how a wide range of large strain rates affects fragment size and velocity distributions. The second objective was to explore how changing materials – including tempered glass, concrete, and concrete masonry (CMU) – affects fragment size and velocity distributions. The third objective was to explore how fragment size distributions change with time due to, e.g., collisions between the fragments and the collector.

In pursuit of the third objective, the fragment size distribution was measured at three different times using three different techniques. More specifically, a high-speed video (HSV) camera was used to record the initial crack pattern on the rear face of each sample, a second HSV camera was used to capture the fragment sizes and velocities in-flight at intermediate times, and finally the late-time at-rest fragments were physically collected and analyzed post-test. Because this test series physically collected over 50,000 fragments, it was not possible to weigh each fragment by hand. Instead, a new technique was developed, which combines sieving, shadowgraphy, and digital image processing.

These tests were performed in SRI International's 6.5-in-diameter 37-ft long shock tube. In these tests, 2-in-thick specimens of precast concrete and concrete masonry units (CMU) were subjected to three different pressure-time histories with peak pressures of approximately 4,000 psi, 3,000 psi, and 1,500 psi. In addition, ¼-in-thick plate tempered glass specimens were subjected to two different pressure-time histories with peak pressures of approximately 250 psi and 500 psi.

Despite the wide of range test conditions, all of the tests in this series, surprisingly, produced a single universal mass distribution, after normalizing by the average fragment mass, to within the limited resolution of the measurement and analysis techniques used.

Contents

Figures

Tables

1 BACKGROUND

This report is the first in a four part series. In brief, the four parts are as follows:

- Part 1 *(this report)*: Measured fragment size distributions, velocity size distributions, and the time-dependency of fragment size distributions in a large number of different small-scale tests.
- Part 2. Measured fragment size distributions in a small number of different large-scale tests. Showed that, in some cases, the size distributions obtained at small scales in Part 1 also occur at large scales.
- Part 3. Measured fragment size distributions in a large number of different small-scale tests. Increased the range of test conditions to obtain a wider variety of fragment size distributions than in Part 1. In particular, modified the experimental techniques used in Part 1 to allow for higher-pressures and increased fragment sample sizes.
- Part 4. Measured fragment size distributions in a small number of different large-scale tests. Building on Part 2, obtained further evidence that the size distributions obtained at small scales in Parts 1 and 3 also occur at large scales.

All of these tests used explosively-driven shock tubes. Shock tubes have rarely, if ever, been used to systematically study fragmentation prior to this work. Parts 1 and 3 used a small (6.5-in diameter) shock tube to load square plates with relatively short-duration high-overpressure airblast, creating conditions where material properties (e.g., strength, density) dominate structural response (e.g., bending, flexing). Part 2 and 4 used a large (8 ft diameter) shock tube to load realistic building façade panels and roofing sections with relatively long-duration low-overpressure air blast, creating conditions where structural response dominates material properties.

1.1 PURPOSE AND SCOPE

This test series used a small explosively-driven shock tube to shatter simply-supported plate samples using relatively high-pressure, long-duration blast loads. Placing test articles inside small shock tubes risks ejecting the test articles whole, almost regardless of support technique, rather than fragmenting them. This test series used a novel ‘punch out’ technique, wherein the test article was mounted outside the shock tube. In other words, the test articles were made deliberately larger than the shock tube diameter, to allow for a simple exterior support structure. The test setup included a fragment stripper designed to preferentially capture fragments originating from the uniformly-shock-loaded circular center of the target.

This test series was performed in SRI International’s 6.5-in-diameter 37-ft long shock tube. The shock tube was used to fragment 2-in-thick specimens of precast concrete and concrete masonry unit (CMU) material using three different pressure-time histories with peak pressures of approximately 4,000 psi, 3,000 psi, and 1,500 psi. In addition, the shock tube was used to fragment ¼-in-thick plate tempered glass specimens using two different pressure-time histories with peak pressures of approximately 250 psi and 500 psi.

1.2 TESTING OBJECTIVES

The first goal of this test series was to explore how fragment size and velocity distributions depend on blast loads or, equivalently, strain rates. The second goal was to explore how fragment size and velocity distributions depend on material type. The third goal was to explore how fragment size distributions change with time due to, e.g., mid-air collisions between fragments.

As part of the first goal, LS-DYNA was used to make pre-test predictions for the strain rate; see Appendix B. More specifically, LS-DYNA was used to predict the velocity gradients that were, in turn, used to calculate the strain rates through the thickness of the test sample. The through-thickness strain rates were then averaged to get an average strain rate. For example, Figure 1 shows LS-DYNA predictions for the average strain rate vs. applied peak reflected overpressure for concrete and tempered glass test articles. Based on these predictions, and the pressure loads achievable in the shock tube, this test series obtained strain rates ranging between 10^2 sec^{-1} and $8x10^3$ sec^{-1}.

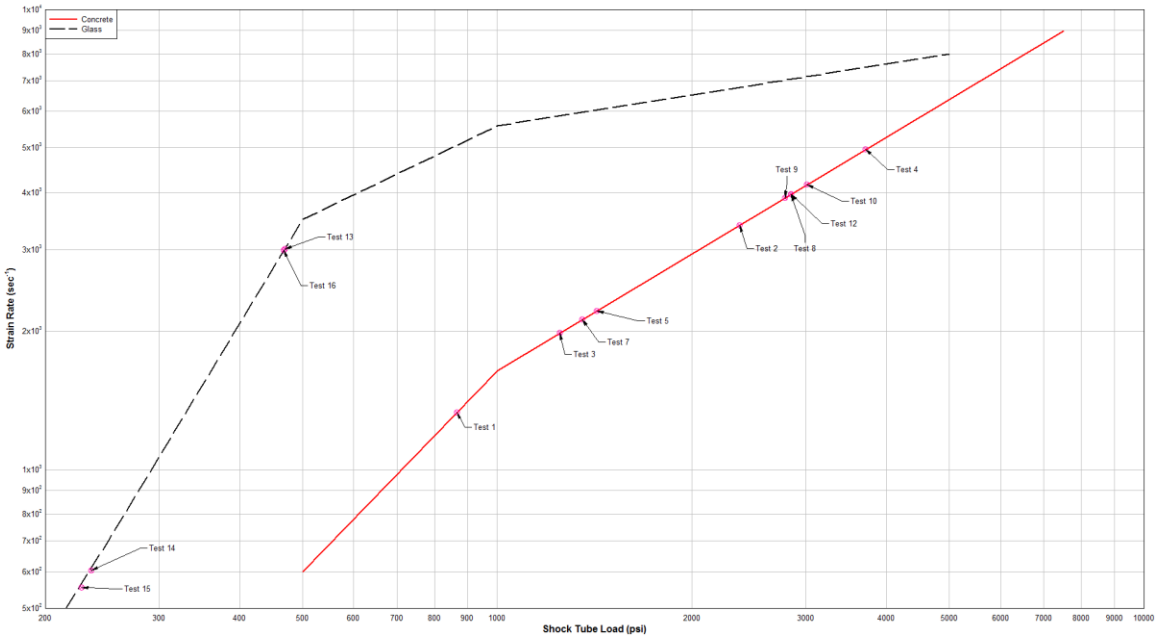

Figure 1. LS-DYNA pre-test predictions for average strain rates in concrete and tempered glass test articles.

2 TESTING OVERVIEW

As previously noted, these tests were performed in SRI International's 6.5-in-diameter 37-ft long shock tube, which is located at SRI's privately owned Corral Hollow Experiment Site (CHES).

To determine how the fragment size distribution changed with time, the fragment size distribution was measured at three different times using three different techniques. In particular, a high-speed video (HSV) camera was used to record the initial crack pattern on the rear face of each sample, a second HSV camera was used to record the fragment sizes and velocities in-flight at intermediate times, and finally the late-time at-rest fragments were physically collected and analyzed post-test. Because this test series physically collected over 50,000 fragments, it was not possible to weigh the fragments by hand. Instead, a new technique was developed, which combined sieving, shadowgraphy, and digital image processing techniques.

Table 1 summarizes the 16 tests completed in this series. Tests 1, 2, and 11 were conducted strictly for purposes of test design and calibration. In other words, only 13 tests in the series were analyzed.

Table 1. Small diameter shock tube experiment parameters.

Test	Sample	Sample Thickness[1] (in)	Charge Type	Charge Length (in)	Charge Mass (g)	Peak Reflected Overpressure (psi)		Approximate Duration (ms)		Impulse (psi-ms)		Strain Rate (sec^{-1})
						East[2]	West[2]	East[2]	West[2]	East[2]	West[2]	
1	Concrete (checkout)	2	3600 gr/ft Primacord	24	467	N/A	866.5	N/A	4.6	N/A	1502.3	$1.33x10^3$
2	Concrete (checkout)	2	3600 gr/ft Primacord	24	467	N/A	2371.8	N/A	6.0	N/A	2626	$3.4x10^3$
3	CMU	2.125	1-in dia Comp B	22	481	1259.3	1240.5	12.3	10.0	2909.1	1867.1	$1.98x10^3$
4	CMU	2.0625	1.75-in dia Comp B	24.125	1579	3603.7	3816.0	21.0	23.0	5514.1	5123.9	$4.97x10^3$
5	Concrete	2	1-in dia Comp B	24.1875	486	1423.2	1425.1	11.2	12.6	2096.4	2007.0	$2.21x10^3$
6	Concrete	1.9375	1.75-in dia Comp B	24.1125	1581	N/A[3]	N/A[3]	N/A[3]	N/A[3]	N/A[3]	N/A[3]	N/A[3]
7	CMU	2.0625	1-in dia Comp B	21	462	1347.3	1358.4	13.1	14.3	1932.0	1901.8	$2.12x10^3$
8	Concrete	2	1.5-in dia Comp B	21.375	1042	2972.5	2722.4	8.7	13.0	3264.5	3511.4	$3.97x10^3$
9	Concrete	2	1.5-in dia Comp B	20.5	994	2932.6	2632.9	N/A[3]	10.8	N/A[3]	3267.1	$3.89x10^3$
10	CMU	2.09375	1.5-in dia Comp B	20.5	993	3167.4	2849.2	11.0	12.0	4054.9	2963.6	$4.16x10^3$
11	Fixed Steel Load Plate	1.5	1-in dia Comp B	22.375	486	1775.5	1828.5	49.1	53.5	4624.7	4991.1	N/A
12	CMU	2.125	1.5-in dia Comp B	24	1167	2782.3	2908.2	11.5	17.3	4009.6	3992.3	$3.97x10^3$
13	Tempered Glass	0.22	1200 gr/ft Primacord	24	155.5	477.6	460.9	11.8	11.3	666.7	643.6	$3.02x10^3$
14	Tempered Glass	0.22	450 gr/ft Primacord	24	78	235.4	235.7	9.3	9.1	340.2	339.0	$6.03x10^2$
15	Tempered Glass	0.22	450 gr/ft Primacord	24	78	223.9	230.9	9.1	9.2	325.6	326.0	$5.55x10^2$
16	Tempered Glass	0.22	1200 gr/ft Primacord	24	155.5	485.5	450.0	11.4	11.2	639.6	618.9	$3.00x10^3$

[1] All test sample were 16-in x 16-in plates with varying thickness
[2] Gages located 1.5-in from the samples inside the shock tube on the East or West
[3] Partial or full loss of test data due to instrumentation triggering or sampling failures

Three materials were tested in this series: concrete, CMU material, and tempered glass. The concrete samples were produced by a contractor using a 3,000-psi mix developed by the US Army Corps of Engineers and designated as SAM-35 [1]. The CMU samples were produced using an off-the-shelf normal weight, 4,000-psi mix poured and provided by Pacific Supply [2]. The tempered glass was an off-the-shelf fully tempered single pane produced by C.R. Laurence, Co. [3] and cut to size by a local glass shop in Livermore, CA [4].

Table 2 shows the test sample material properties. As seen in Appendix C, the concrete and CMU values are derived from compression testing. The tempered glass values are typical [5].

Table 2. Test sample material properties.

Material Type	Density (pcf)	Compressive Strength (psi)	Elastic Modulus (psi)	Tensile Strength (psi)	G_f (lbs/in)
Concrete	131	3,120	2.76×10^6	419	0.34
CMU	125	4,470	3.08×10^6	501	0.40
Tempered Glass	161	13,500	10.0×10^6	13,500	0.047

2.1 TEST SETUP

Testing began with two preliminary checkout tests with concrete samples. In these two tests, the side-view HSV was heavily obscured by smoke and fireball. In subsequent tests, significant improvements in camera view and fragment flight observations were achieved by: (a) purging the shock tube with pure nitrogen before each shot; (b) cleaning the soot and combustible residue left from previous shots; (c) securing the charge with non-combustible materials; and (d) adjusting the camera location and lighting. To further improve the camera view, the length of the shock tube was increased from 22-ft to 40-ft., which delayed the arrival of detonation products. For the tempered glass specimens, Primacord charges were used. For the concrete and CMU specimens, cast Comp B charges were used. Cast Comp B eliminated combustible materials, such as the plastic jacket of the Primacord, which otherwise would contribute to smoke formation. Figure 2 shows the test setup used for Tests 3 to 16, after the above improvements were made.

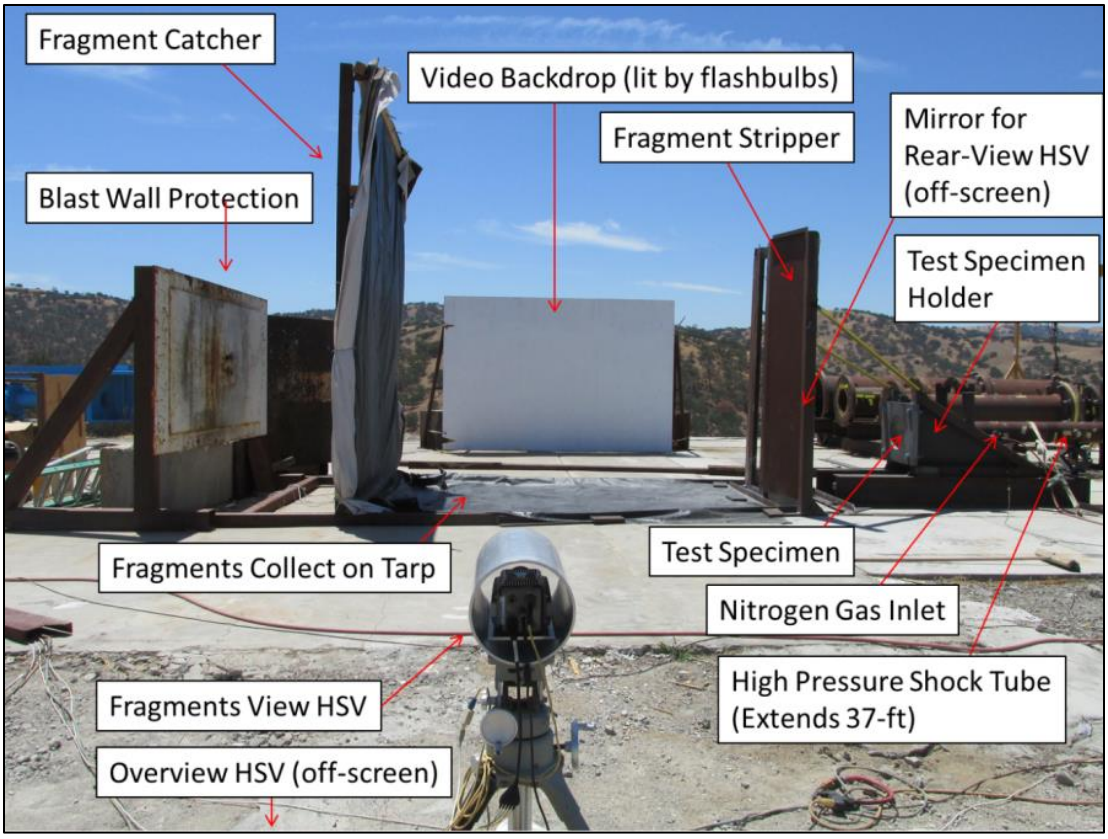

Figure 2. High pressure shock tube test setup used for Tests 3 to 16.

As shown in Figure 2, a mirror and a HSV camera were used to record the early-time fracture patterns on the rear face of each sample. For example, Figure 3 shows the rear face of the tempered glass sample in Test 14. For ¼-in.-thick tempered glass, most of the fragments form in two dimensions in clear view of the camera. Thus the rear-view HSV can be used to estimate the early-time fragment size distributions for glass. By contrast, for the 2-in-thick concrete and CMU, most of the fragments form in three-dimensions and, thus, out-of-view of the camera. In other words, the rear-view HSV cannot be used to estimate the early-time fragment size distributions for concrete and CMU, at least not without some way of extrapolating from the visible surface to the interior.

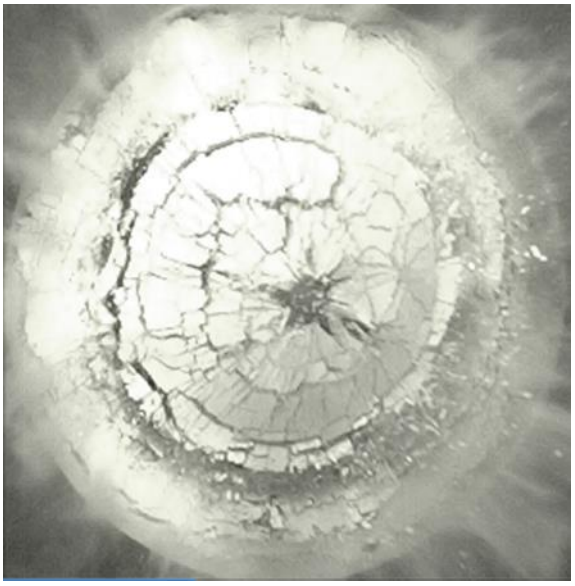

Figure 3. Rear-view HSV capture of tempered glass fracture in Test 14.

As shown in Figure 2 and Figure 4, a fragment stripper and side-view HSV camera were used to record the intermediate-time in-flight fragments. The opening in the fragment stripper was 10-ft tall by 1-ft wide. Located 5-ft from downstream from the sample, the fragment stripper excluded fragments traveling at angles greater than 5° relative to a vertical plane passing through the midsection of the test article. As its main benefit, the fragment stripper made it easy to estimate fragments sizes and speeds, by ensuring that fragments maintained a known fixed distance from the side-view-HSV camera. As a secondary benefit, the fragment stripper tended to admit fragments originating from the directly-loaded center of the sample and, conversely, tended to eliminate fragments originating from the perimeter of the sample. In other words, the fragment stripper selected fragments formed under relatively simple steady uniform loading conditions, a useful feature for future model validation and calibration.

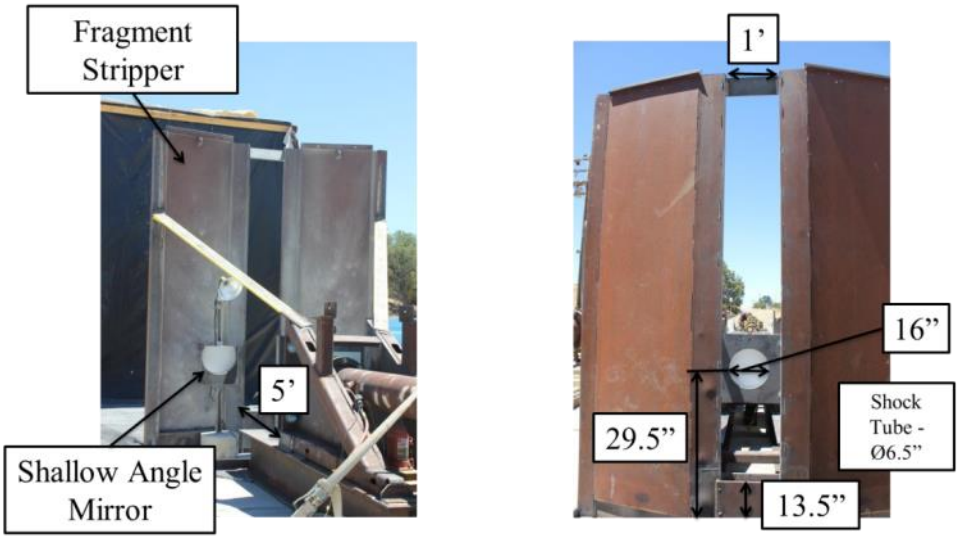

Figure 4. Fragment stripper details.

As seen in Figure 5, a fiduciary video was produced by recording markings of known fixed lengths, placed in the vertical plane in the center of the fragment stripper, using the side-view HSV camera. As described in Section 3.2.1, the fiduciary video led to a simple conversion factor between the number of video pixels and the physical location and dimension of each fragment observed in the side-view HSV.

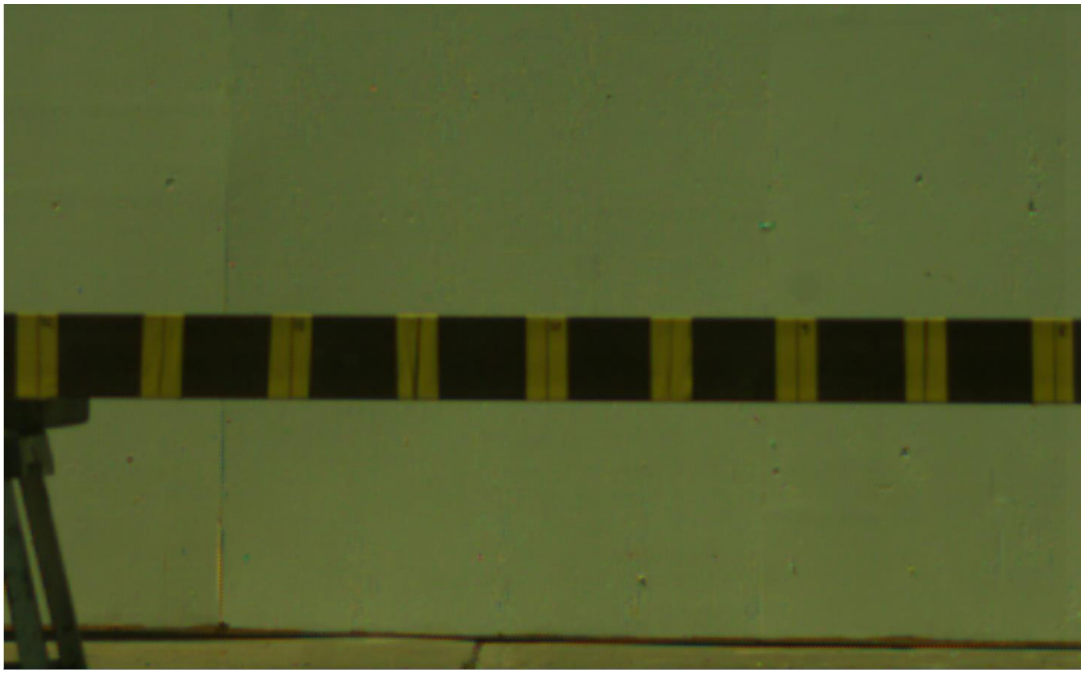

Figure 5. Fiduciary video screen capture.

As shown in Figure 2, the late-time fragments were physically collected using a soft-catcher system, consisting of alternating layers of carpet and Kevlar mounted on a vertical steel frame, with enough layers used to prevent penetration. The soft-catcher system directed the fragments into a collection area, consisting of a heavy-duty tarp mounted on a horizontal steel angle frame, welded to the fragment stripper and laying on the ground. After each experiment, the fragments that landed in the collection area (i.e., on the framed tarp) were collected and weighed. Fragments that landed outside of the collection area (i.e. on the concrete pad or the ground) were collected and discarded.

As noted earlier, a total of 16 tests were performed, where two were preliminary design experiments and one was a load check experiment with a rigid steel plate. In the latter test, a rigid steel plate was bolted to the end of the shock tube, and the pressure was measured for comparison with other cases where the blockage was shattered.

The remaining 13 experiments involved five CMU targets, four precast concrete targets, and four tempered glass targets. Each target was a 16-in x 16-in plate. However, as seen in Figure 6 and Figure 7, the small diameter shock tube loaded only by a 6.5-in-diameter circular area located in the center of each plate. The target plates were placed against a simple steel support on one side and the end of the shock tube on the other side, with only a foam spacer intervening. While the test objects shattered completely in all cases, those parts of the test objects not directly exposed to

the airblast, i.e., outside of the 6.5-in-diameter center circular region, tended to travel off-axis and were thus preferentially eliminated by the fragment stripper. Perimeter fragments with large upward or downward velocity components sometimes passed through the stripper. However, they were easily identified in the side-view HSV and were not measured. In other words, the results are dominated by material punched out from the center of the target, which traveled nearly perpendicular to the plate surface, in the direction of the airblast.

Figure 6. CMU samples before (left) and after (right) being mounted in the supports.

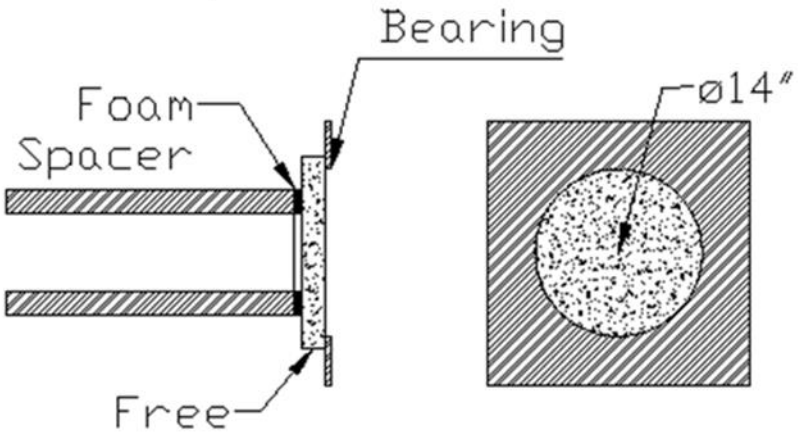

Figure 7. Test target material support conditions.

In all cases, long cylindrical explosive charges were used to create extended airblast durations, while still obtaining the desired high overpressures on the targets. The precast concrete and CMU samples were exposed to three overpressure levels, referred to here as high, medium, and low. The high overpressures were obtained by employing a 1.75-inch-diameter 24.1-inch-long cast Comp B explosive charge that weighed 3.48 lbs (1.58 kg) resulting in a peak reflected static overpressure of ~4,000 psi and a duration of ~10 ms. The medium overpressures were obtained by employing a 1.5-inch-diameter 20.5 to 24-inch-long cast Comp B explosive charge (Figure 8) that weighed between 2.18 lbs (0.99 kg) and 2.58 lbs (1.17 kg) and resulted in a peak reflected static overpressure of ~3,000 psi and a duration of ~8 ms. The low overpressures were obtained by employing a 1-inch-diameter 21 to 22.4-inch-long cast Comp B explosive charge that weighed

between 1.01 lbs (0.46 kg) and 1.06 lbs (0.48 kg) and resulted in a peak reflected static overpressure of ~1,500 psi and a duration of ~5 ms.

Figure 8. Comp B explosive charge and driver section.

The tempered glass samples were exposed to two overpressure levels, referred to here as high and low. These overpressures were obtained by using multiple 24-inch-long strands of either 150 grain/ft or 400 grain/ft Primacord that were reverse-initiated by an RP80 detonator located at the end closest to the target. The high overpressure tests obtained peak incident static overpressures of 500 psi. The low overpressure tests obtained peak incident static overpressures of 250 psi. In all cases, the durations were between 8 and 10 ms.

Pressure was measured using Kulite strain-gaged diaphragm pressure transducers with a range of 60 ksi for the CMU and precast concrete samples and 2 ksi for the tempered glass samples. These pressure gages were placed in strategic locations to characterize the loading environment along the length of the shock tube. For example, Figure 9 shows the pressure-time history measured in Test 12, a medium-pressure CMU test at a pressure gage located 3.25-in upstream from the face of the test sample. Pressure gages were placed on either side of the shock tube, i.e., the East and West side as denoted in Table 1. Data from the pressure gages were collected using a Nicolet Odyssey Data Acquisition System. Appendix C gives a full set of pressure measurements.

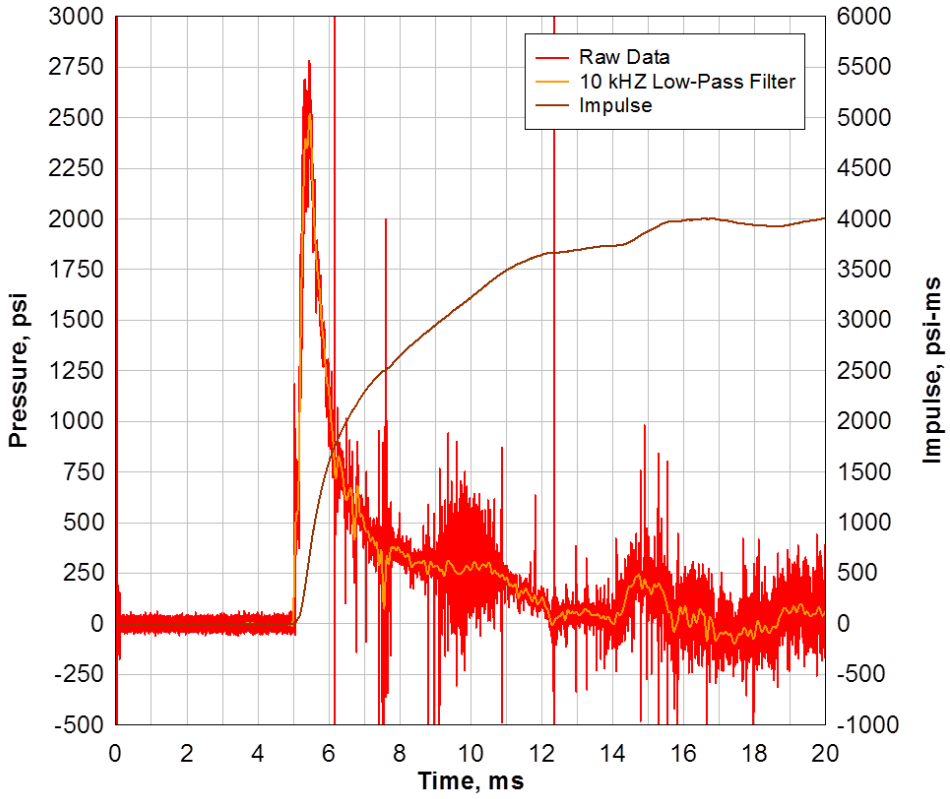

Figure 9. Test 12 (medium-pressure CMU) pressure and impulse histories from a 60-ksi Kulite pressure gage located 3.25-in upstream of the test specimen.

3 FRAGMENT DISTRIBUTION ANALYSIS TECHNIQUES

As seen in Figure 10, two digital image processing software tools were used to characterize debris size and velocity distributions. Frag Track, a custom tool developed by PEC, was used to estimate fragment sizes and velocities from the side-view HSV. SigmaScan, a well-known commercial image analysis package, was used to estimate fragment sizes from the rear-review HSV and from digital photographs of the physically-collected debris.

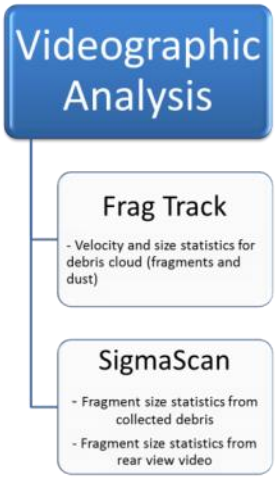

Figure 10. Two digital image processing software tools were used to characterize fragment size and velocity.

3.1 ANALYSIS OF EARLY-TIME REAR-VIEW HIGH-SPEED VIDEOS

Selected frames from the rear-face high-speed video from the tempered glass tests were analyzed using SigmaScan. The selected frames were pre-processed to subtract the background and to outline the fragments monochromatically. SigmaScan was then used to assess the images and output a tabular CSV file of fragment count and area. As noted earlier, rear-face videos are of less value for the concrete and CMU tests, since these fragments form volumetrically in three-dimensions, meaning most are hidden from view.

Figure 11 shows an example of SigmaScan analysis of the rear-face HSV. In the upper right, fragments are identified and outlined. In the lower left, the background is removed. In the lower right, SigmaScan assigns numbers and as-measured properties to each identified fragment. Of the four tempered glass tests, SigmaScan analysis was successfully completed only for Tests 13, 15, and 16. Due to lighting and exposure issues, the rear-face HSV for Test 14 was too blurry to support SigmaScan analysis.

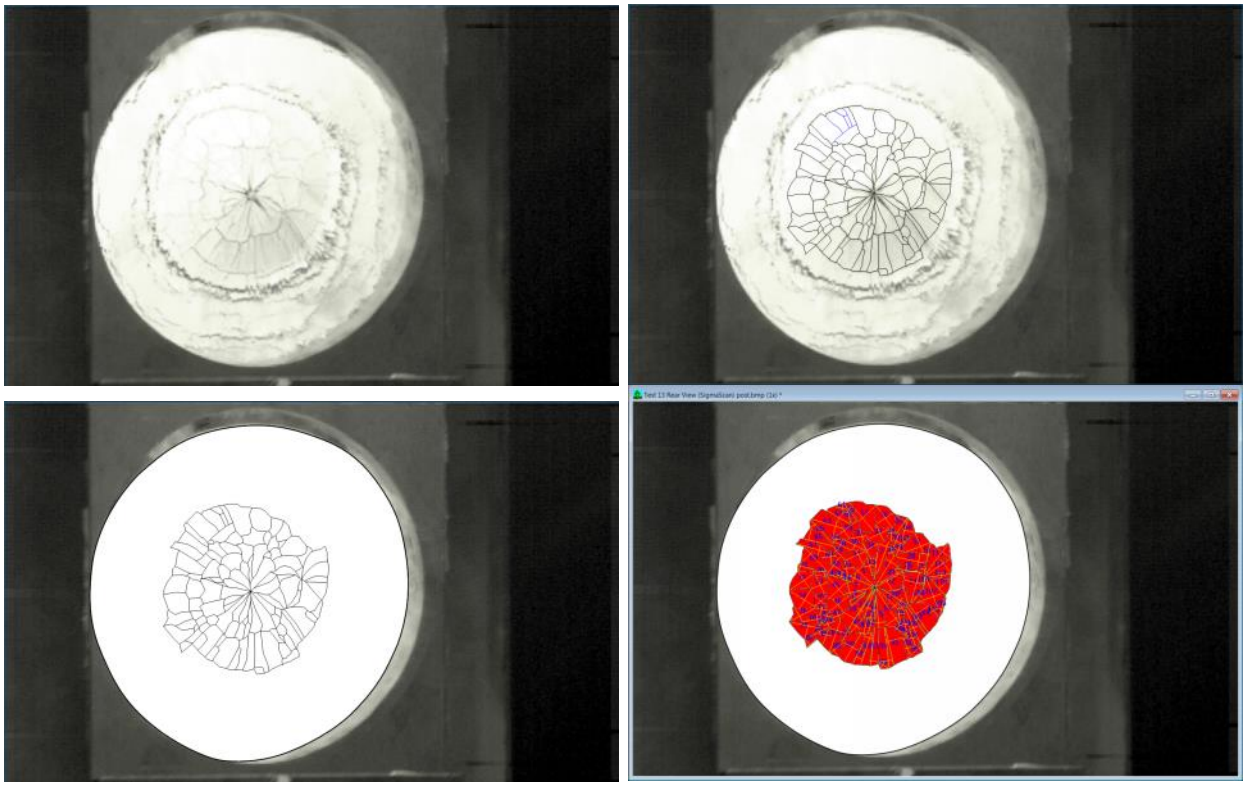

Figure 11. Progression of image analysis for size distribution using SigmaScan Pro for Test 13.

3.2 ANALYSIS OF MID-TIME SIDE-VIEW HIGH-SPEED VIDEOS

3.2.1 FRAG TRACK ANALYSIS METHODOLOGY

Frag Track was designed to estimate debris cloud velocities, whether or not it was possible to clearly distinguish separate fragments.

Frag Track has two main options, one for low and one for high obscuration conditions. The first option was used for the tempered glass tests, which included only low levels of smoke and fire. The second option was used for the concrete and CMU tests which included elevated levels of smoke and fire.

The first option requires the user to select a reference frame. The algorithm then tracks anything that is not part of the reference frame. Unfortunately, this option tracks any and all differences from the reference frame, meaning there is no way to reliably distinguish fragments from smoke and flame. Figure 12 illustrates the first option.

Figure 12. The first Frag Track option.

The second option uses velocity gradients to identify and track individual objects. More specifically, this option looks for closed surfaces with velocity gradients on all sides, which allows it to clearly distinguish fragments from smoke and flame. As an additional advantage, the second option allows Frag Track to estimate fragment sizes in addition to velocities, where the size estimates are based on 2D pixel counts. Figure 13, Figure 14, and Figure 15 illustrate the second option. To exclude fragments that ricochet from the ground or other surfaces, the second option excludes fragments with excessively large vertical velocities.

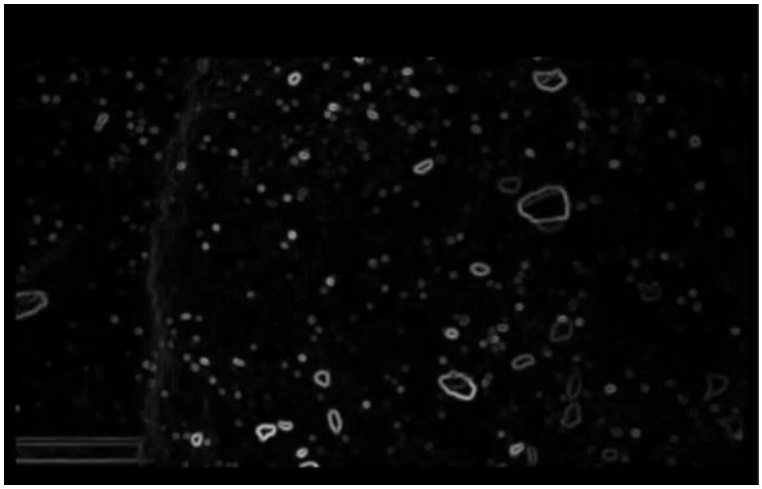

Figure 13. The second Frag Track option looks for velocity gradients.

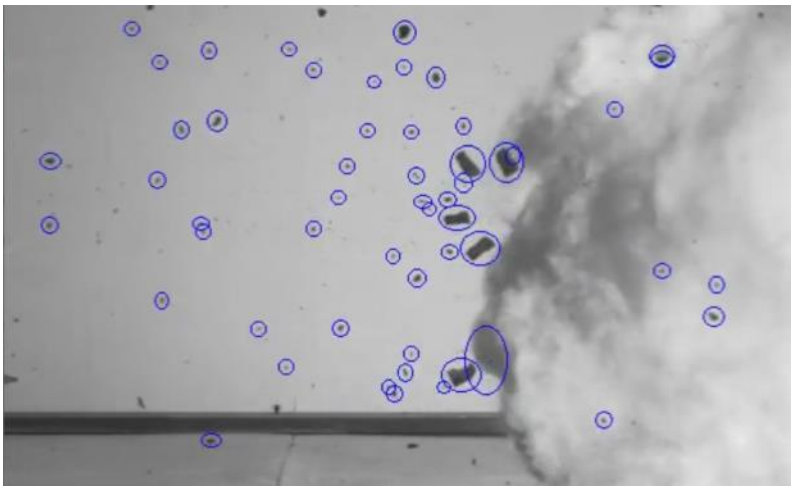

Figure 14. In the second option, Frag Track detects a fragment if velocity gradients form a closed surface.

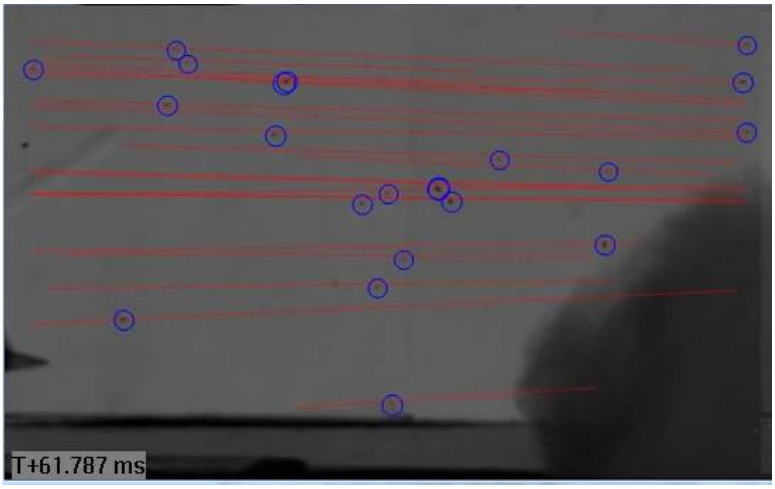

Figure 15. In the second option, Frag Track follows individual fragments as they travel across the field of view.

The location of each detected fragment is displayed and tracked over time, leading to estimates of each fragment's travel distance (measured in number of pixels), travel time (measured in number of frames), area (measured in number of pixels) and aspect ratio (unitless). The Frag Track output is converted to physical units using the conversion factor determined from the fiduciary video. More specifically, the fragment velocity is converted from pixels/frame into ft/sec based on the frame rate of the camera and the fiduciary. Similarly, the fragment area is converted from number of pixels to in^2 based on the average aspect ratio during the time that the fragment is tracked.

Obviously, Frag Track is not able to track fragments that are completely obscured by smoke or the fireball. In practice, as seen in Figure 16, the fireball tends to preferentially obscure fragments with middling velocities.

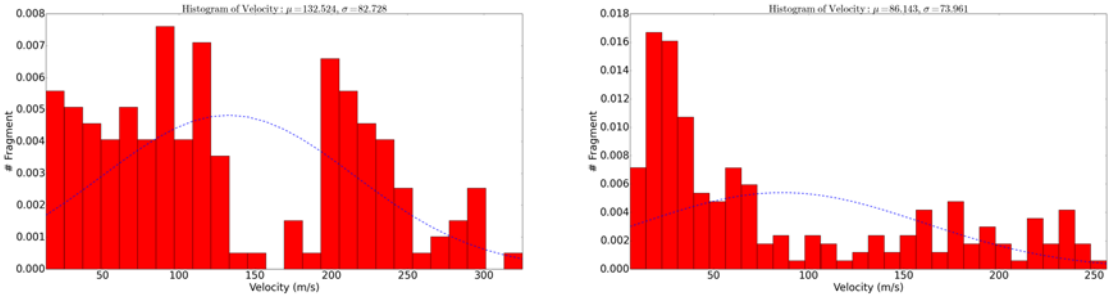

Test 6 *Test 9*

Figure 16 Velocity histograms for Tests 6 and 9 where the fireball obscures the view of mid-range velocity fragments

The circular 'punch out' testing technique used here resulted in a wide range of fragment speeds. The first and fastest fragments form near the center of the target, while the last and slowest fragments form at the periphery, near the outer radius of the shock tube. For example, Figure 17 shows the results for Tests 3 and 4 with CMU plates, which had peak reflected static overpressures of around 1,250 psi and 3,700 psi, respectively. In both cases, the earliest fragments originating from the center of the test sample have the highest velocity. As time progresses, the velocities decrease with an asymptotic value of around 6,000-ft/sec (1,800-m/sec). Because Test 4 has a larger load, the peak velocities are higher than in Test 3.

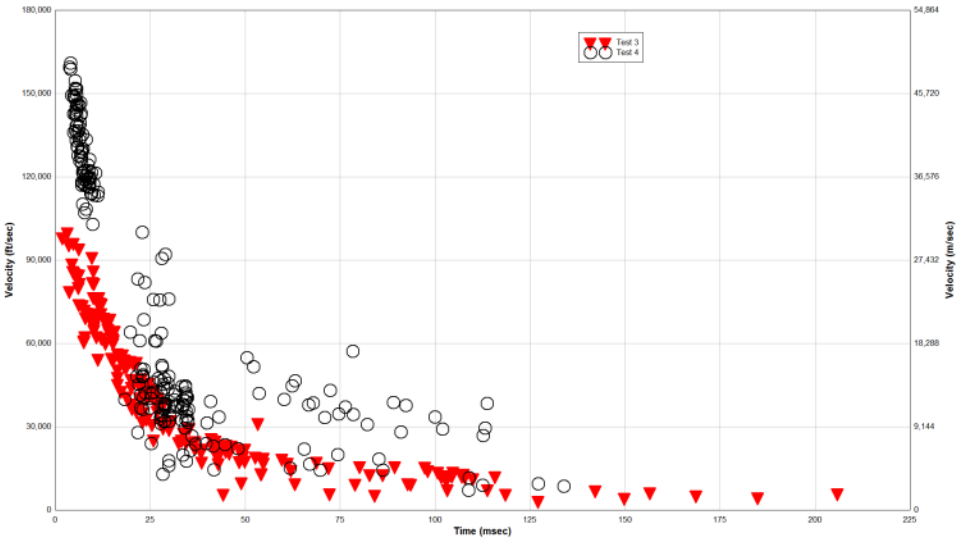

Figure 17. Fragment velocity vs. time for Tests 3 and 4 as determined by Frag Track.

Figure 18 shows median fragment velocity vs. reflected peak static overpressure across all tests. For tempered glass and concrete, higher pressure loadings clearly result in higher median fragment velocities, as expected. However, the trend is not as clear for CMU, probably because such a large portion of these fragments were obscured by smoke and fireball, especially during the high pressure tests.

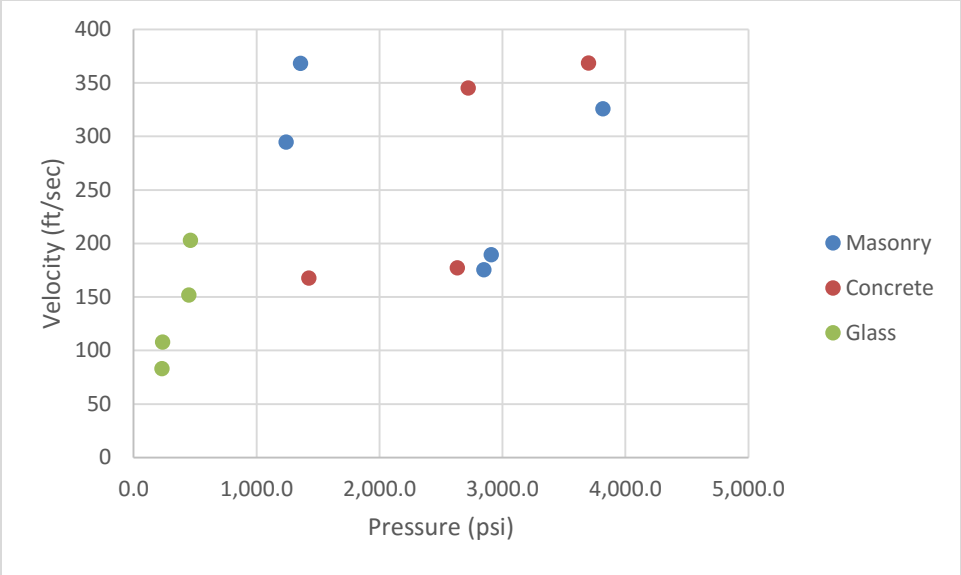

Figure 18. Median velocity vs peak static overpressure for Tests 3-10 and Tests 12-16.

Figure 19 compares the fragment mass distribution for Tests 3 and 4, which had peak reflected static overpressures of around 1,250 psi and 3,700 psi, respectively. The plot shows 20 mass bins, each 0.25-g in width. Because of the larger loading, Test 4 produced smaller fragments overall than Test 3. However, and somewhat surprisingly, Test 4 produced more fragments in the largest sizes bin (>5-g) than Test 3. This is probably because the higher overpressures in Test 4 propelled more large fragments from the periphery of the circular 'punch out' region horizontally into the field of view of the side-on HSV. As discussed later, the video analysis based on Frag Track has a lower fragment size limit on the order of 0.5-g (0.0011-lb), which explains the dramatic drop off in fragment counts in the two smallest size bins.

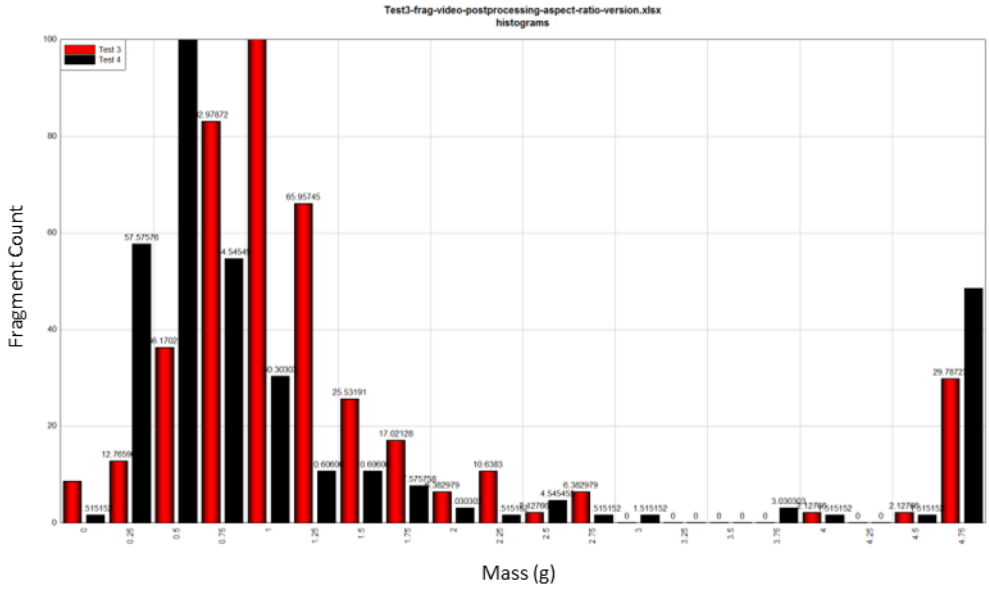

Figure 19. Concrete mass distribution for Tests 3 and 4.

3.2.2 FRAG TRACK VELOCITY ANALYSIS VALIDATION

To confirm that Option 2 in Frag Track correctly measures fragment velocities, the results were compared with manual tracking. In particular, in Test 7 one random fragment was selected from each of three different velocity groups, namely, fast (>1,000-ft/sec), medium (400- to 1,000-ft/sec), and slow (<400-ft/sec) velocity ranges. For each fragment chosen, two time-stamped images were layered on top of the corresponding fiduciary image. The fragment velocity was then hand calculated based on the displacement and change in time. Figure 20 to Figure 22 show the manually-tracked fragment displacement for a random fragment in each of the three velocity groups with the fiduciary image in the background.

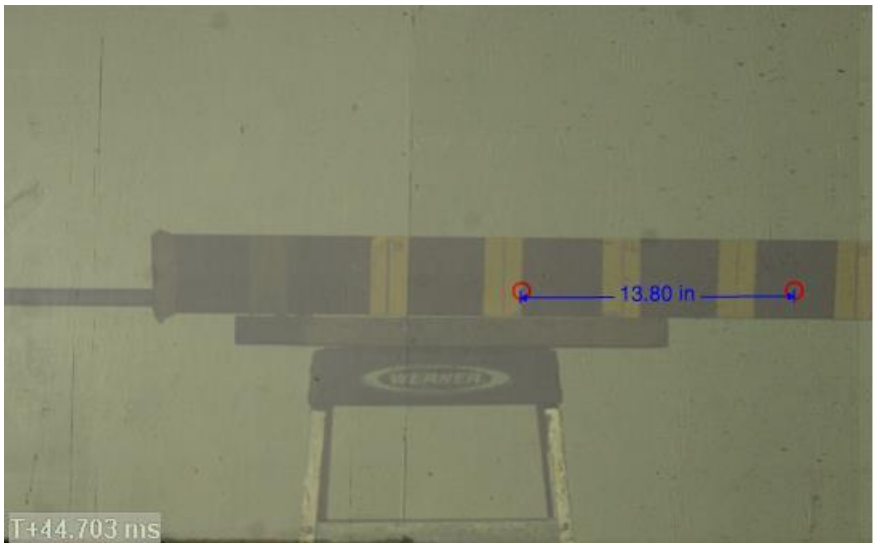

Figure 20. Fragment manually tracked in Test 7 randomly chosen from the fast group.

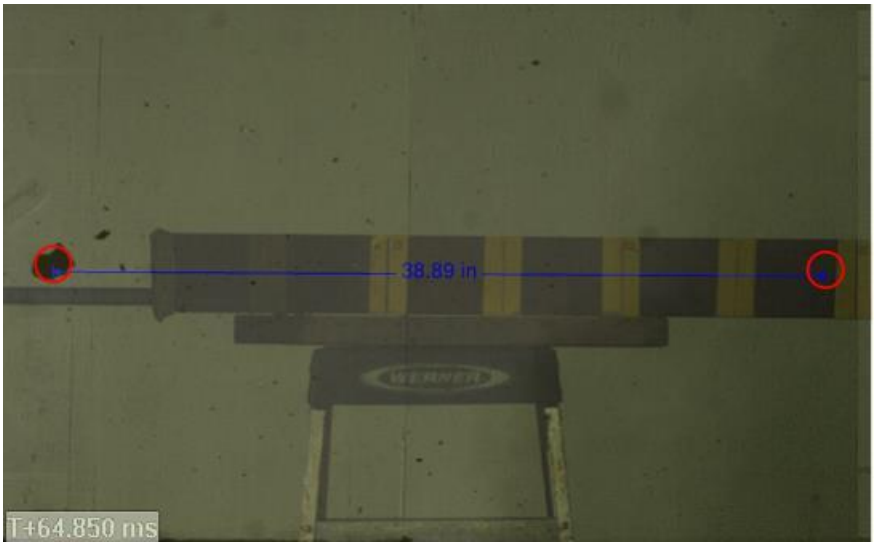

Figure 21. Fragment manually tracked in Test 7 randomly chosen from the middle group.

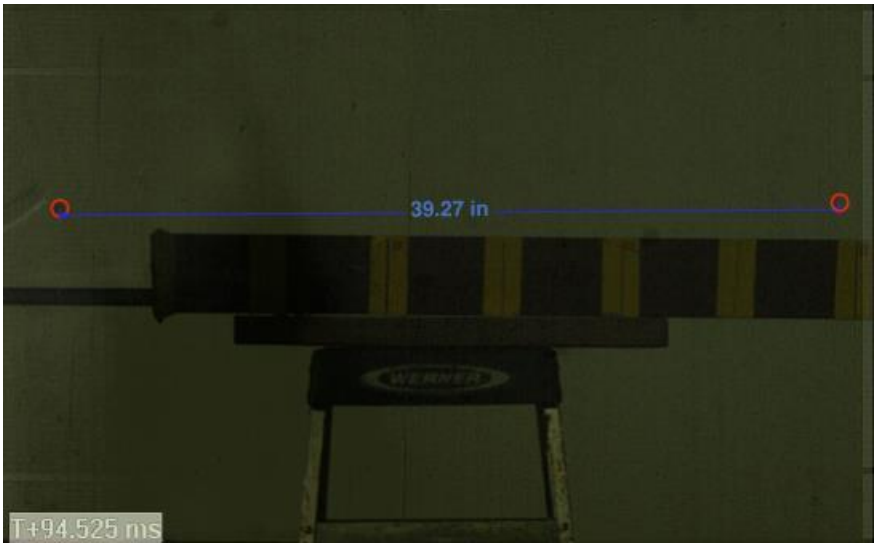

Figure 22. Fragment manually tracked in Test 7 randomly chosen from the slow group.

Table 3 shows the differences between the Frag Track and hand-calculated velocities. Notice that the differences are less than 5% in all cases.

Table 3. Percent Error for Frag Tracker Analysis Software.

Analysis Method	Group 1 Velocity (ft/sec)	Group 2 Velocity (ft/sec)	Group 3 Velocity (ft/sec)
Hand-calculated	604	1,410	216
Frag Track	576	1,401	222
Difference	4.6%	0.6%	-2.7%

3.2.3 Frag Track Mass Analysis Validation

To confirm that Frag Track correctly measures cross-sectional fragment sizes, results were compared to SigmaScan for a random video frame in Test 7. Figure 23 shows the video frame as processed in SigmaScan. Notice that each fragment was assigned a fixed index number. Figure 24 shows the same video frame as processed in Frag Track. Frag Track assumes linear trajectories, as indicated by the red lines. Frag Track will only track objects that are repeatedly detected in adjacent frames.

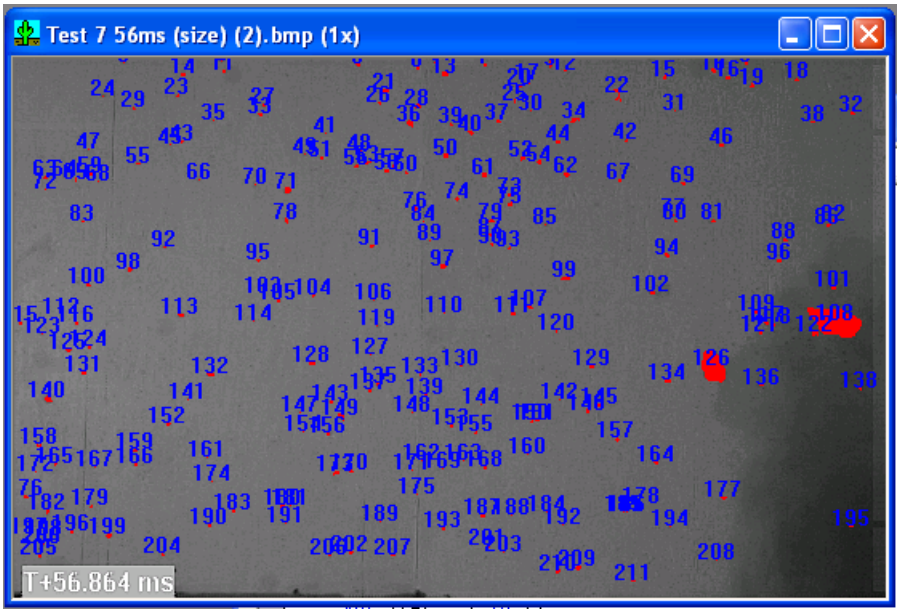

Figure 23. SigmaScan measuring object sizes from a still image.

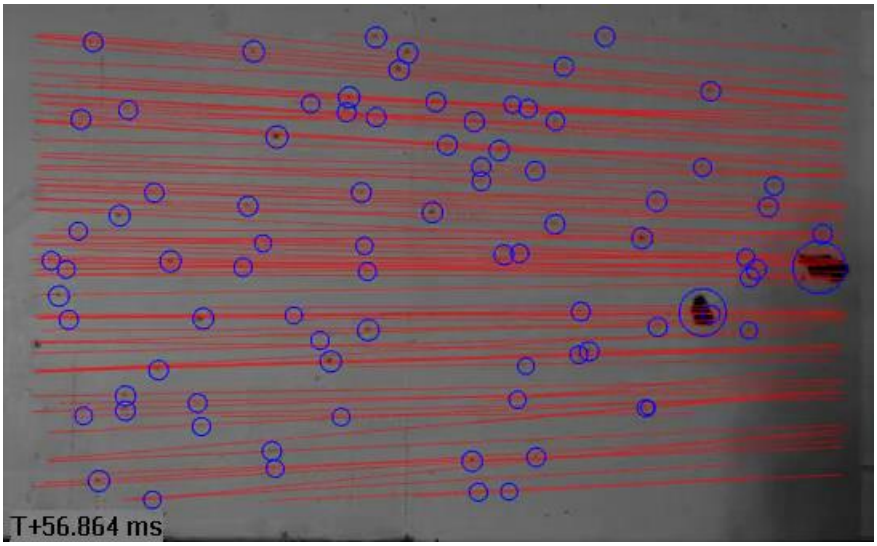

Figure 24. Frag Track measuring object sizes, as well as velocities and trajectories, from the same still image as was shown in Figure 23

Figure 23.

As seen in Figure 25, the two tools agree well for cross-sectional areas larger than one pixel. The top of Figure 25 compares the cumulative distribution functions (CDFs) for fragment areas of three pixels and larger. The bottom of Figure 25 compares the size of each individual fragment including those with an area of a single pixel or a fraction of a pixel. On average, the Frag Track results differ from the SigmaScan results by about -5%. This discrepancy occurs because SigmaScan accepts fragments that Frag Track rejects. SigmaScan requires only that fragments be visible in a single frame, while Frag Track requires that fragments be visible over several adjacent

flames. This causes Frag Track to sometimes reject fragments that are temporarily obscured by smoke and fire.

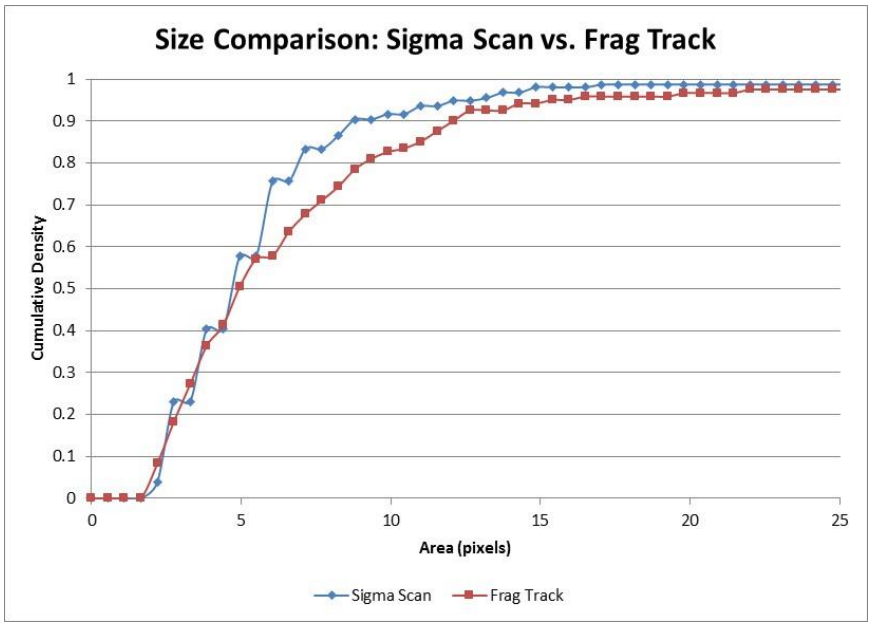

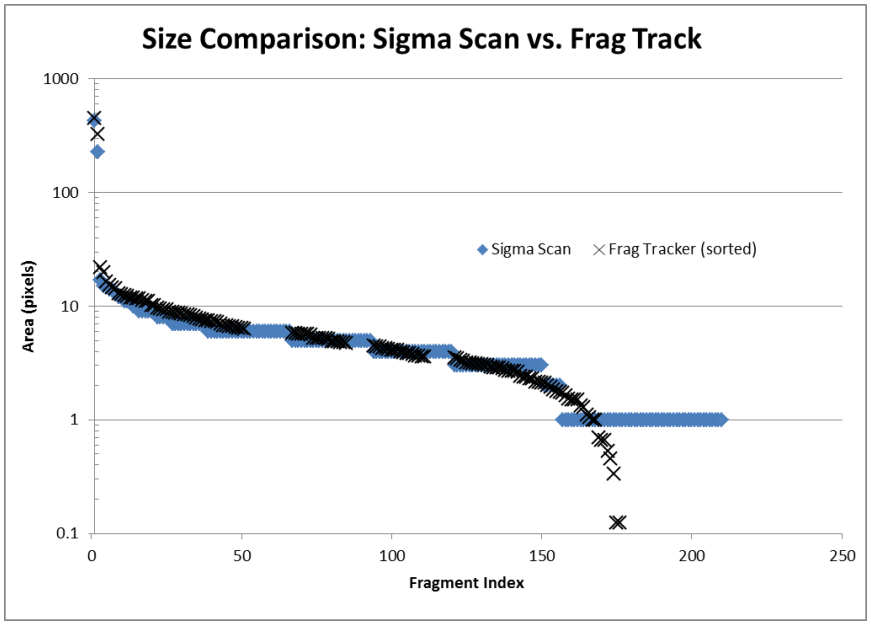

Figure 25. Cumulative distribution function and cross-sectional fragment size comparison between SigmaScan and Frag Track.

3.3 ANALYSIS OF LATE-TIME PHYSICALLY-COLLECTED FRAGMENTS

As described in Section 2, fragments were physically collected in each test using a fragment catcher. Even after excluding the smaller fragments, well over 50,000 fragments were collected in this test series. It was not possible to weigh so many fragments by hand within the resources

available for this project. Two main alternatives were considered: sieving and shadowgraphy. Sieving is a classic technique for quickly characterizing large numbers of fragments by passing them through a series of increasing finer sieves and measuring the weight captured in each sieve. However, this approach produces only rough estimates of the fragment size distribution. Shadowgraphy, combined with digital image processing, is another classic technique for characterizing large numbers of fragments. However, shadowgraphy is typically restricted to cases where the out-of-plane dimension is fixed or can easily be inferred from the in-plane cross-section. Examples include liquid atomization, where the fragments are uniformly spherical, and thin plate fragments where all but the smallest fragments have a fixed out-of-plane thickness.

Holography has the potential to overcome the limitations of shadowgraphy and is routinely used for liquid atomization in well-controlled laboratory settings. However, prior attempts to use holography for field applications such as this one have failed. Thus holography was considered too risky to attempt for this project.

The mining and processing industries have recently developed shadowgraphy-based techniques for automatic characterization of vast quantities of material, including cases where the individual fragments substantially deviate from the usual assumptions; see, e.g., [6]. Unfortunately, this body of literature was discovered too late to apply it in this effort.

Instead, a new technique was developed that combines sieving and shadowgraphy. It was found that the errors inherent in applying shadowgraphy to random three-dimensional objects can be substantially reduced by sieving the material first. The new technique was validated by comparing the results to hand measurements.

The remainder of this section describes the new characterization technique in detail. The fragments collected in each test were passed through a series of increasingly finer sieves in order to group them by size. After the overall contents of each sieve were weighed, the fragments were staged for pictures by laying them out on a flat surface. These pictures were analyzed using SigmaScan with a minimum fragment mass of 0.005 g. Below 0.005 g, it was impractical to physically separate individual fragments, as would be required to avoid treating multiple fragments as a single fragment.

For example, Figure 26 shows the fragments physically collected in Tests 13 and 14. These fragments were run through a series of sieves to separate the fragments into bins. As seen in Figure 27, the fragments from each bin were carefully laid out and photographed. SigmaScan's image editing features were used to convert each photograph to a high-contrast image, which allowed SigmaScan to estimate fragment sizes more accurately.

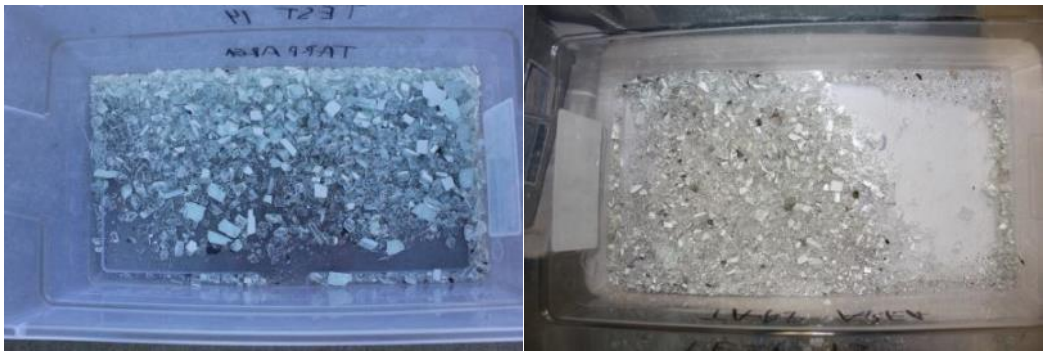

Test 13 *Test 14*

Figure 26. Fragments collected from the designated collection area in Tests 13 and 14.

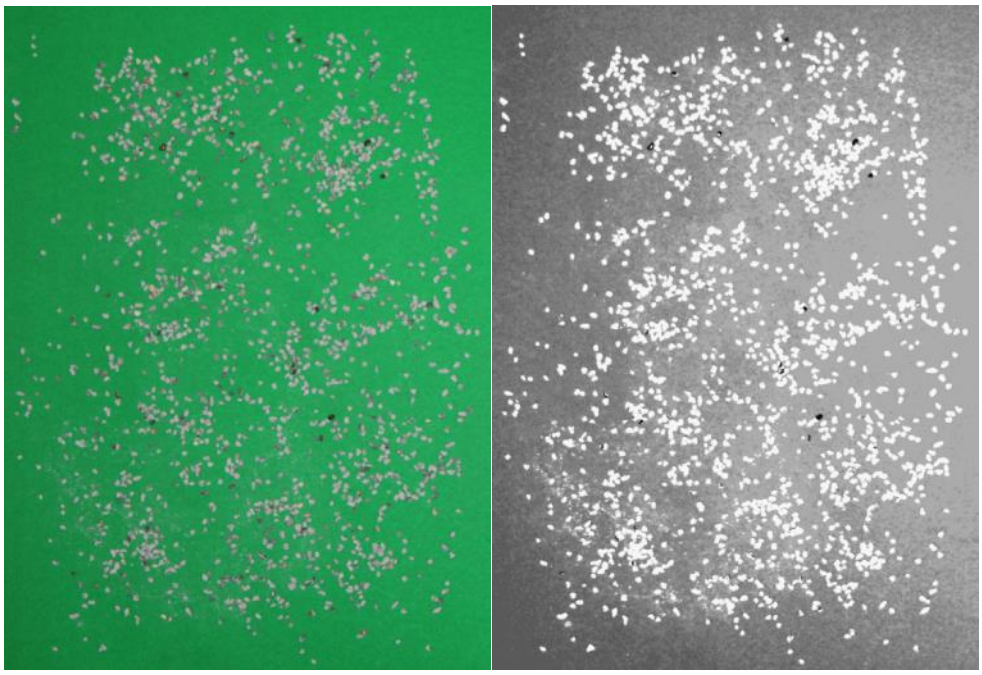

Figure 27. Fragments captured in sieve #8 in Test 5 before (left) and after (right) SigmaScan processing.

For each bin/sieve, the mass was calculated for individual fragments as follows:

$$m_i = A_i \cdot \frac{\sum m_i}{\sum A_i}$$

where m_i is the mass and A_i is the cross-sectional area of fragment i. In other words, the mass-to-area ratio of each individual fragment was assumed to be the same as the cumulative mass to cumulative area ratio of all fragments in the same bin.

SigmaScan is able to distinguish small differences in contrast intensity. As a result, SigmaScan is capable of registering tiny particles on the order of 10^{-2} in^2 in high resolution images, potentially including ambient dust and almost-invisible cross-contamination between different tests. As seen in Figure 28, the spreadsheet results produced by SigmaScan were post-processed using Microsoft Excel. Excel macros and simple logic functions were used to exclude microscopic fragments during post-processing, in order obtain accurate cumulative area calculations and to enforce the above assumptions concerning uniform thicknesses.

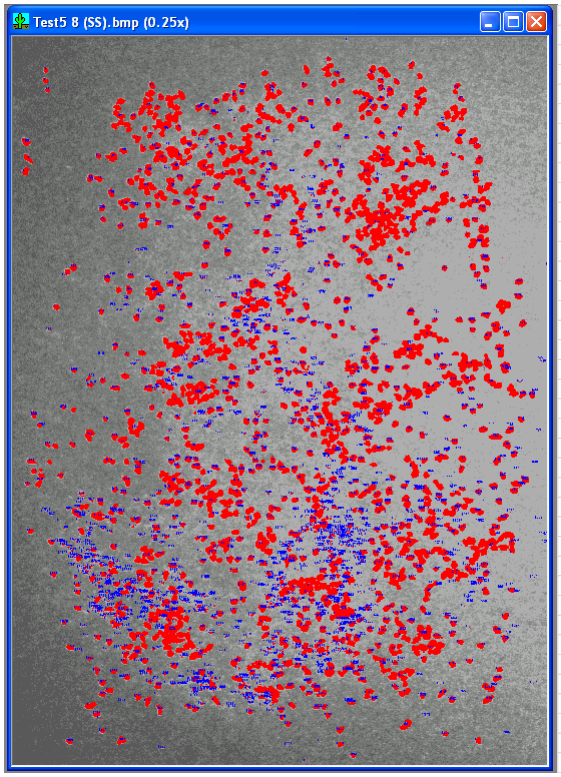

Object No.	Area (pixels)	797
1	3	0
2	313	1
3	613	1
4	1615	1
5	1310	1
6	653	1
7	1278	1
8	295	1
9	504	1
10	385	1
11	445	1
12	373	1
13	453	1
14	493	1
15	477	1
16	479	1
17	542	1
18	406	1
19	2793	1
20	546	1
21	816	1
22	3	0
23	536	1
24	921	1
25	3212	1
26	1	0
27	265	1
28	2978	1
29	4134	1
30	344	1
31	788	1
32	7821	1
33	1	0
34	820	1
35	548	1
36	554	1
37	454	1
38	1	0

Figure 28. Processed SigmaScan image and spreadsheet output.

More specifically, two passes were made in Excel. In the first pass, logic functions and VBA code were used to enforce a lower limit for an object area (in pixels). In the second pass, errors were corrected in which SigmaScan treated multiple adjacent fragments as one fragment. In laying out the fragments from each sieve prior to photographing them, every attempt was made to physically separate the fragments. However, inevitably, a certain fraction ended up touching or slightly overlaying each other.

Figure 29 shows part of the resulting Excel spreadsheet for the #8 sieve in Test 5. In the figure, column A shows the indexed object number, column B shows the original area measurement, column E is a counter for the first pass, and column F is an adjusted counter for the second pass. For each sieve a fragment area (cell I1) representative of the actual maximum area was used to adjust the individual measurements in column G. Initially this area was selected based on the median of the original data set (cell H6) with small adjustments made by hand to account for variability between each sieve and between each test. The spreadsheet also shows the estimated number of fragments after the first pass first pass (797 objects, cell E2) and the estimated number of fragments after the second pass (1,754 fragments, cell F2) based on a representative fragment area (589 pixels). The adjusted areas in column G are calculated by dividing values in column D by values in column F. As a result of the two passes and adjustments made to the data set, adjusted averages (cell I4) and adjusted medians (cell I6) agree with each other. To further ensure the accuracy of this process, adjusted area measurements were thoroughly spot checked in SigmaScan by comparing the fragment counter values in column F to visible fragments taken directly from the image. Spots checks were performed for every image (and consequently every sieve) for all tests.

	A	D	E	F	G	H	I
1	Object No.	Area (pix)	First Pass	Second Pass	Adj. Area	**Rep. Area:**	**589**
2			797	1754			
3	2	313	1	1	313	**Avg.**	**Adj. Avg.**
4	3	613	1	2	307	**1038.45**	**437**
5	4	1615	1	3	538	**Med.**	**Adj. Med.**
6	5	1310	1	3	437	**583**	**447**
7	6	653	1	2	327		
8	7	1278	1	3	426		
9	8	295	1	1	295		
10	9	504	1	1	504		
11	10	385	1	1	385		
12	11	445	1	1	445		
13	12	373	1	1	373		
14	13	453	1	1	453		
15	14	493	1	1	493		
16	15	477	1	1	477		
17	16	479	1	1	479		
18	17	542	1	1	542		
19	18	406	1	1	406		
20	19	2793	1	5	559		
21	20	546	1	1	546		
22	21	816	1	2	408		
23	23	536	1	1	536		
24	24	921	1	2	461		
25	25	3212	1	6	535		
26	27	265	1	1	265		
27	28	2978	1	6	496		
28	29	4134	1	8	517		
29	30	344	1	1	344		
30	31	788	1	2	394		
31	32	7821	1	14	559		
32	34	820	1	2	410		

Figure 29. Corrected fragment sizes for sieve #8 in Test 5.

3.3.1 VALIDATION

As noted earlier, sieving was used to reduce the errors inherent in applying shadowgraphy to objects with variable unknown out-of-plane shapes and thicknesses To gage the success of this approach, the results were compared against hand measurements done on three random subsets of fragments collected in Test 7. More specifically, 100 random fragments were gathered from three different sieves and hand-weighed. Figure 30 to Figure 32 show the comparison between hand-weighed fragments and SigmaScan-calculated weights for a #6 sieve (0.132" nominal sieve opening), a #4 sieve (nominal 0.187" opening), and a ¼" sieve fragments.

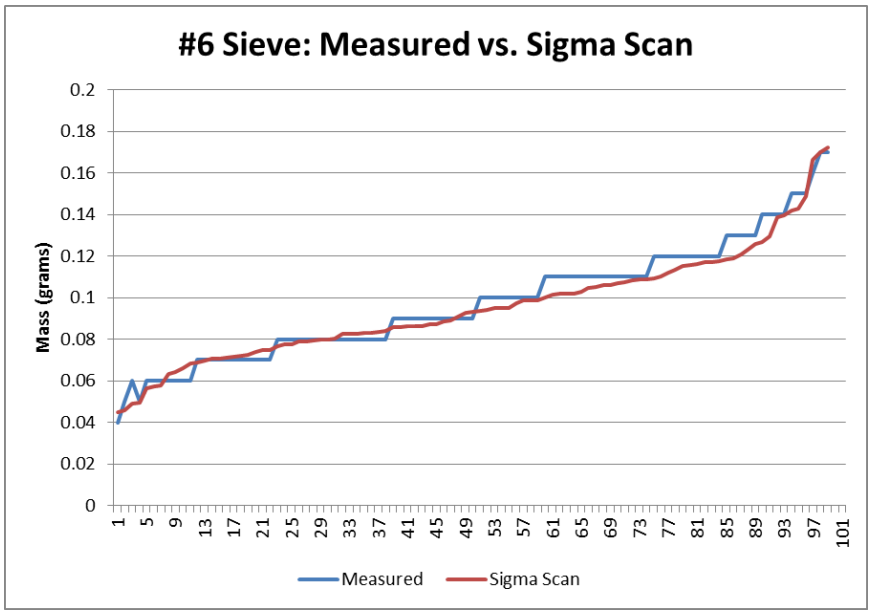

Figure 30. SigmaScan vs. hand measured weights for 100 fragments taken from a #6 sieve in Test 7

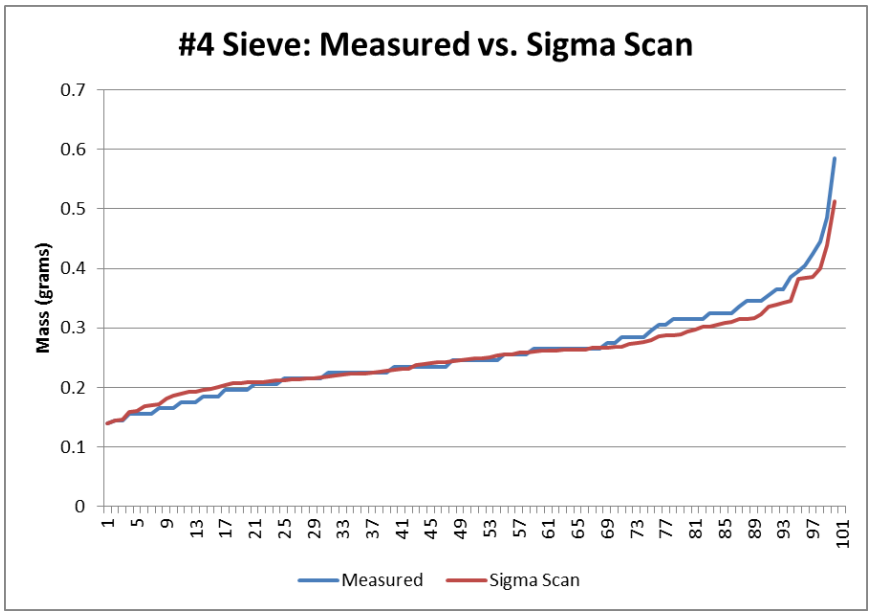

Figure 31. SigmaScan vs hand measured weights for 100 fragments taken from a #4 sieve in Test 7.

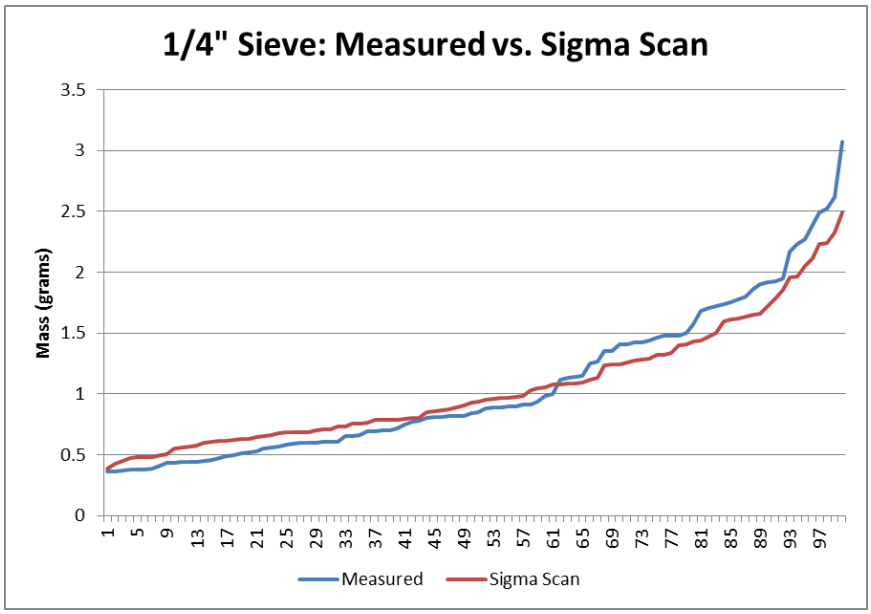

Figure 32. SigmaScan vs hand measured weights for 100 fragments taken from a ¼" sieve in Test 7.

Table 4 compares hand measured and SigmaScan values for average mass, minimum mass, maximum mass. In addition, Table 4 shows percent error averaged over 100 fragments. In general, SigmaScan tends to slightly over predict the mass of smaller fragments and slightly under predict the mass of larger fragments.

Table 4. Comparison of hand-weighed fragments to calculated masses from SigmaScan.

Sieve Size	Avg. Mass (g)		Min. Mass (g)		Max Mass (g)		Avg.% Error
	Measured	SigmaScan	Measured	SigmaScan	Measured	SigmaScan	
#6	0.098	0.096	0.05	0.046	0.17	0.17	-2%
#4	0.259	0.255	0.14	0.14	0.59	0.51	-1%
¼"	1.052	1.052	0.31	0.38	3.12	2.50	12%

4 RESULTS

4.1 DEBRIS DISTRIBUTIONS

4.1.1 General Observations

Table 5 shows the number and mass of the subset of fragments that passed through the fragment stripper and were physically collected and sieved. As expected, the total mass of physically collected fragments was consistently much less than the mass of the original sample. However, the total mass of the physically collected fragments was often close to the mass of the *loaded* area of the original sample, i.e., the 6.25-in diameter disk in the center of the test sample. The number of fragments collected ranged from 3,703 fragments in Test 16 up to 8,367 fragments in Test 7.

Table 5. Summary of fragments captured using physical collection techniques.

Test	Sample	Mass (lb)	Collected Weight (lb)	% of Original Plate Weight	% of Directly Loaded Weight	Fragment Count
3	CMU	39.5	4.12	10%	94.3%	4,520
4	CMU	40.65	1.53	4%	31.5%	7,481
5	Concrete	40.2	5.30	13%	110.2%	4,831
6	Concrete	40.95	1.76	4%	35.9%	3,751
7	CMU	39.75	4.12	10%	86.6%	8,367
8	Concrete	40.9	2.56	6%	52.3%	3,905
9	Concrete	38.5	3.08	8%	66.9%	4,564
10	CMU	40.1	1.99	5%	41.5%	6,779
12	CMU	40.55	1.93	5%	39.8%	6,576
13	Tempered glass	5.2	0.48	9%	77.1%	3,967
14	Tempered glass	5.2	0.72	14%	115.7%	3,967
15	Tempered glass	5.2	0.72	14%	115.7%	3,579
16	Tempered glass	5.15	0.50	10%	81.1%	3,703

Figure 33 shows a typical view of the fragments that were not physically collected because they travelled at oblique angles and hit the fragment stripper.

Figure 33. A typical view of the debris that did not pass through the fragment stripper.

Table 6 shows the number, mass and velocity of the subset of fragments characterized in side-view HSV analysis using Frag Track. The number and mass of fragments obtained from side-view HSV is, not surprisingly, less than the number and mass of fragments obtained from physical collection. This is due to the limited viewing area of the side-view HSV cameras, obscuration from smoke and fire from the high explosives, omission of small fragments due to limited video resolution, omission of some fragments due to limited appearance in successive video frames, and omission of fragments with large upward or downward velocity components, including those which ricocheted from the ground surface.

Table 6. Summary of fragments captured in high speed video using Frag Track.

Test	Sample	Mass (lb)	Video Tracked Weight (lb)	% of Original Plate Weight	Frag Count	% of Directly Loaded Weight	Median Velocity (ft/sec)	Qualitative Notes on Frag Track Processing
3	CMU	39.5	1.98	5%	192	41.9%	294.6	Video goes dark early in the event. Visible debris was tracked
4	CMU	40.65	1.36	3%	224	28.0%	325.7	Missed detection of some of the initial high-speed fragments. Gap in fragment data as fireball passes through video
5	CMU	40.2	1.67	4%	364	34.7%	167.6	Some debris is completely obscured by smoke at around 110-ms. Other than this, about 90% of the visible debris was tracked
6	Concrete	40.95	1.21	3%	164	24.7%	368.5	Debris was engulfed and completely obscured by the fireball towards the end of the video. Appears that visible debris was tracked well.
7	CMU	39.75	1.76	4%	389	37.0%	368.2	Visible fragments were tracked well.
8	Concrete	40.9	3.31	8%	220	67.6%	345.2	Some fragments obscured by fireball. Visible fragments appear to have been tracked well.
9	Concrete	38.5	1.41	4%	201	30.6%	177.2	Missed some small high-speed fragments. Fireball partially covers debris from ~50-80 msec.
10	CMU	40.1	0.6	1%	254	12.5%	175.4	Video was very obscured by smoke and fire. Visible debris is tracked, but the amount of visible debris is small.
12	CMU	40.55	1.22	3%	325	25.1%	189.4	Video was overexposed at beginning. Some fragments were tracked through smoke.
13	Temp glass	5.2	0.39	8%	173	62.7%	202.9	No issues. All visible tempered glass fragments were tracked well.
14	Temp glass	5.2	1.1	21%	856	176.8%	107.9	No issues. All visible tempered glass fragments were tracked well.
15	Temp glass	5.2	0.58	11%	293	93.2%	83.2	No issues. All visible tempered glass fragments were tracked well.
16	Temp glass	5.15	0.99	19%	712	160.6%	151.8	No issues. All visible tempered glass fragments were tracked well.

The Frag Track, SigmaScan, and sieve analyses were combined to determine distributions for debris mass and velocity for each experiment. For each data set, histograms were developed with either mass or velocity on the horizontal axis and fragment count on the vertical axis. Figure 34 through Figure 36 provide mass distributions for six of the thirteen tests. The mass distribution from the collected fragments is laid over the mass distribution from the video analysis. In many cases, the Frag Track video mass matches the collected fragment mass fairly well, except for the smallest fragments. The discrepancy for small fragments is due to the fact that the side-view video technique is able to accurately capture fragment masses as small as ~0.5-g (0.00112-lb) while the physical collection technique is able to accurately capture fragment masses as small as ~0.005 g. Notice that the video technique obtains greater random variation due to the smaller sample size. These results seem to indicate that fragments did not experience any significant size changes between the mid-time, mid-air state captured in the side-view HSV and the final late-time resting state captured in physical collection. This conclusion, if true, implies that the only dramatic changes occur between early-time state captured in the rear-view HSV – when the fragment cloud is high-speed and dense and thus especially prone to shattering collisions – and the mid-time state captured in the side-view HSV. This conclusion is especially significant for the glass fragments, which are the most fragile, and can easily shatter due to collisions with the catcher.

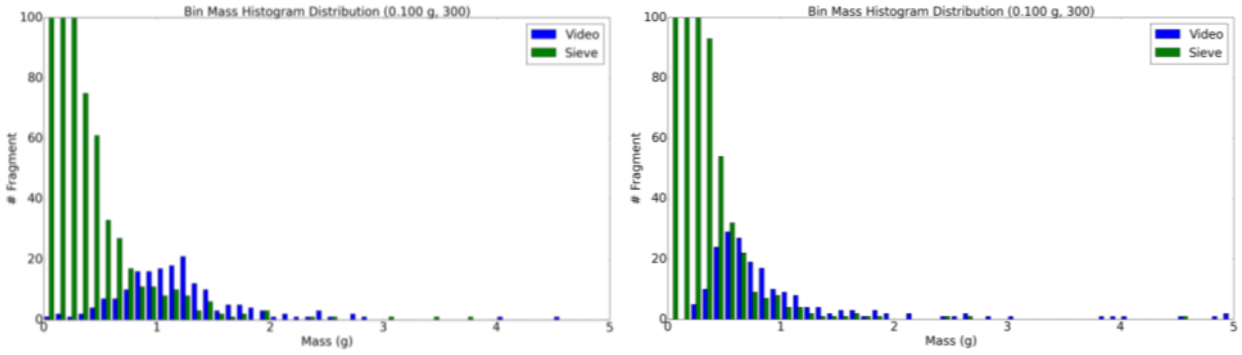

Test 3 *Test 4*

Figure 34. Fragment mass histograms for CMU Tests 3 and 4.

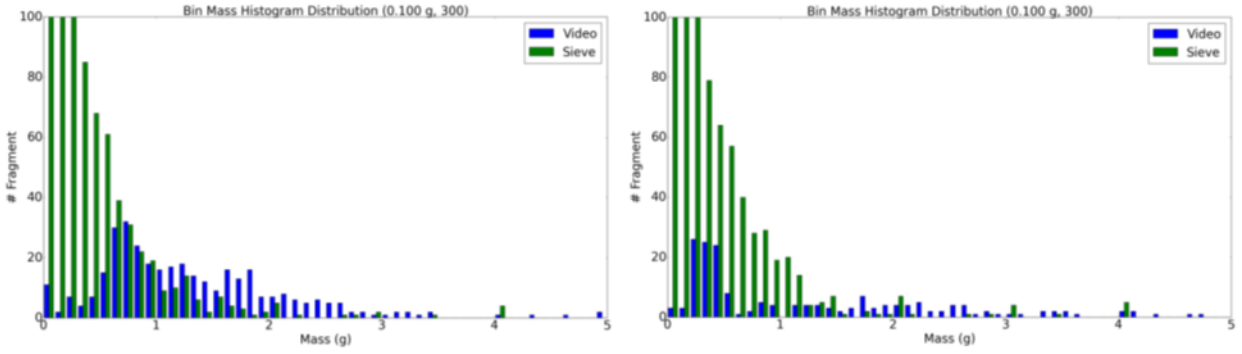

Test 5 *Test 9*

Figure 35. Fragment mass histograms for concrete Tests 5 and 9.

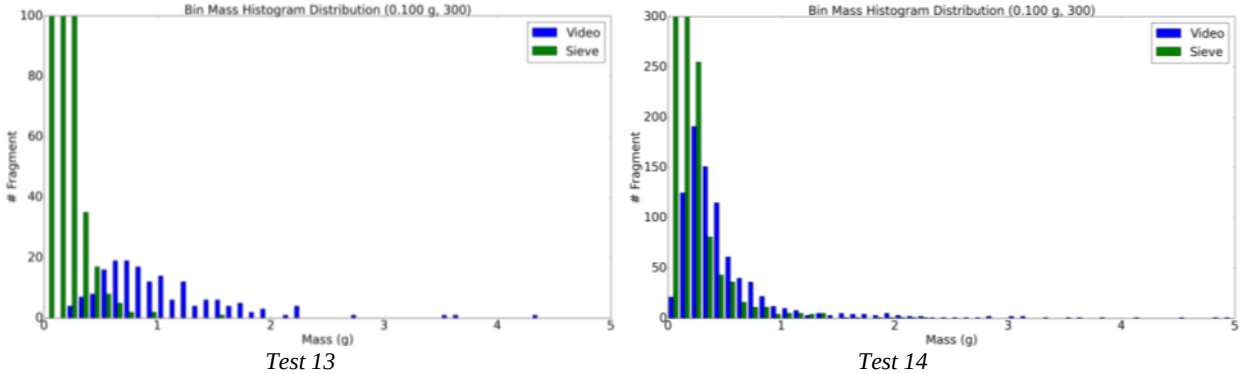

Test 13 *Test 14*

Figure 36. Fragment mass histograms for tests tempered glass Tests 13 and 14.

Figure 37 and Figure 38 show that, for concrete, a large loading rate (Test 6) produces more small fragments moving at higher velocities than a small loading rate (Test 5). Similarly, Figure 39 and Figure 40 show that, for CMU, a large loading rate (Test 4) produces more small fragments moving at higher velocities than a small loading rate (Test 3). The trend is less evident for tempered glass. In particular, Figure 41 shows results for Tests 13 and 16 at 500-psi while Figure 42 shows results for Test 14 at 250-psi. Test 13 has higher velocities but more large fragments than Test 14.

Test 16 has more small fragments but velocities are no larger than in Test 14. These inconsistencies merit further study.

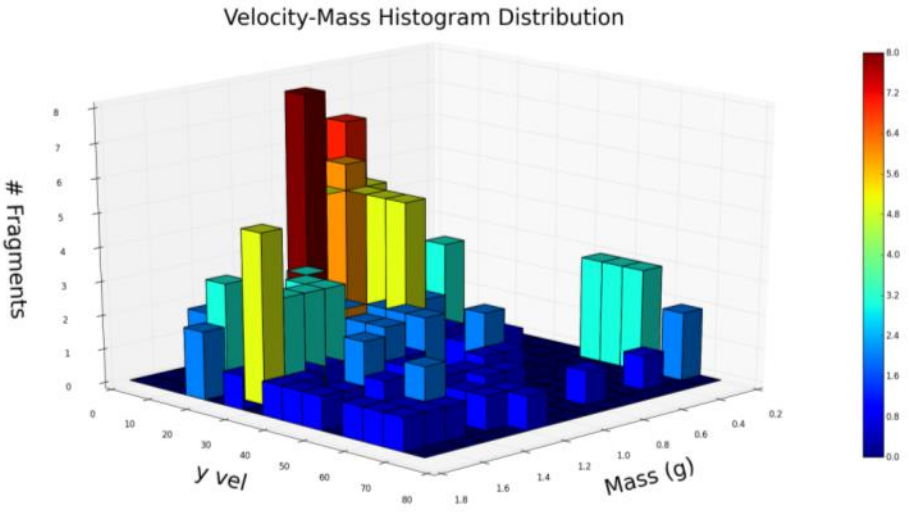

Figure 37. Velocity-mass histogram for Test 5.

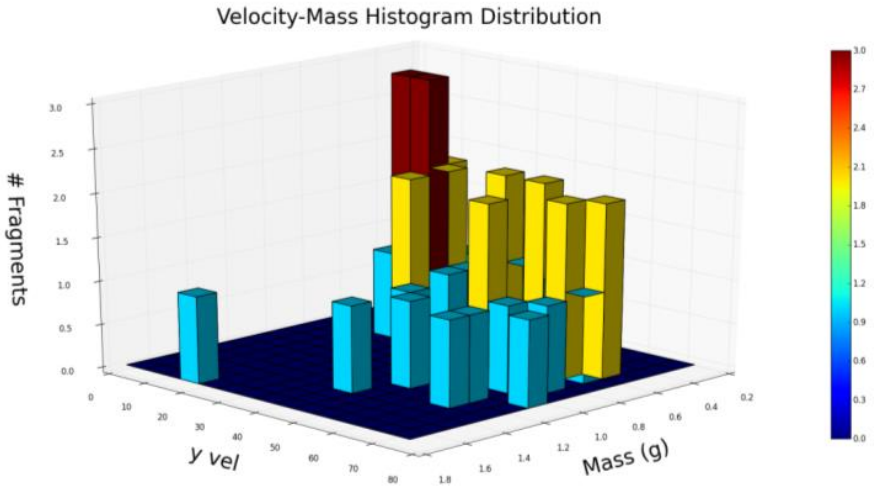

Figure 38. Velocity-mass histogram for Test 6.

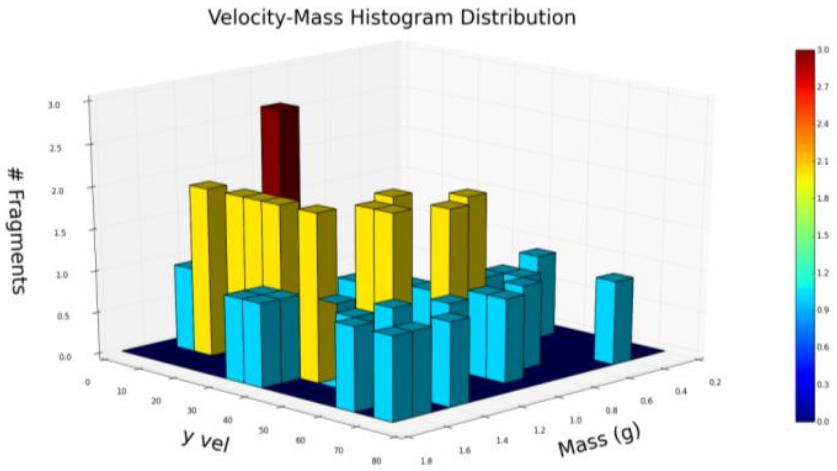

Figure 39. Velocity-mass histogram for Test 3.

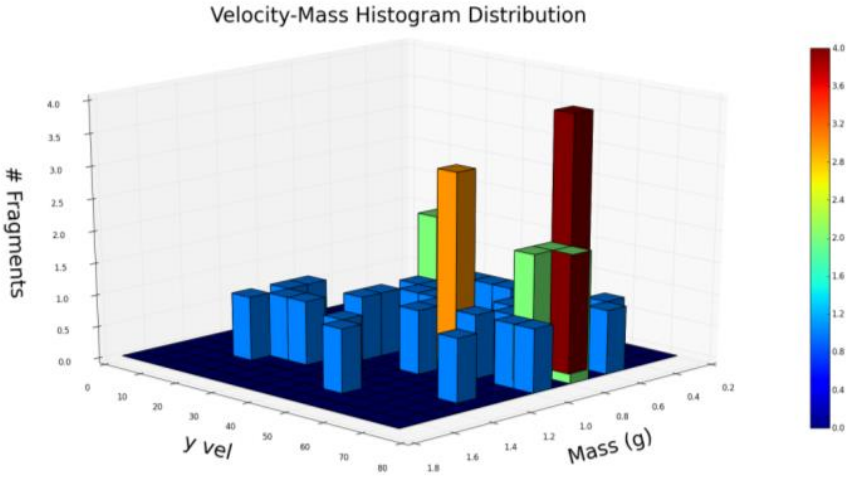

Figure 40. Velocity-mass histogram for Test 4.

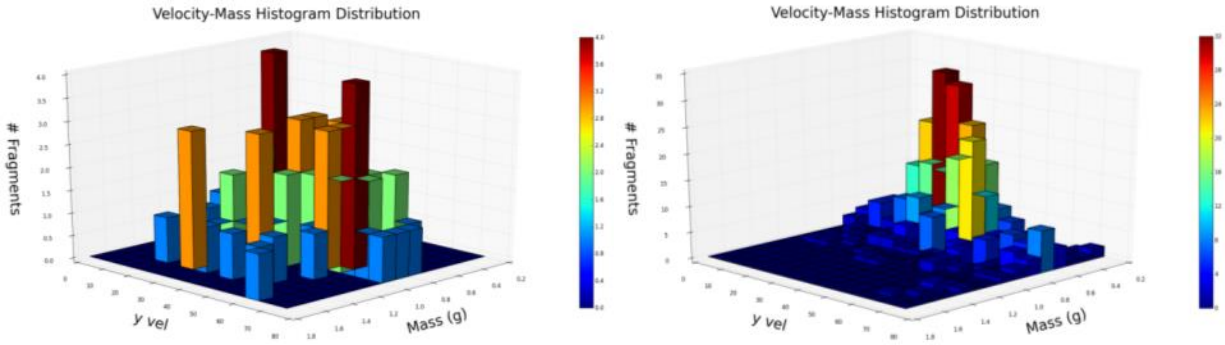

Test 13 *Test 16*

Figure 41. Velocity-mass histogram for Tests 13 and 16.

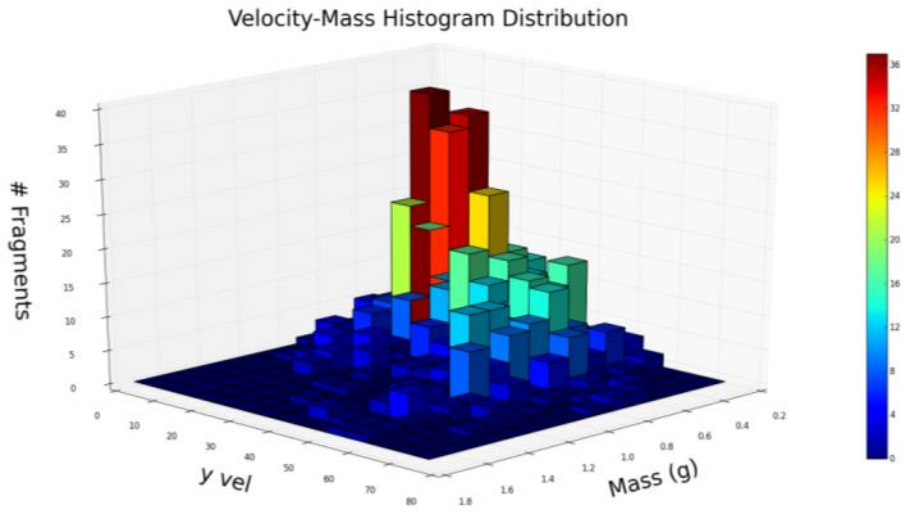

Figure 42. Velocity-mass histogram for Test 14.

4.1.2 Analysis and Distribution Fit Approach

Fragment size distributions are commonly described by cumulative distribution functions (CDFs) and probability density functions (PDFs). The *cumulative distribution function* $F(M)$ is the number fraction of fragments with masses greater than or equal to *M*. Similarly, the *probability density function* $f(M)$ is the number fraction of fragments with masses in a range *dM* centered on *M* divided by *dM*. Notice that $F(x)$ is monotone decreasing such that $F(0)=1$ and $F(\infty)=0$ and that $f(x)$ is always non-negative such that:

$$\int_0^\infty f(x)dx = 1.$$

Also notice that:

$$F(M) = -\int_M^\infty f(x)dx; \;\; f(M) = -\frac{dF}{dM}$$

This assumes an infinite range of fragment sizes. The CDFs and PDFs over the limited range $M_{min} \leq M \leq M_{max}$ are related to the CDFs and PDFs over an infinite range as follows:

$$\tilde{F}(M) = \frac{F(x) - F(M_{min})}{F(M_{max}) - F(M_{min})}$$

$$\tilde{f}(M) = \frac{f(M)}{F(M_{max}) - F(M_{min})}$$

The *count mean mass* is defined as follows:

$$M_{avg} = \int_0^{\infty} Mf(M)dM$$

for an infinite range and:

$$\tilde{M}_{avg} = \int_{M_{\min}}^{M_{\max}} M\tilde{f}(M)dM = \frac{\int_{M_{\min}}^{M_{\max}} Mf(M)dM}{\int_{M_{\min}}^{M_{\max}} f(M)dM}$$

for a finite range. Notice that, for simple one-step fragmentation, conservation of mass, momentum, and energy yield expressions for M_{avg} as a function of strain rate, e.g., [7] [8]. However, this is obviously not the case for $\tilde{M}_{avg}$, which depends on the arbitrary values M_{min} and M_{max}. Normalizing by the count mean mass, *Weibull size distributions* may be defined as follows:

$$F(M) = \exp\left[-c\left(\frac{M}{M_{avg}}\right)^r\right]$$

$$f(M) = \frac{c\,|\,r\,|}{M_{avg}}\left(\frac{M}{M_{avg}}\right)^{r-1} \exp\left[-c\left(\frac{M}{M_{avg}}\right)^r\right]$$

where *r* is a free parameter and where:

$$c = \Gamma\left(1+\frac{1}{r}\right)^r$$

As shown in Laney [9]:

$$r = \frac{n}{m}$$

where *n* is the exponent in the Weibull size distribution written in terms of fragment diameter and *m* is the fragment dimension, e.g., $m = 3$ for CMU and concrete and $m = 2$ for plate glass.

As before, the Weibull size distribution can be modified to account for a limited range. As a specific example, suppose that $r > 0$ and $M \le M_{max} \ll M_{avg}$. As another specific example, suppose that $r < 0$ and $M \ge M_{min} \gg M_{avg}$. In either case, Weibull size distributions are approximately equal to *power law size distributions*:

$$F(M) = \begin{cases} 1-(M/M_{\max})^r & r>0 \\ (M/M_{\min})^r & r<0 \end{cases}$$

$$f(M) = \begin{cases} \dfrac{r}{M_{\max}}\left(\dfrac{M}{M_{\max}}\right)^{r-1} & r>0 \\ \dfrac{|r|}{M_{\min}}\left(\dfrac{M}{M_{\min}}\right)^{r-1} & r<0 \end{cases}$$

Approximate values for *r* were obtained by curve fitting the experimental results. This is a surprisingly complex problem. Table 7 lists seven major issues.

Table 7. Issues faced in curve fitting experimental fragment size distributions.

Issue	Discussion	Solution
1. Independent Variable	The fitting outcome depends on the choice of independent variable. The most common choices are mass and diameter. Less common choices are cross-sectional area and surface area.	Base all curve fits on fragment mass. Because fragments are eccentrically shaped, estimating the experimental diameter or area is difficult.
2. Dependent Variable	The fitting outcome depends on the choice of dependent variable. Two common choices are PDFs and CDFs.	Choose fitting parameters to obtain a reasonable compromise between fit quality for the PDF and CDF.
3. Binning	Binning is optional for CDFs but mandatory for PDFs. The fitting outcome depends on the choice of bin limits. The simplest binning strategy – fixed bin widths – typically results in overpopulated small bins and underpopulated large bins, both of which adversely impact fit quality.	Away from the extremes, choose bin limits so that adjacent bins have the same mass. For the largest and smallest fragments, choose the bin limits to minimize changes in mass between adjacent bins. Compare results for coarse (10 bins), medium (35 bins), and fine (150 bins) resolution.
4. Fitting Functions	The fitting outcome depends on the choice of fitting function. While the research literature suggests numerous possibilities, uncommon fitting functions explored in this project offered no advantage over common fitting functions.	Use either Weibull or power law size distributions.
5. Sample Ranges	The fitting outcome depends on upper or lower limits imposed by experimental techniques, e.g., limited optical resolution. In particular, the side-view HSV results only obtained the upper tail of the size distribution.	Account for minimum fragment sizes in the expressions for the PDFs and CDFs, as described above.
6. Normali-Zation	The fitting outcome depends on the choice of normalization. The most common normalization involves dividing size by a characteristic size. The limited-range count mean mass is easy to determine but varies dramatically with range. The full-range count diameter, while not readily apparent from any given set of test data, does not depend on an artificially-limited range.	Divide all masses by the *full-range* count mean mass. This requires inferring the full-range count mean mass from the *limited-range* experimental data. In essence, the full-range count mean mass is a second parameter, in addition to *r*, chosen to minimize fitting error.
7. Error Weighting	Common approaches include least squares fitting in linear-linear and log-log planes.	Choose the fitting parameters to obtain a reasonable compromise between different error weighting schemes using a χ^2 approach.

Numerous attempts were made to develop automated *ad hoc* fitting procedures, using MS Excel macros, to implement the solutions given in Table 7. Unfortunately, because of the difficulty of optimizing across two variables using MS Excel macros, these procedures were unable to implement (5.) and (6.). This had a particularly serious impact on the side-view HSV, which had a large minimum fragment size, as seen in later in Section 4.1.4.

While this subsection has discussed fragment size, similar expressions and considerations apply for fragment velocity, as seen later in Section 4.1.4.

4.1.3 Mass Distributions From Rear-View HSV Analysis

This subsection describes the early-time mass distributions obtained from an analysis of the rear-view HSV using SigmaScan. As described earlier, results are limited to three tests involving plate glass test objects, namely, Tests 13, 15 and 16. While the glass plates completely shattered, the SigmaScan analysis captured only the very-early-time fragments produced by a roughly circular sub-region, with a radius about 2/3 of that of the supporting plate; see Figure 43. These very-early-time fragments were still in or near the same plane as the original glass plate, unlike the fragments formed at slightly later times from the deflected perimeter, which makes it easy to convert pixel counts to physical dimensions. The SigmaScan analysis omitted the very small fragments produced at the perimeter of the sub-region.

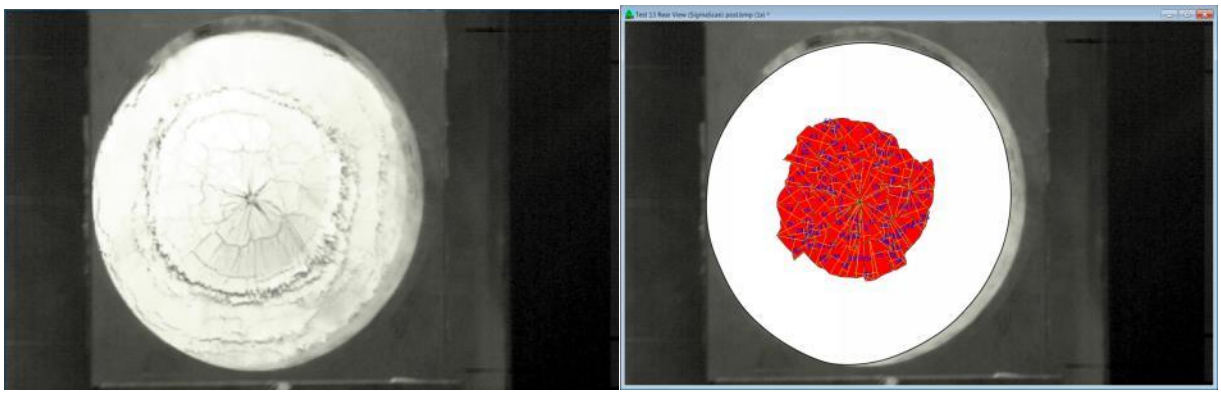

Figure 43. Development of fragment sizes from SigmaScan analysis.

Table 8 summarizes the outcome of the SigmaScan analysis of the rear-view HSV, where $\widetilde{M}_{avg}$ refers to the count mean mass over the experimental range $M_{min} \leq M \leq M_{max}$. In all three cases, the experimental mass range was at least 3 orders-of-magnitude. However, because all of the fragments less than about 10% of $\widetilde{M}_{avg}$ were either rejected as unreliable or collected into the smallest size bin, and because all of the largest fragments were collected into another size bin, the practical mass range was only about 1.5 orders-of-magnitude, just wide enough to obtain reliable curve fits.

Table 8. Statistical parameters for rear-view HSV mass distributions.

Material	Test	# Frags Observed	Total Mass Observed (g)	M_{max} (g)	M_{max} (g)	$\widetilde{M}_{avg}$ (g)
Tempered Glass	13	431	375	0.003	10.65	0.866
	15	414	541	0.0004	71.35	1.250
	16	651	520	0.003	7.52	0.798

Table 9 shows the best-fit Weibull size distributions. More specifically, the first three rows show the curve fits obtained for Tests 13, 15, and 16 individually; see also Figure 44, Figure 45, and Figure 46, respectively.[1] The last row shows the curve fit obtained for Tests 13, 15, and 16 combined; see also Figure 47. Notice that no attempt was made adjust for the minimum or maximum fragment sizes, i.e., the full-range and limited-range count mean masses were assumed to be the same. Also notice that, even though Tests 13 and 16 were essentially the same, they obtained substantially different results. This is probably because, in Test 13, the SigmaScan analysis was performed at an earlier time than in Test 16, before the fragments in the center subregion were fully formed. In each test, the SigmaScan analysis was performed at the earliest time possible, as soon as the fragment outlines were readily apparent in the rear-view HSV, which introduced a degree of test-to-test variation depending on lighting conditions and other factors.

Table 9. Best-fit Weibull parameters based on rear-view HSV mass in Tests 13, 15, and 16 involving plate glass test objects.

Material	Test	Pressure (psi)	Weibull Parameters	
			r	$M_{avg} \cong \widetilde{M}_{avg}$ (g)
Tempered Glass	13	Low (250)	1.06 (*)	0.866
	15	High (500)	0.69	1.250
	16	Low (250)	0.64	0.798
	Combined		0.78	

(*) Measured before the fragments were fully formed.

[1] In these and all subsequent figures, the label "Probability Density" on the vertical axis refers to the PDF *times the count mean mass*, i.e., it refers to $M_{avg} f(M)$.

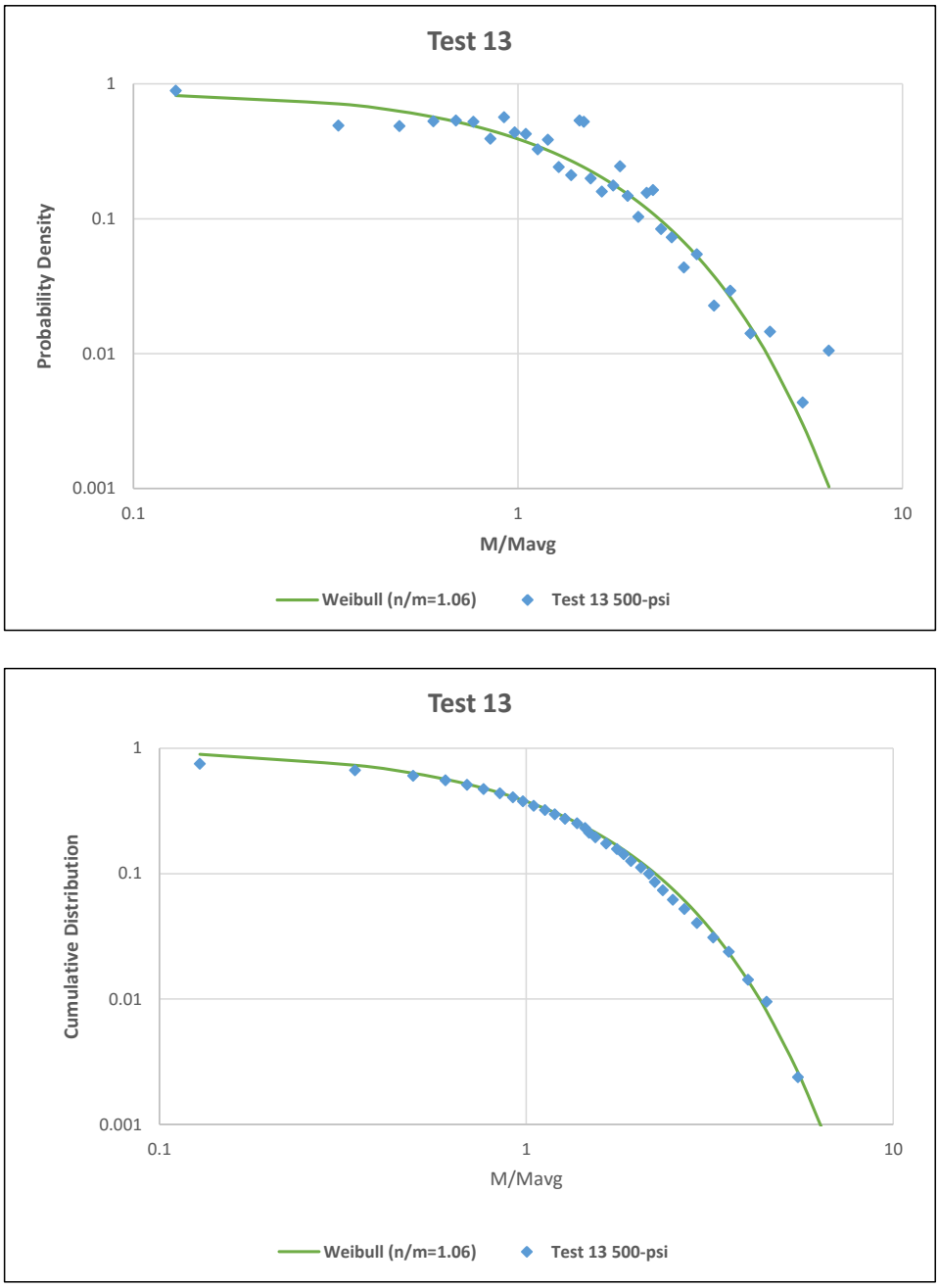

Figure 44. Best-fit Weibull mass distribution for rear-view HSV test data for PDF (top) and CDF (bottom) for Test 13 for tempered glass.

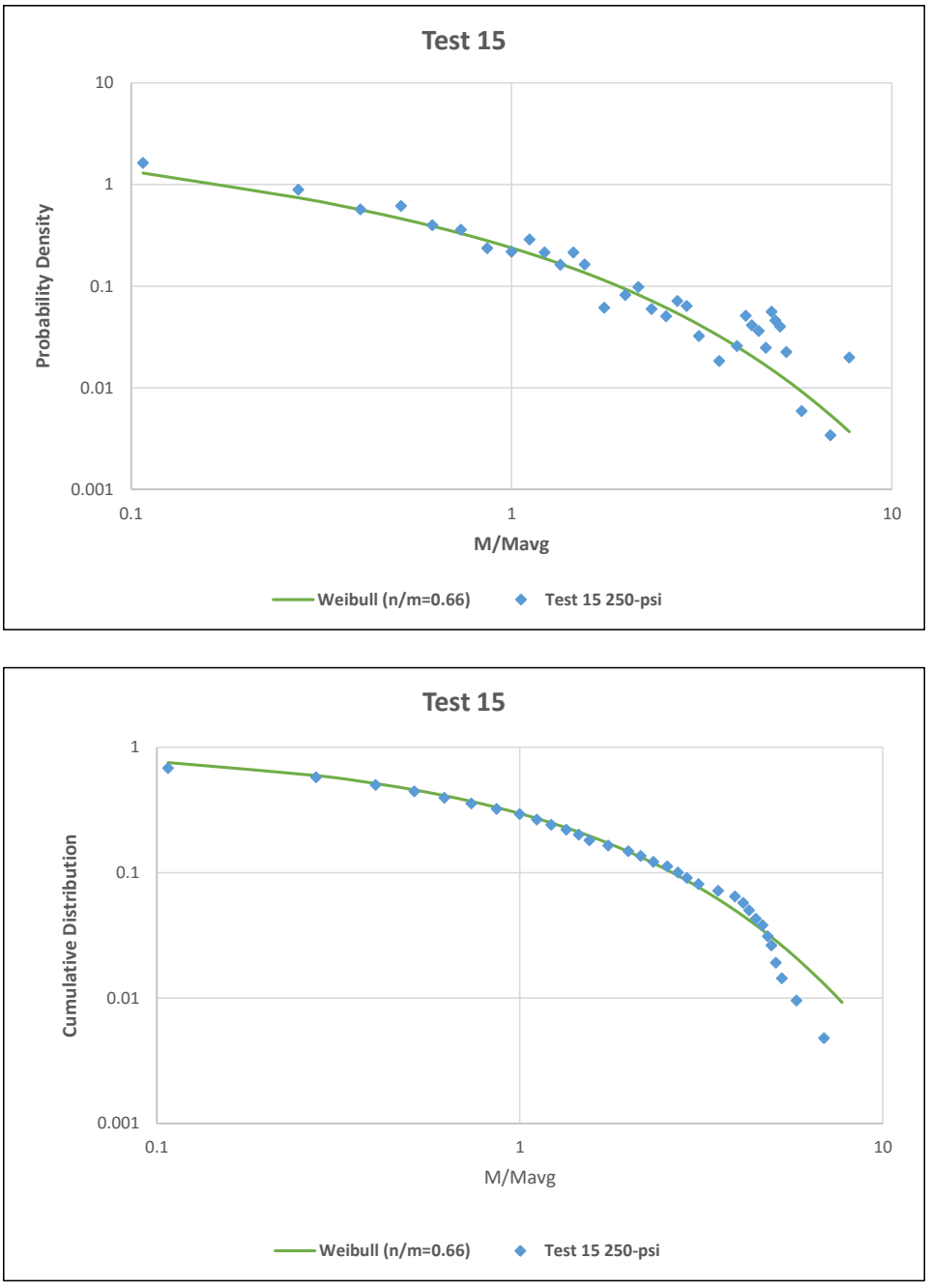

Figure 45. Best-fit Weibull mass distribution for rear-view HSV test data for PDF (top) and CDF (bottom) for Test 15 for tempered glass.

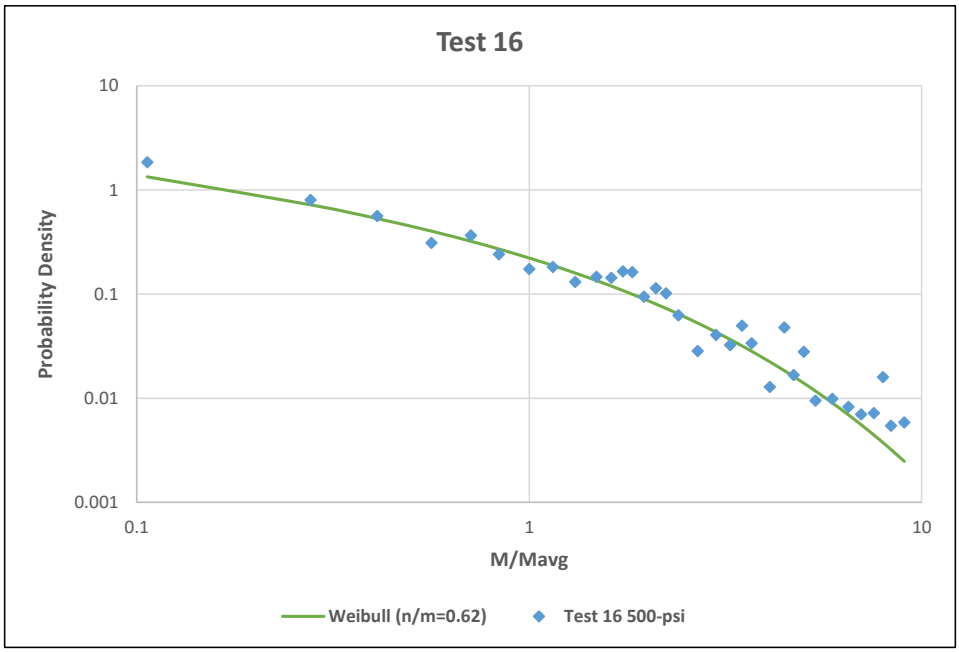

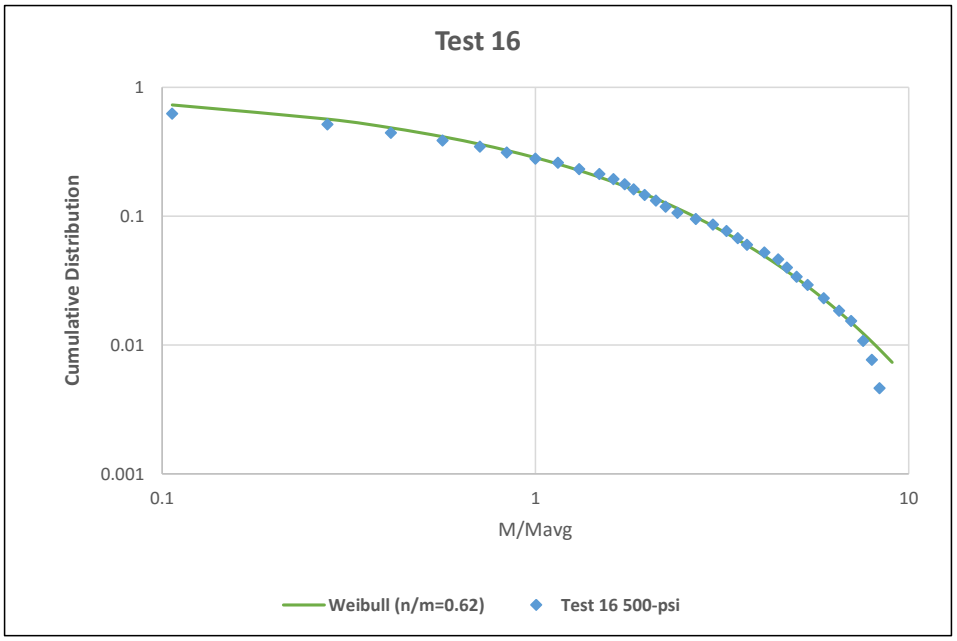

Figure 46. Best-fit Weibull mass distribution for rear-view HSV test data for PDF (top) and CDF (bottom) for Test 15 for tempered glass.

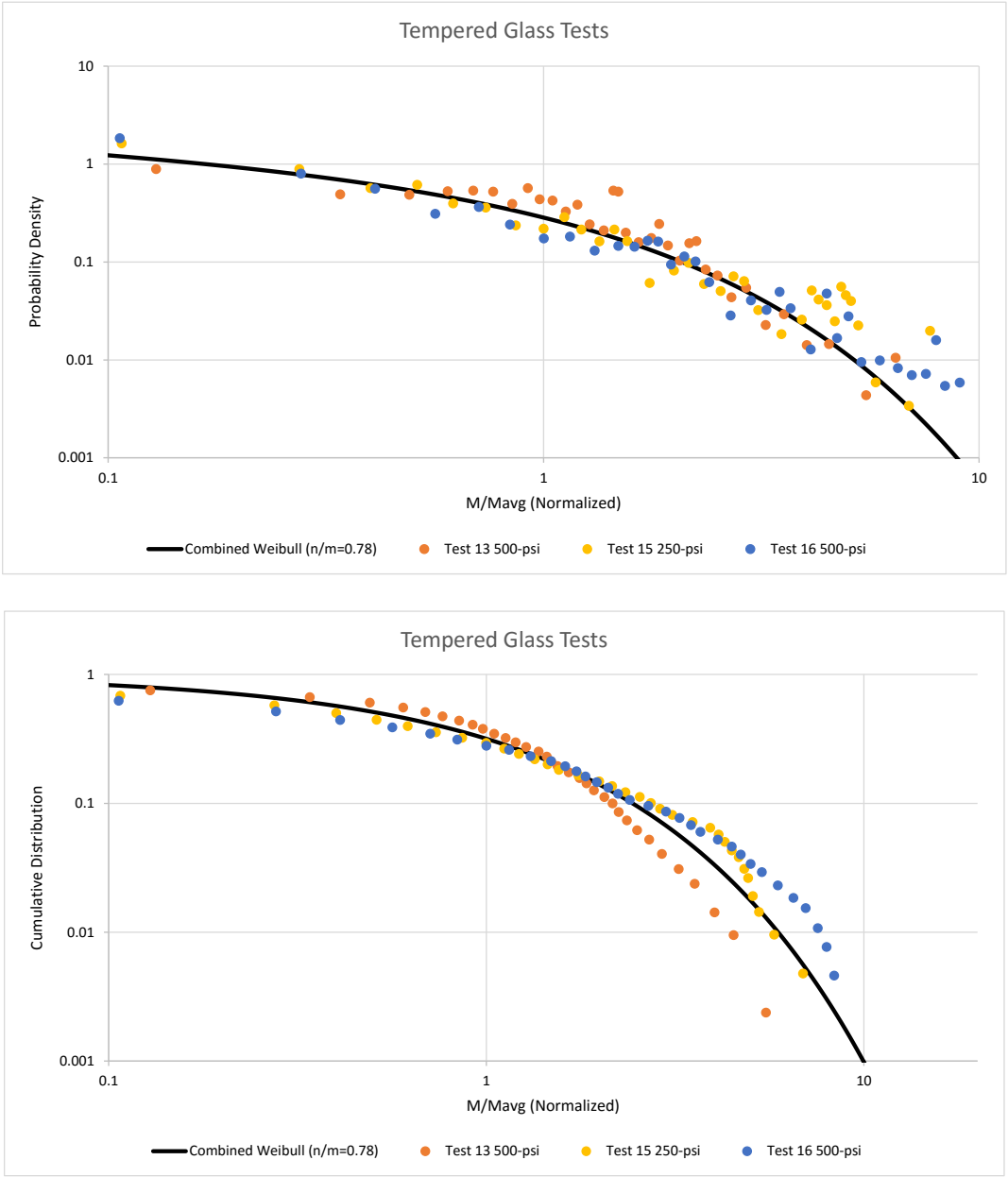

Figure 47. Best-fit Weibull mass distribution for rear-view HSV test data for PDF (top) and CDF (bottom) for Tests 13, 15 and 16 for tempered glass.

4.1.4 Mass and Velocity Distributions from Side-View HSV Analysis

This subsection describes the mid-time mass and velocity distributions obtained from analyzing the side-view HSV using Frag Track. As discussed in Section 4.1.1, Frag Track imposes a minimum fragment size of 0.1 to 0.5-g, which is much larger than in the early- and late-time measurement techniques. As discussed in Section 4.1.2, curve fitting procedures must account for large minimum fragment sizes. In particular, the full-range count mean mass must be estimated from a finite-range of fragments, which is generally much larger.

For example, Figure 48 shows the results for Test 16 with $M_{min} = 0.1$g, $M_{max} = 16$g, and $\widetilde{M}_{avg} = 0.903$g. The Weibull parameters were estimated to be $r = 0.91$ and $M_{avg} = 0.798$g. However, comparing with the early- and late-time results, both of these parameters are clearly too large. In particular, the early- and late-time results both obtained $r \approx 2/3$, which implies that $r \approx 2/3$ at mid-times as well.

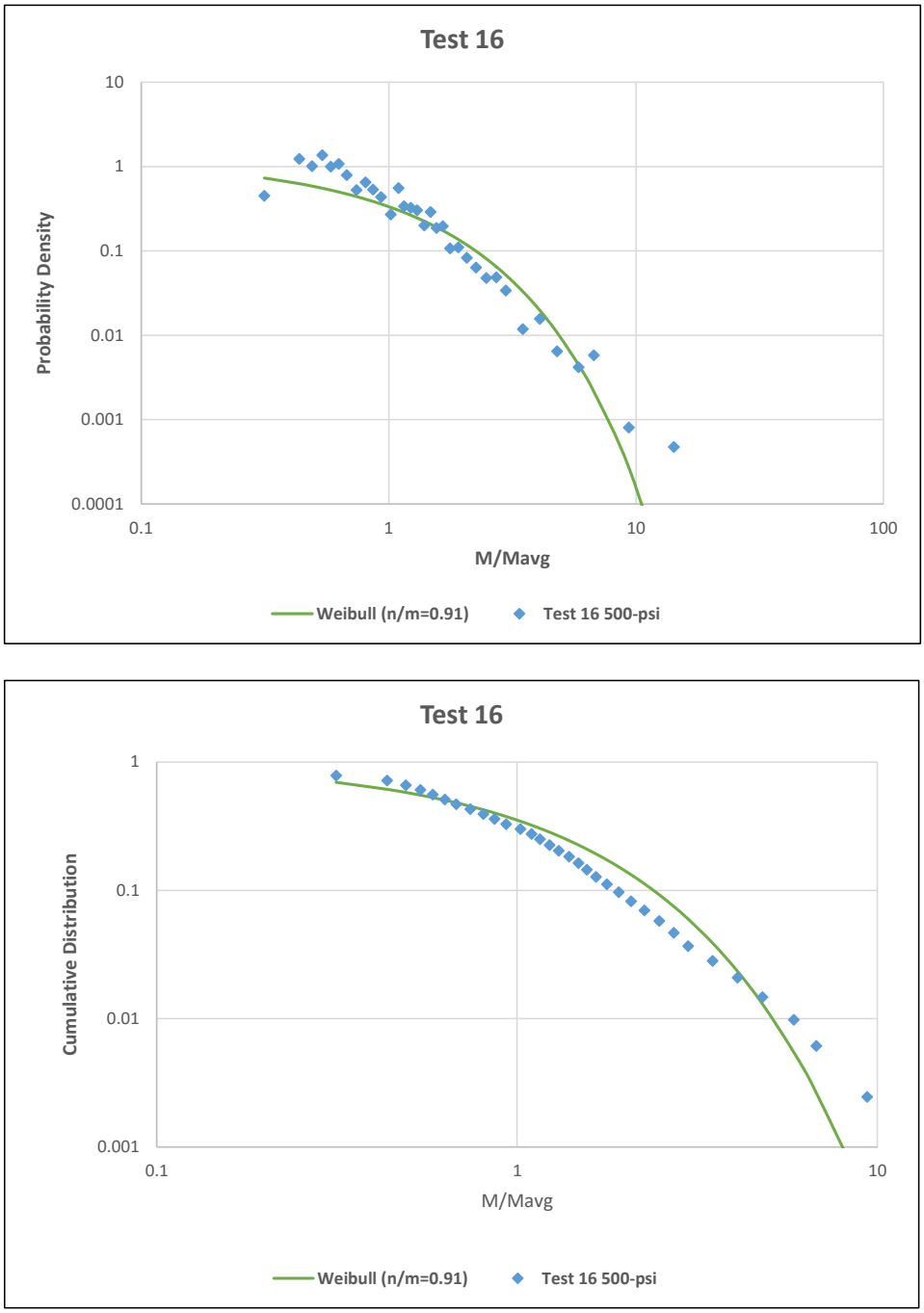

Figure 48. Best-fit Weibull mass distribution for side-view HSV test data for PDF (top) and CDF (bottom) for Test 16 involving glass.

Table 10 summarizes the outcome of the Frag Track analysis of the side-view HSV for mass. In theory, the experimental mass range was between 1.5 and 2.5 orders-of-magnitude. However, because most of the smallest fragments were collected into one size bin, and most of the largest fragments were collected into another size bin, the practical mass range was only about 1 order-

of-magnitude, which limits fitting fidelity. This problem was exacerbated by random noise in the PDFs, which tended to be severe when the number of observed fragments was less than about 250.

Table 10. Statistical parameters for side-view HSV mass distributions.

Material	Test	Pressure (psi)	# Frags Observed	Total Mass Observed (g)	M_{max} (g)	M_{max} (g)	$\widetilde{M}_{avg}$ (g)	Random Noise in PDF
CMU	3	Low (1,500)	192	1,403	0.1	11	1.983	Severe
	4	High (4,000)	224	813	0.3	9	1.531	Moderate
	7	Low (1,500)	390	1,151	0.1	12	0.978	Light
	10	Med (3,000)	254	406	0.3	8	1.078	Severe
	12	Med (3,000)	325	804	0.1	23	2.317	Severe
Tempered Glass	13	High (500)	173	260	0.4	10	1.507	Severe
	14	Low (250)	856	817	0.1	31	0.932	Light
	15	Low (250)	293	352	0.3	9	1.021	Light
	16	High (500)	712	656	0.1	16	0.903	Light
Concrete	5	Low (1,500)	364	1,183	0.1	14	1.333	Moderate
	6	High (4,000)	164	750	0.1	13	1.923	Severe
	8	Med (3,000)	220	1,783	0.2	35	2.712	Severe
	9	Med (3,000)	201	843	0.1	10	1.994	Severe

A number of different *ad hoc* fitting procedures were attempted over a period of several months. Table 11 compares the results of two of those attempts. As one difference, Method 2 generally assumed that M_{avg} is about the same as $\widetilde{M}_{avg}$ while Method 3 generally assumed that M_{avg} is much less than $\widetilde{M}_{avg}$, in line with the late-time results obtained via physical collection.

Table 11. Best-fit Weibull parameters based on side-view HSV mass.

Material	Test	Weibull Parameters			
		Method 2 (July 2016)		Method 3 (Sep 2016)	
		r	M_{avg} (g)	r	M_{avg} (g)
CMU	3	1.60	1.967	0.39	0.188
	4	0.90	1.554	0.34	0.066
	7	1.00	1.130	0.58	0.193
	10	1.40	1.173	0.37	0.096
	12	1.10	2.024	0.25	0.099
Tempered Glass	13	1.70	1.526	1.11	0.866
	14	1.10	1.243	0.83	0.972
	15	1.20	1.119	1.06	1.250
	16	1.23	1.201	0.91	0.798
Concrete	5	1.20	1.379	0.42	0.209
	6	1.10	2.198	0.24	0.181
	8	1.60	2.469	0.26	0.164
	9	1.20	2.280	0.26	0.221
Average		1.26	1.64	0.54	0.408

NOTE: The Weibull parameters shown in this table are believed to have significant errors due to test data limitations.

Table 11 is given for reference purposes only. After comparing the early-, mid- and late-time results, *these curve fits are believed to have significant errors.* As already noted, these errors are partly due the narrow size spread and random noise inherent in the side-view HSV mass results. However, these errors are also partly due to the curve fitting procedures which, despite several attempts, experienced difficulties with cases where M_{avg} was significantly different than $\widetilde{M}_{avg}$.

The true mid-time size distributions probably have $r \approx 2/3$, consistent with the early- and late-time results. In fact, after eliminating the 7 tests that experienced severe random noise, Method 3 yields an average of $r = 0.68$. Including the 7 tests that experienced severe random noise, Method 3 yields an average of $r = 0.54$, which is still within 20% of $r = 2/3$.

The remainder of this subsection concerns fragment velocity distributions. As described in Section 3.2.1, the mid-range velocities were often obscured by smoke and fire. For example, Figure 49 shows the velocities derived from side-view HSV in Test 4. The mid-range velocity bins are nearly empty. As seen in Figure 50, this occurs because of smoke obscuration. As the smoke clears, the fragments become visible again, but, by this time, they are travelling substantially slower. In other words, before smoke obscuration, the video captures the fastest fragments that formed first near the center of the target, while after smoke obscuration, the video captures the slowest fragments that formed later, nearer the periphery of the target.

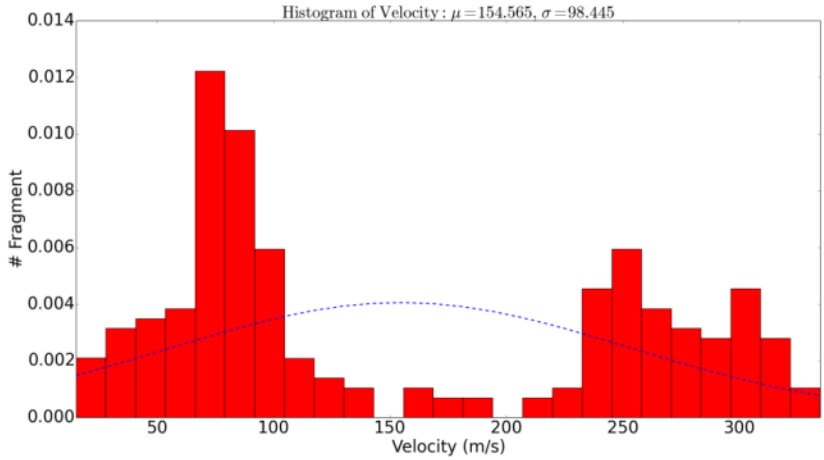

Figure 49. Velocity histogram for Tests 4 where the fireball obscures the view of mid-range velocity fragments.

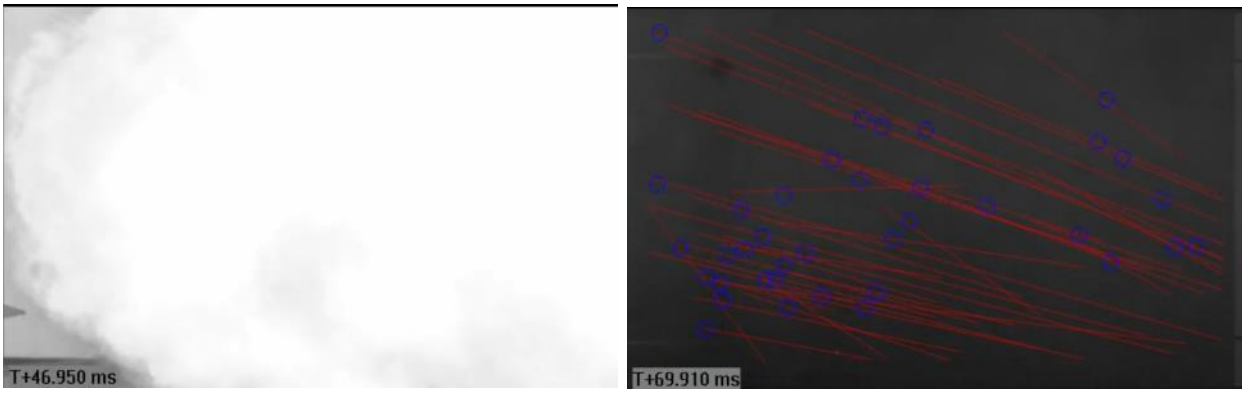

Figure 50. Screen captures from the rear-view HSV taken in Test 4 at 47-msec (left) and 69-msec (right) illustrate how smoke obscures video supporting the velocity measurements.

Because of obscuration and limited video resolution, the problems with the side-view HSV velocity data are probably as severe those of the side-view HSV mass data. However, because this is the only source of velocity data, a full set of side-view HSV velocity results is given with the caveat that *they are believed to have significant errors*. Only Weibull fits to velocity CDFs will be shown. Unlike mass, there is no known theoretical foundation for using Weibull distributions for velocity. Weibull distributed were used here for expediency and for consistency with the mass fits.

Figure 51 shows the best-fit Weibull velocity distribution for the combination of the five tests involving CMU (Tests 3, 4, 7, 10, and 12). Figure 52 shows the best-fit Weibull velocity distribution for the combination of the four tests involving tempered glass (Tests 13, 14, 15, and16). Figure 53 shows the best-fit Weibull velocity distributions for the combination of the four tests involving concrete (Tests 5, 6, 9 and 10). Finally, Figure 54 to Figure 66 show the best-fit Weibull velocity distributions for the thirteen individual tests. Table 12 shows the statistical parameters for each test.

Table 13 shows the Weibull fitting parameters.

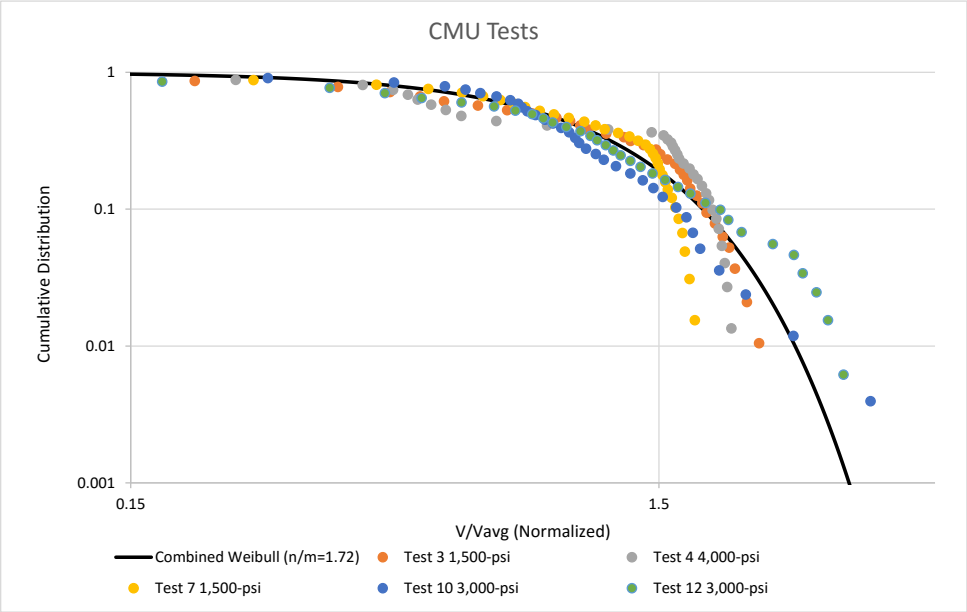

Figure 51. Best-fit Weibull velocity distribution for side-view HSV test data CDF for Tests 3, 4, 7, 10 and 12 involving CMU.

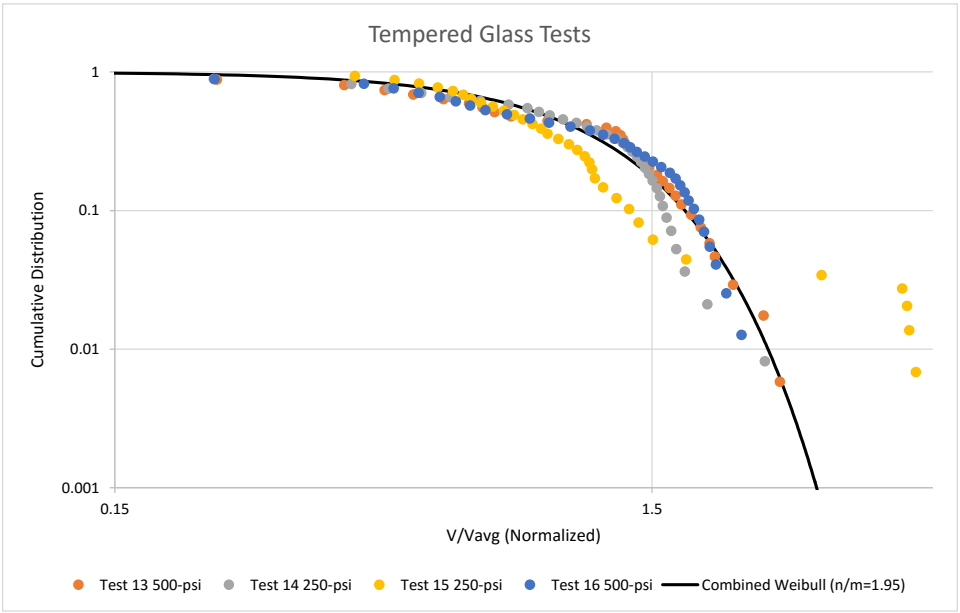

Figure 52. Best-fit Weibull velocity distribution for side-view HSV test data CDF for Tests 13-16 involving tempered glass.

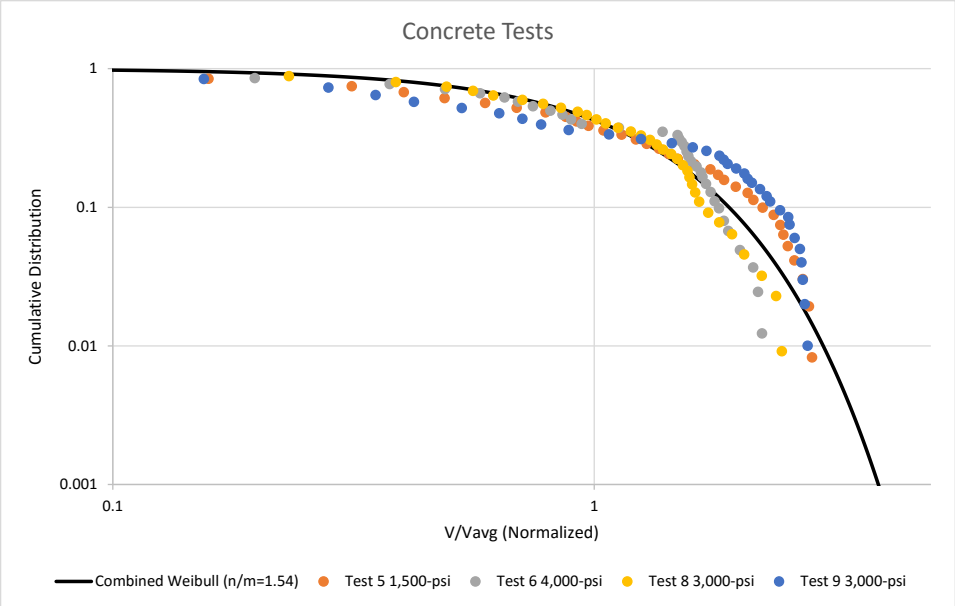

Figure 53. Best-fit Weibull velocity distribution for side-view HSV test data CDF for Tests 5, 6, 8, and 9 involving concrete.

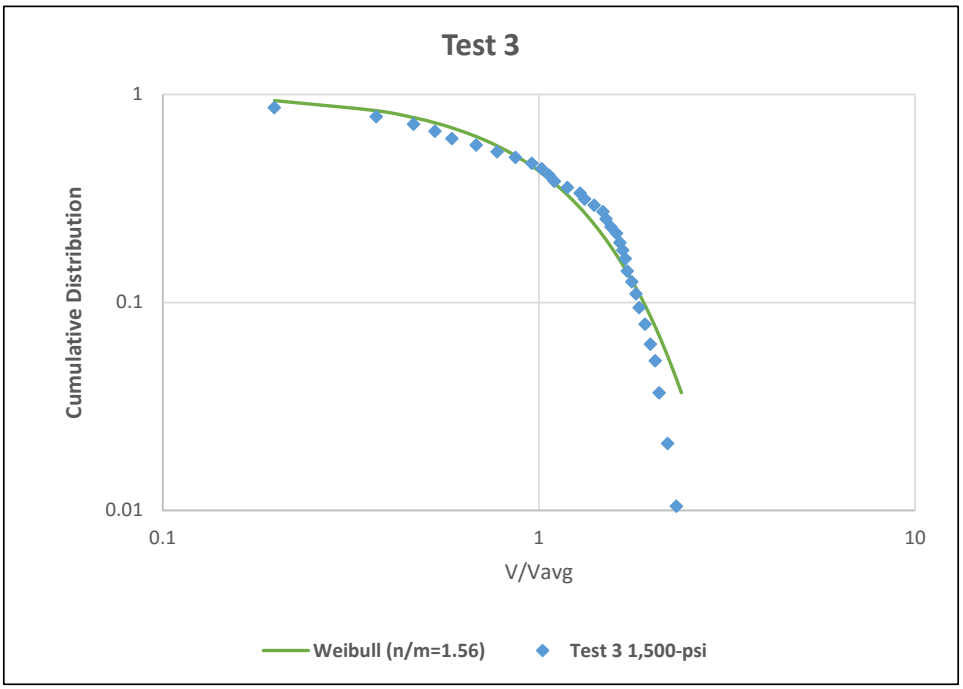

Figure 54. Best-fit Weibull velocity distribution for rear-view HSV test data for CDF for Test 3 involving CMU.

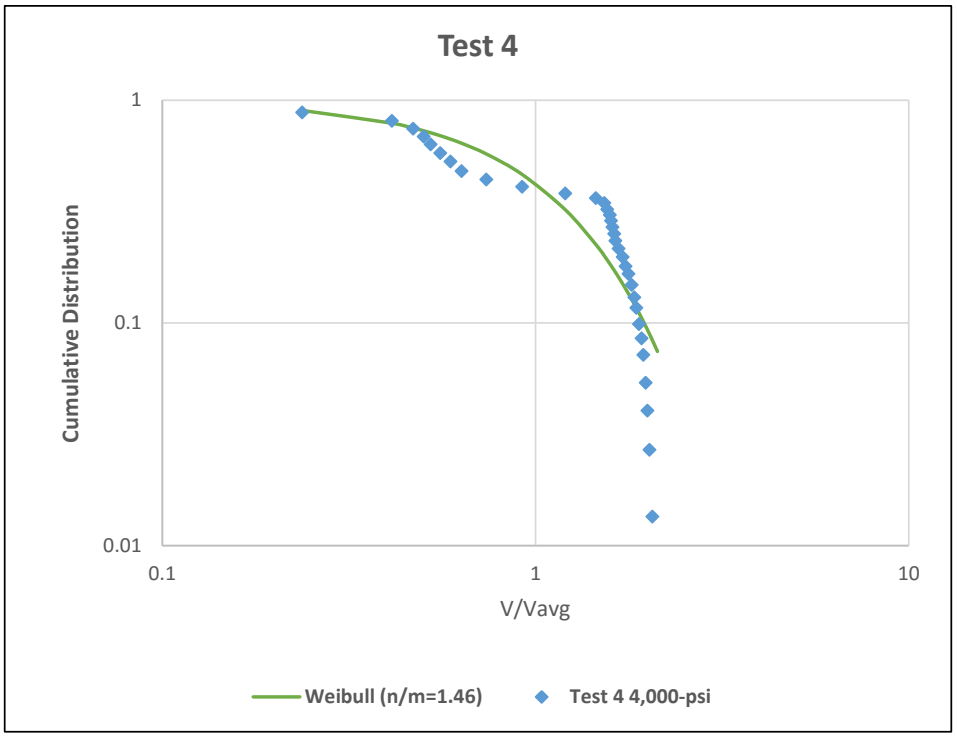

Figure 55. Best-fit Weibull velocity distribution for rear-view HSV test data for CDF for Test 4 involving CMU.

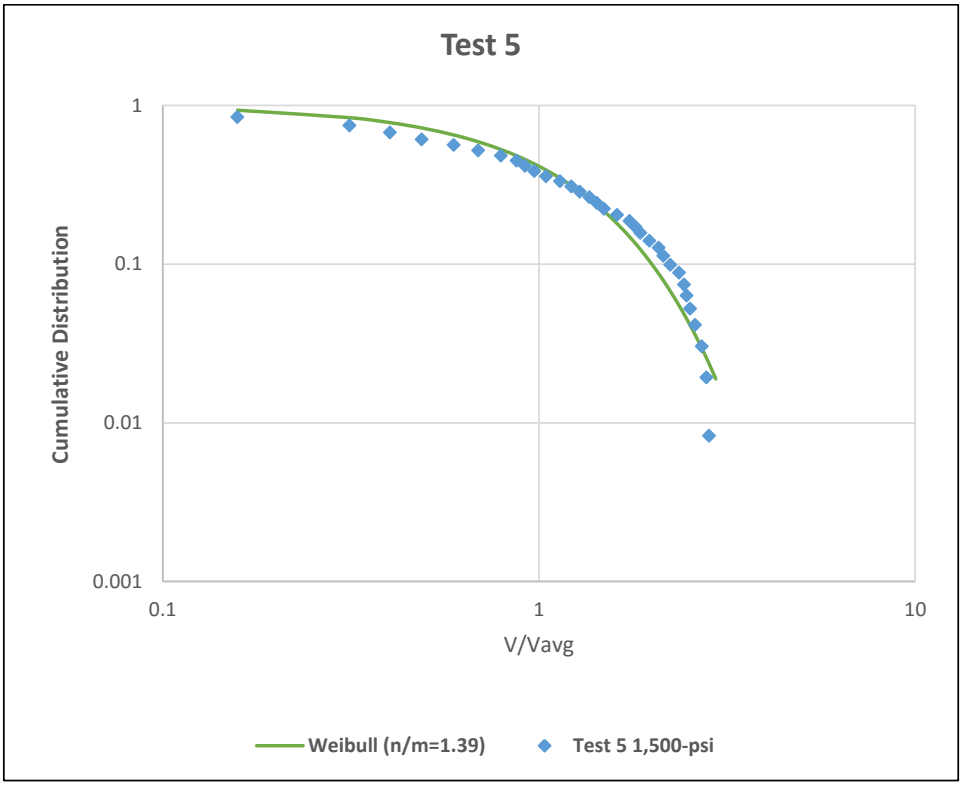

Figure 56. Best-fit Weibull velocity distribution for rear-view HSV test data for CDF for Test 5 involving concrete.

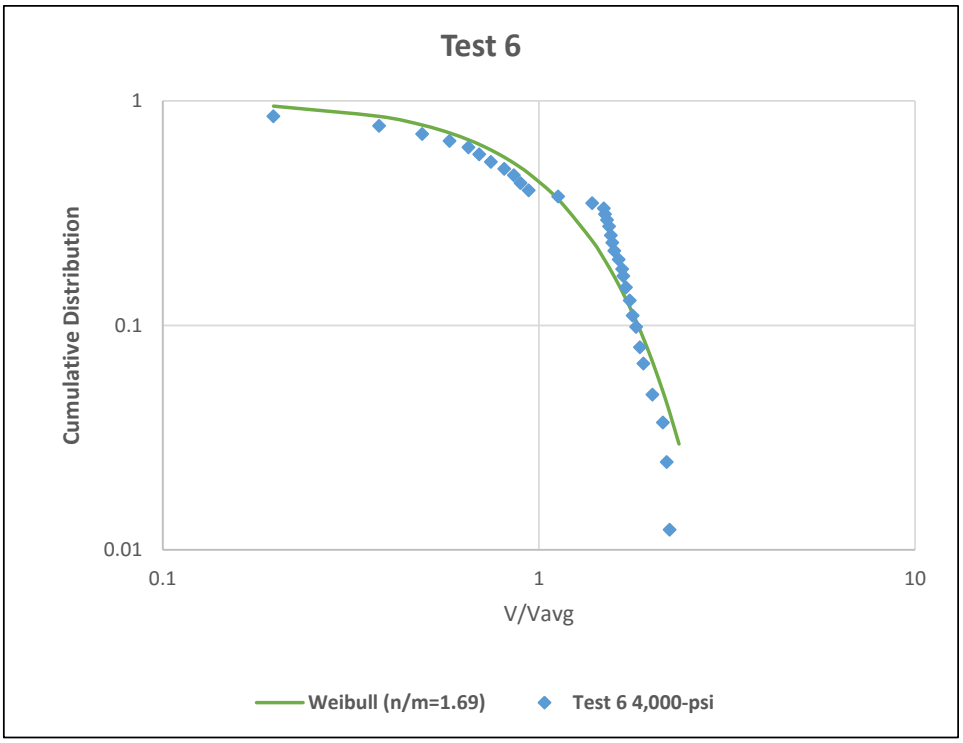

Figure 57. Best-fit Weibull velocity distribution for rear-view HSV test data for CDF for Test 6 involving concrete.

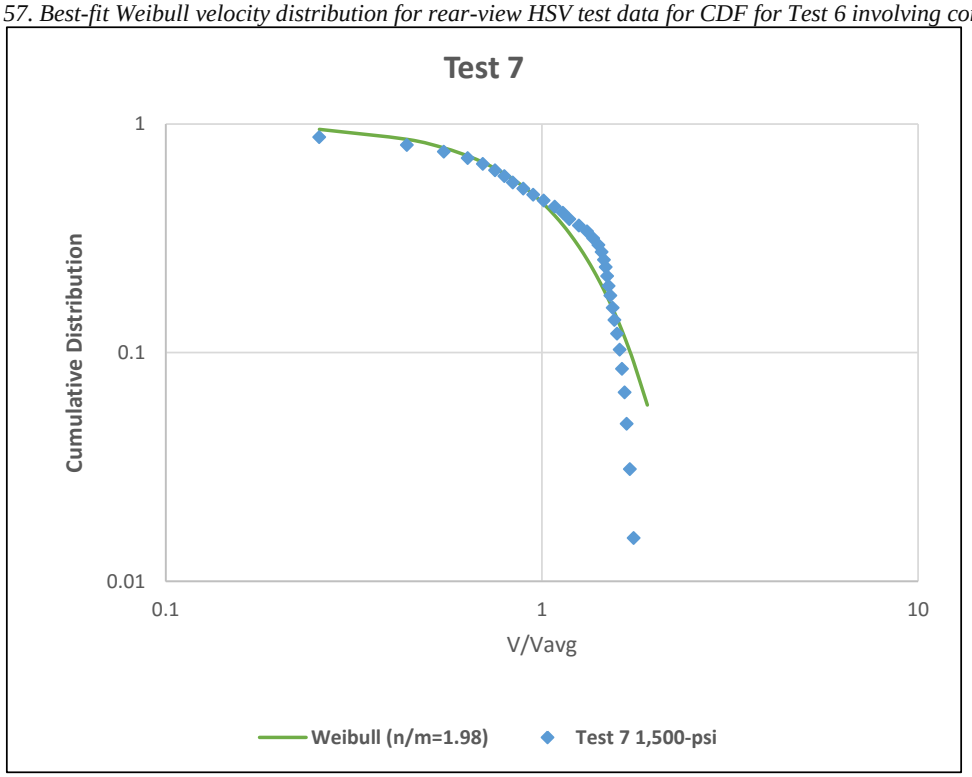

Figure 58. Best-fit Weibull velocity distribution for rear-view HSV test data for CDF for Test 7 involving CMU.

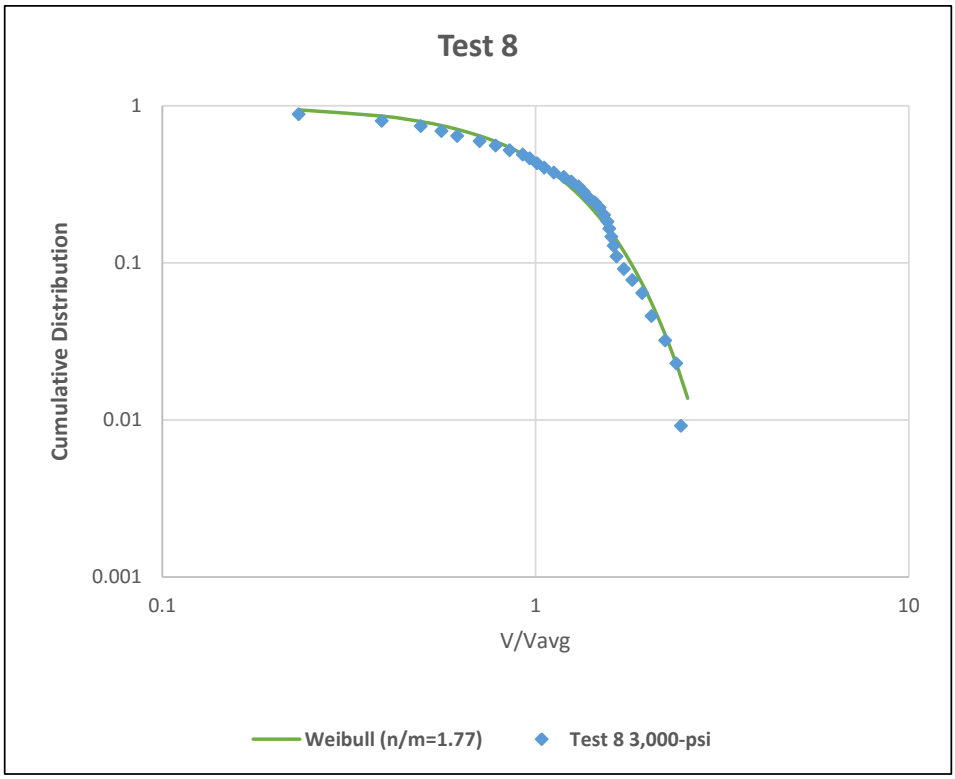

Figure 59. Best-fit Weibull velocity distribution for rear-view HSV test data for CDF for Test 8 involving concrete.

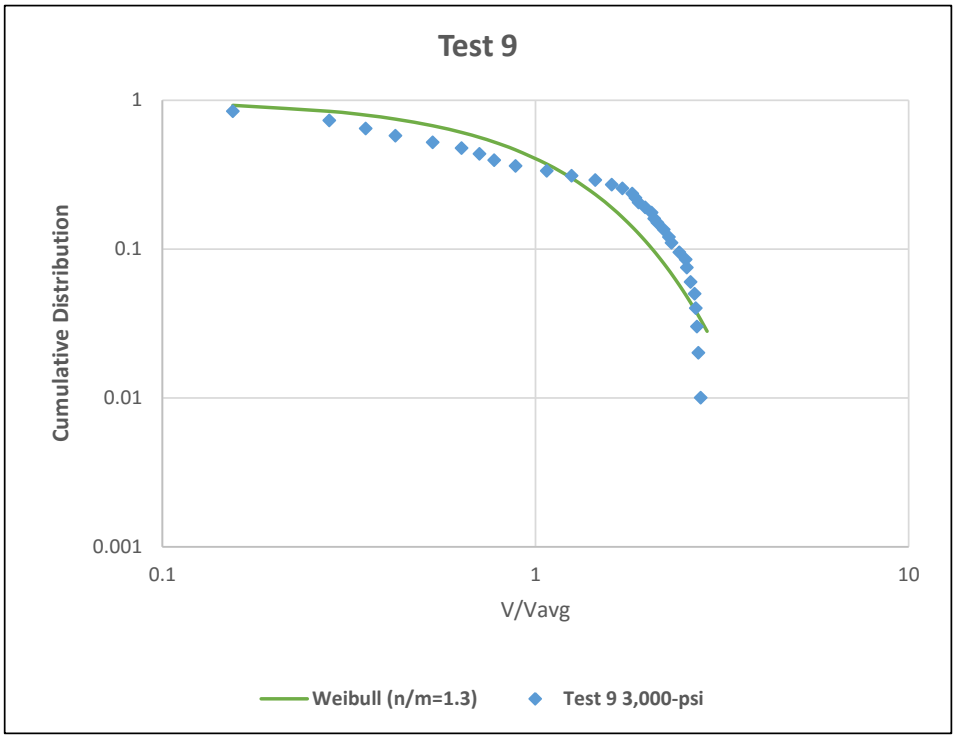

Figure 60. Best-fit Weibull velocity distribution for rear-view HSV test data for CDF for Test 9 involving concrete.

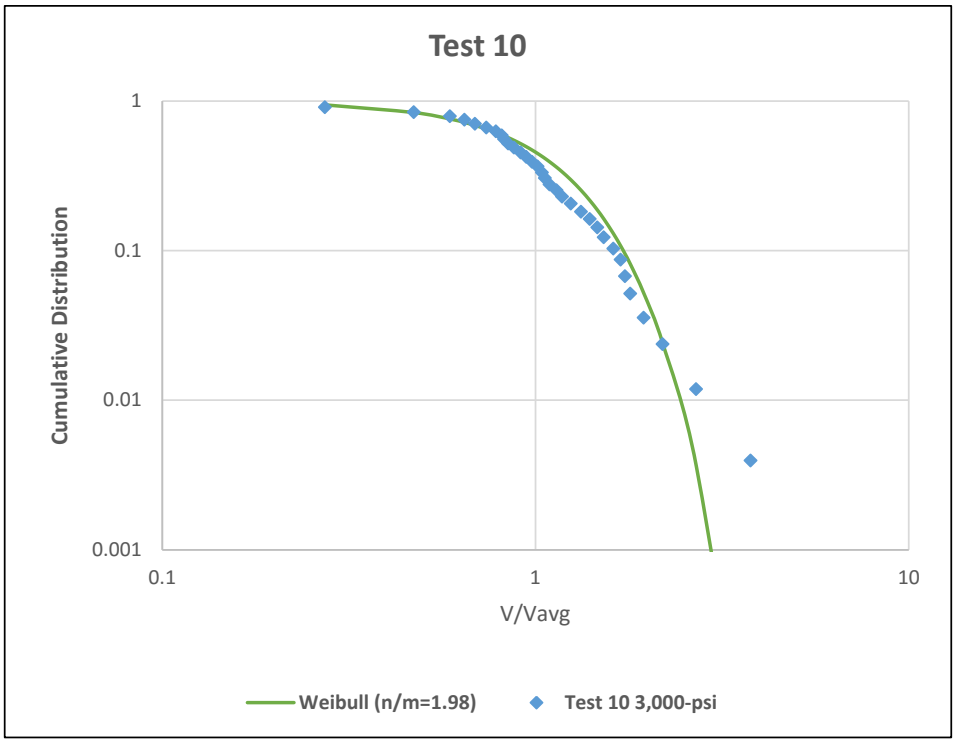

Figure 61. Best-fit Weibull velocity distribution for rear-view HSV test data for CDF for Test 10 involving CMU.

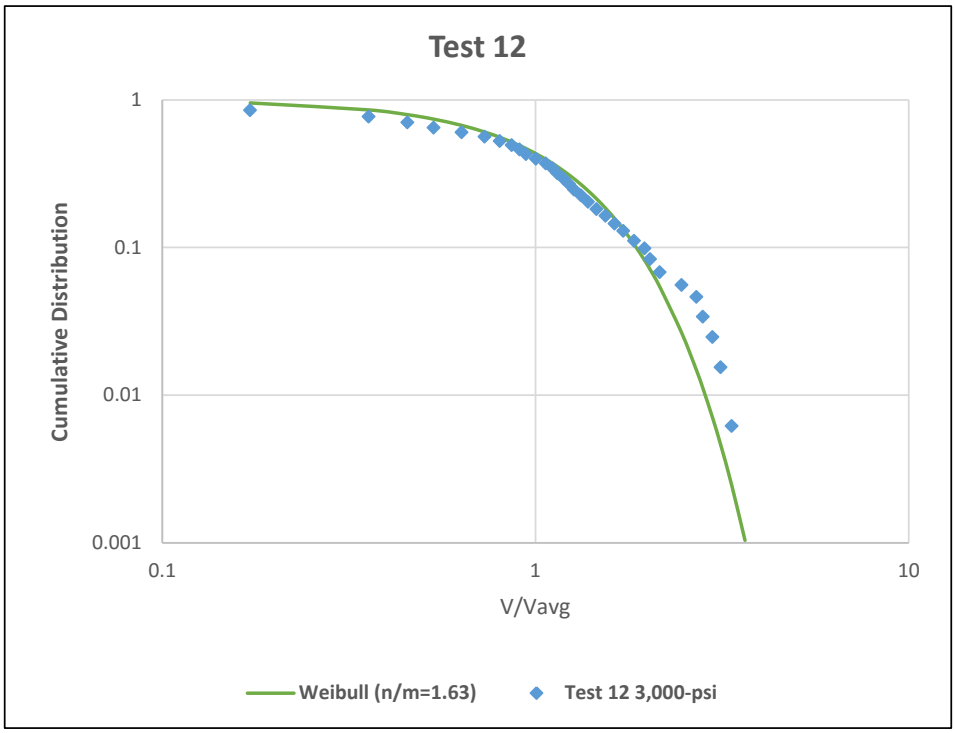

Figure 62. Best-fit Weibull velocity distribution for rear-view HSV test data for CDF for Test 12 involving CMU.

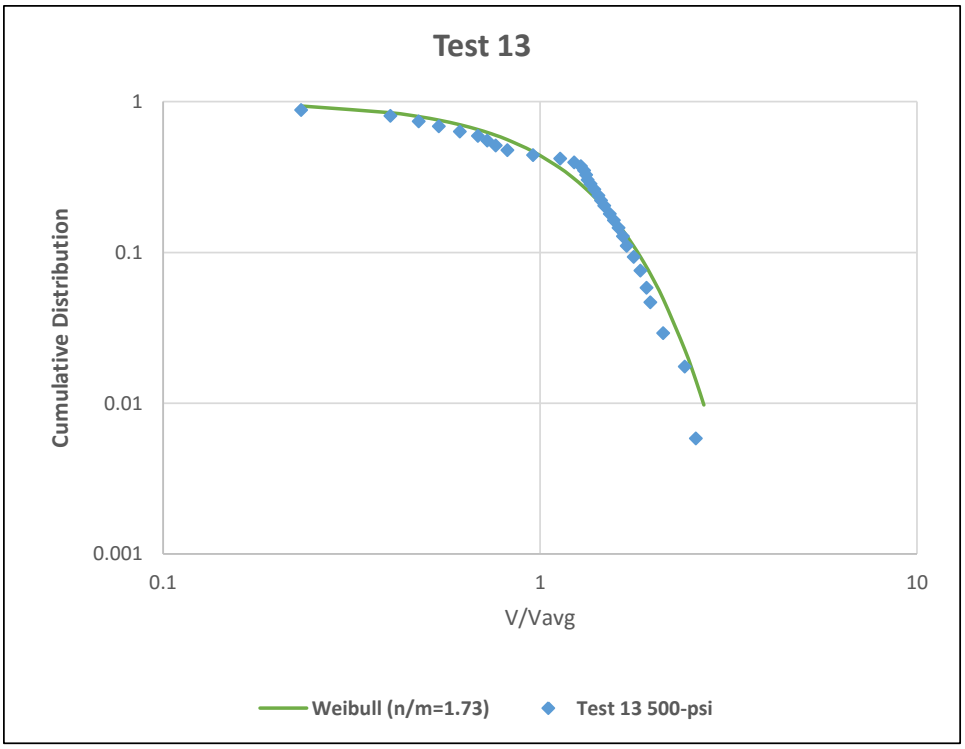

Figure 63. Best-fit Weibull velocity distribution for rear-view HSV test data for CDF for Test 13 involving tempered glass.

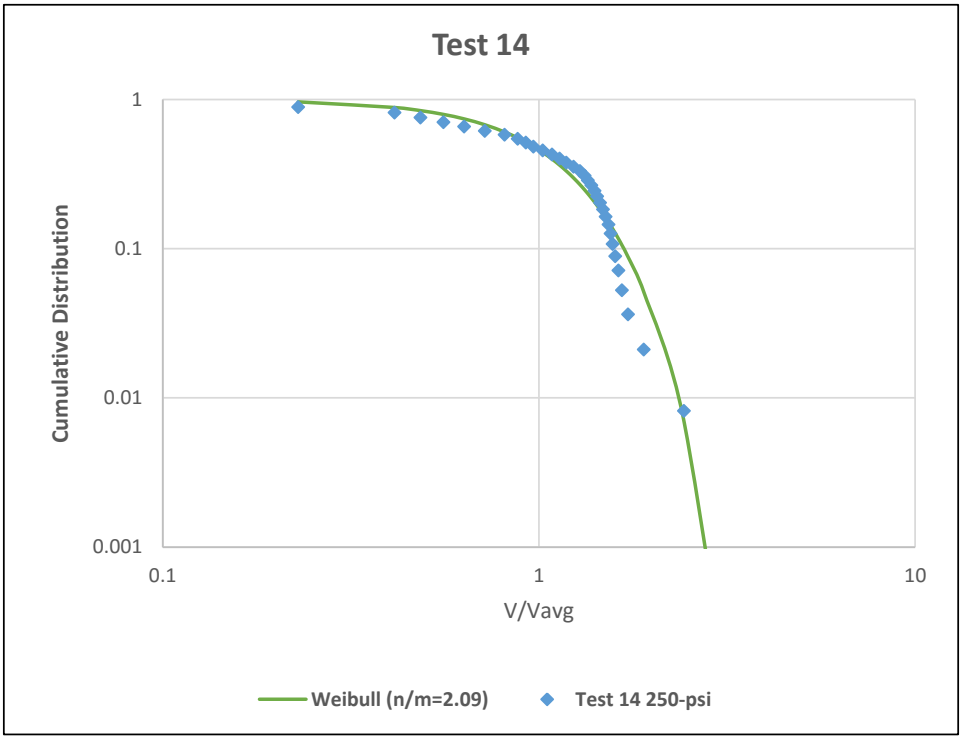

Figure 64. Best-fit Weibull velocity distribution for rear-view HSV test data for CDF for Test 14 involving tempered glass.

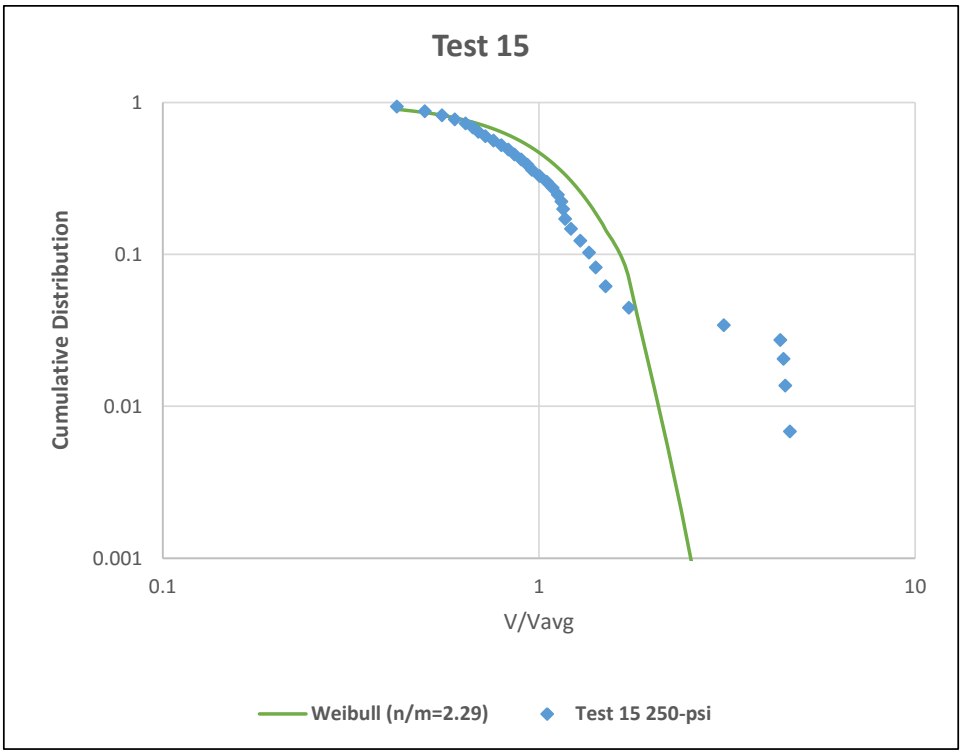

Figure 65. Best-fit Weibull velocity distribution for rear-view HSV test data for CDF for Test 15 involving tempered glass.

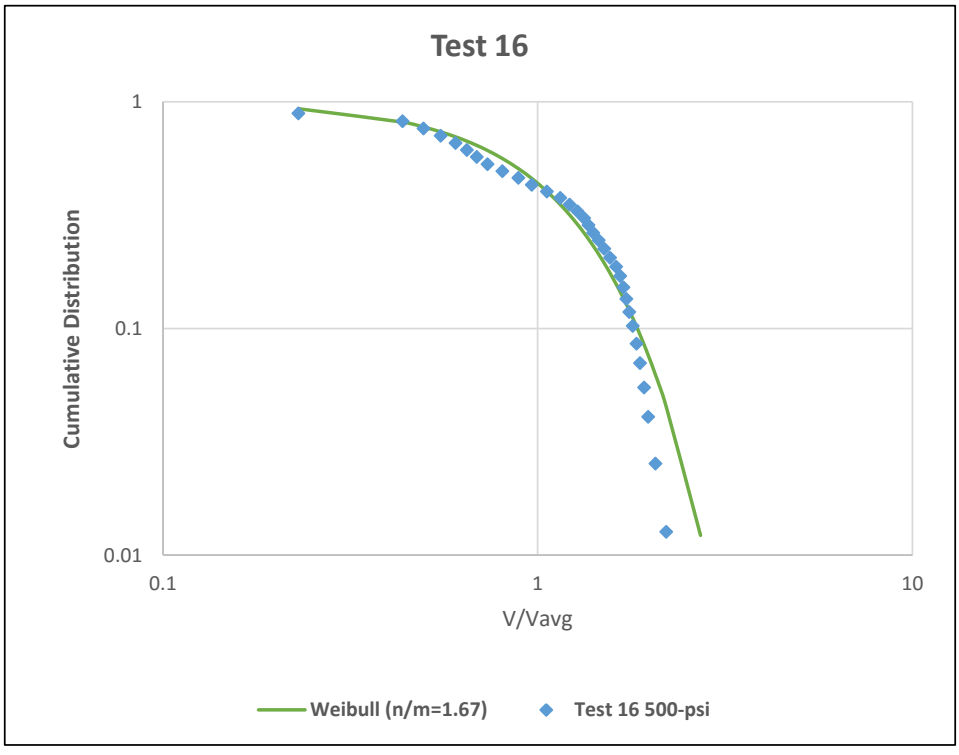

Figure 66. Best-fit Weibull velocity distribution for rear-view HSV test data for CDF for Test 16 involving tempered glass.

Table 12. Statistical parameters for side-view HSV velocity distributions.

Material	Test	# Frags Observed	V_{min} (m/s)	V_{max} (m/s)	$\tilde{V}_{avg}$ (m/s)
CMU	3	192	0	1000	97.7
	4	224	0	1000	154.6
	7	390	0	1000	118.2
	10	254	0	1000	60.5
	12	325	0	1000	65.6
Tempered Glass	13	173	0	1000	77.4
	14	856	0	1000	33.9
	15	293	0	1000	30.3
	16	712	0	1000	56.3
Concrete	5	364	0	1000	65.8
	6	164	0	1000	132.5
	8	220	0	1000	112.5
	9	201	0	1000	86.1

Table 13. Best-fit Weibull parameters based on side-view HSV velocity.

Material	Test	Weibull (r)	Fit Quality
CMU	3	1.56	Good
	4	1.46	Poor (oscillatory data)
	7	1.98	Fair (bi-linear data)
	10	1.98	Good
	12	1.63	Good
	Combined	1.72	
Tempered Glass	13	1.73	Good
	14	2.09	Fair (oscillatory data)
	15	2.29	Poor
	16	1.67	Fair (oscillatory data)
	Combined	1.94	
Concrete	5	1.39	Good
	6	1.69	Fair (oscillatory data)
	8	1.77	Good
	9	1.30	Fair (oscillatory data)
	Combined	1.53	

4.1.5 Mass Distributions from Physical Collection (Sieve) Analyses

This subsection describes the late-time mass distributions obtained from physical collection. Of the three measurement techniques used to characterize fragment size distributions, physical collection provided the highest quality data.

Before considering the usual PDFs and CDFs, it may be of some interest to view the test data in a different form, namely, mass histograms. Figure 67, Figure 68 and Figure 69 show physically collected mass histograms for select low vs high pressure tests on CMU, concrete and tempered glass, respectively. As expected, higher pressures generally lead to more small fragments.

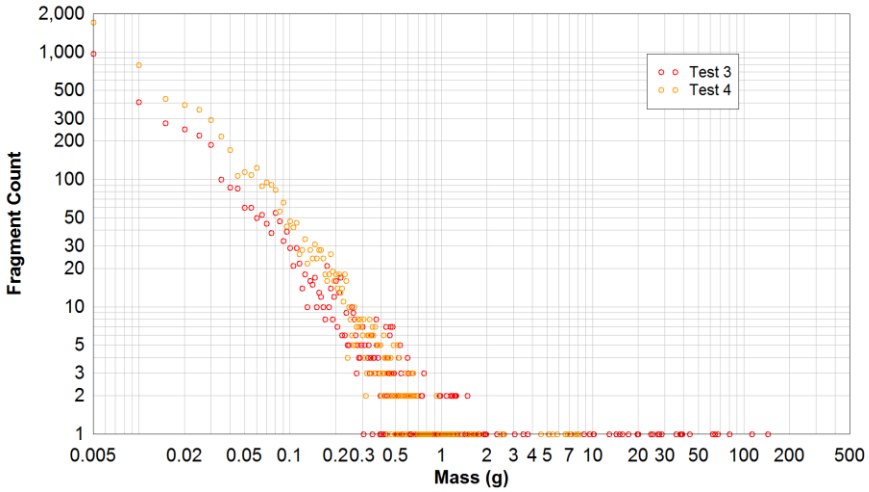

Figure 67. Histograms of physically-collected fragment mass for low (Test 3, ~1,500psi) vs. high (Test 4, ~4,000psi) peak static overpressure loads on CMU.

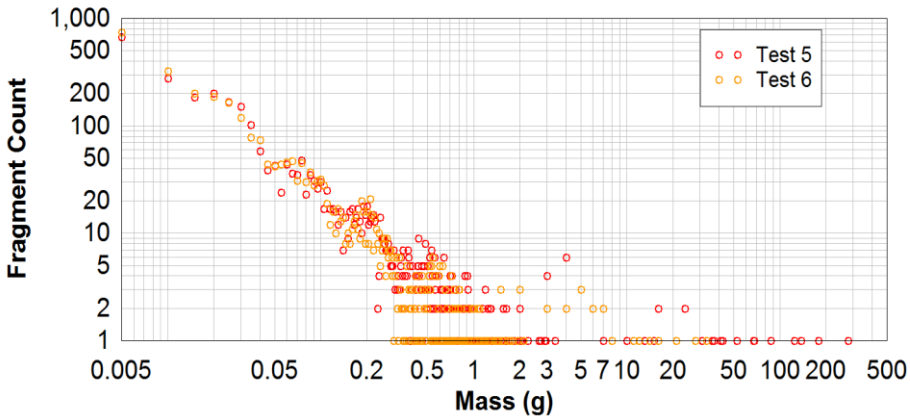

Figure 68. Histograms of physically-collected fragment mass for low (Test 5, ~1,500psi) vs. high (Test 6, ~4,000psi) peak static overpressure loads on concrete.

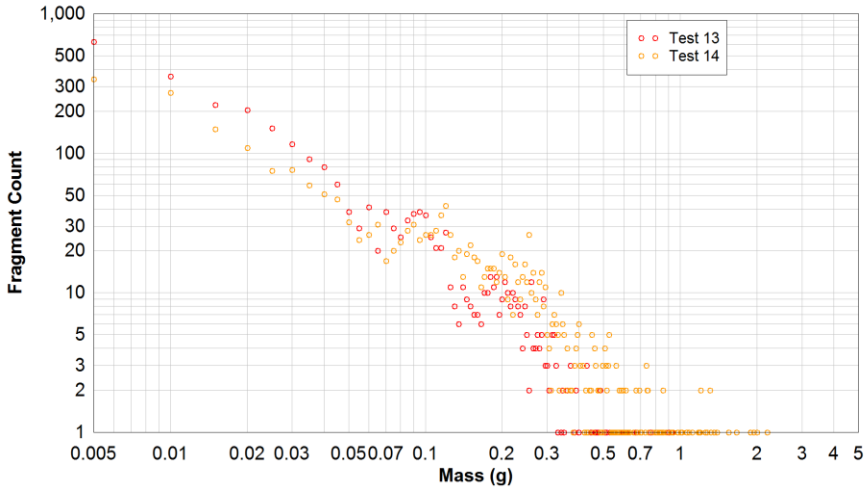

Figure 69. Histograms of physically-collected fragment mass for low (Test 14, ~250psi) vs. high (Test 13, ~500psi) peak static overpressure loads on tempered glass.

Table 14 summarizes the physically-collected fragmentation data. Notice that $M_{min} = 0.01\text{g}$ for all tests. While smaller fragments were measured, the results were not considered reliable. Also notice that M_{max} is the upper limit of the largest size bin, which was chosen to be somewhat larger than the largest observed fragment. Finally notice that the practical mass range is 2.5 to 3 orders-of-magnitude, significantly larger than that obtained with the early- and mid-time measurement techniques.

Table 14. Statistical parameters for physically-collected fragment mass distributions.

Material	Test	Pressure (psi)	# Frags Observed	Total Mass Observed (g)	M_{max} (g)	M_{max} (g)	$\widetilde{M}_{avg}$ (g)
CMU	3	Low (1,500)	4,520	1,661	0.01	8	0.127
	4	High (4,000)	7,481	491	0.01	5	0.085
	7	Low (1,500)	8,367	1,611	0.01	15	0.150
	10	Med (3,000)	6,779	649	0.01	5	0.076
	12	Med (3,000)	6,576	649	0.01	3	0.091
Tempered Glass	13	High (500)	3,967	163	0.01	1.6	0.067
	14	Low (250)	3,967	387	0.01	3	0.149
	15	Low (250)	3,579	310	0.01	3	0.144
	16	High (500)	3,703	190	0.01	3	0.094
Concrete	5	Low (1,500)	4,831	2,286	0.01	16	0.187
	6	High (4,000)	3,751	678	0.01	5	0.124
	8	Med (3,000)	3,905	877	0.01	5	0.096
	9	Med (3,000)	4,564	1,133	0.01	9	0.171

A number of different *ad hoc* fitting procedures were attempted over a period of two years.

Table 15 compares the results of three of those attempts. Method 1 excluded many of the small fragments and was based on a measurement technique that sometimes incorrectly counted two adjacent small fragments as one larger fragment. As a result, Method 1 generally overestimated M_{avg}. Method 2 included more of the small fragments and was based on an improved measurement technique that correctly separated adjacent fragments. In general, in Method 2, M_{avg} is the roughly the same as $\widetilde{M}_{avg}$. However, the improved measurement technique introduced new oscillations in the PDF near $\widetilde{M}_{avg}$, which adversely affected the accuracy of the fitting procedure. Method 3 was an attempt to improve on Method 2 by automatically optimizing both *r* and M_{avg} using MS Excel macros.

In Table 15, green shading indicates which of the three methods obtained the best result, as judged by the errors in various views and by other metrics. Method 2 was the most successful overall. However, in 3 of 13 tests, Method 1 obtained significantly better results than Method 2. Method 3, the last and supposedly best attempt, obtained somewhat worse results than the earlier attempts.

Notice that the Weibull exponents are confined to a relatively narrow range, i.e., *r* varies between 0.46 and 0.76 with an average of about 0.61. After selecting the best result among the three methods, the range is much narrower, i.e., *r* varies between 0.58 and 0.67 with an average of about 0.64. This raises the possibility that all 13 tests may have obtained the same normalized fragment size distribution with $r \approx 2/3$. This is a remarkable result given the major differences in material type and applied loading. This is also, to some extent, a frustrating result, given that this test series was specifically intended to produce a range of different fragment size distributions.

Table 15. Best-fit Weibull parameters based on physically-collected fragment mass data.

Material	Test	Pressure	Weibull parameters						
			Method 1 (Feb 2015) [10]		Method 2 (Jul 2016)		Method 3 (Sep 2016)		"Best"
			r	M_{avg} (g)	r	M_{avg} (g)	r	M_{avg} (g)	r
CMU	3	Low (1,500)	0.50	0.431	0.61	0.123	0.59	0.188	0.61
	4	High (4,000)	0.64	0.077	0.64	0.085	0.59	0.066	0.64
	7	Low (1,500)	0.57	0.238	0.62	0.135	0.58	0.193	0.62
	10	Med (3,000)	0.76	0.104	0.67	0.076	0.76	0.096	0.66
	12	Med (3,000)	0.66	0.105	0.56	0.102	0.73	0.098	0.66
	Combined				0.62		0.65		
Glass	13	High (500)	0.69	0.060	0.64	0.046	0.61	0.041	0.64
	14	Low (250)	0.68	0.128	0.65	0.119	0.65	0.098	0.68
	15	Low (250)	0.67	0.141	0.56	0.109	0.50	0.087	0.67
	16	High (500)	0.65	0.091	0.57	0.066	0.50	0.051	0.65
	Combined				0.61		0.57		
Concrete	5	Low (1,500)	0.46	0.730	0.65	0.152	0.57	0.209	0.65
	6	High (4,000)	0.51	0.222	0.66	0.124	0.60	0.181	0.66
	8	Med (3,000)	0.56	0.246	0.63	0.096	0.57	0.164	0.63
	9	Med (3,000)	0.47	0.264	0.58	0.148	0.52	0.221	0.58
	Combined				0.63		0.57		
Average			0.60	0.218	0.62	0.106	0.60	0.130	0.64

All of the following results were obtained with Method 2 applied to the physically-collected fragments. Figure 70 shows the best-fit Weibull size distribution for the five CMU tests combined. Similarly, Figure 71 shows the best-fit Weibull size distribution for the four plate glass tests combined. Finally, Figure 72 show the best-fit Weibull size distributions for the four concrete tests combined. These three figures support the notion that all 13 tests obtained the same fragment size distribution, after normalizing by the count mean mass. For additional detail, Figure 73 through Figure 85 show the best-fit Weibull size distributions for the 13 individual tests.

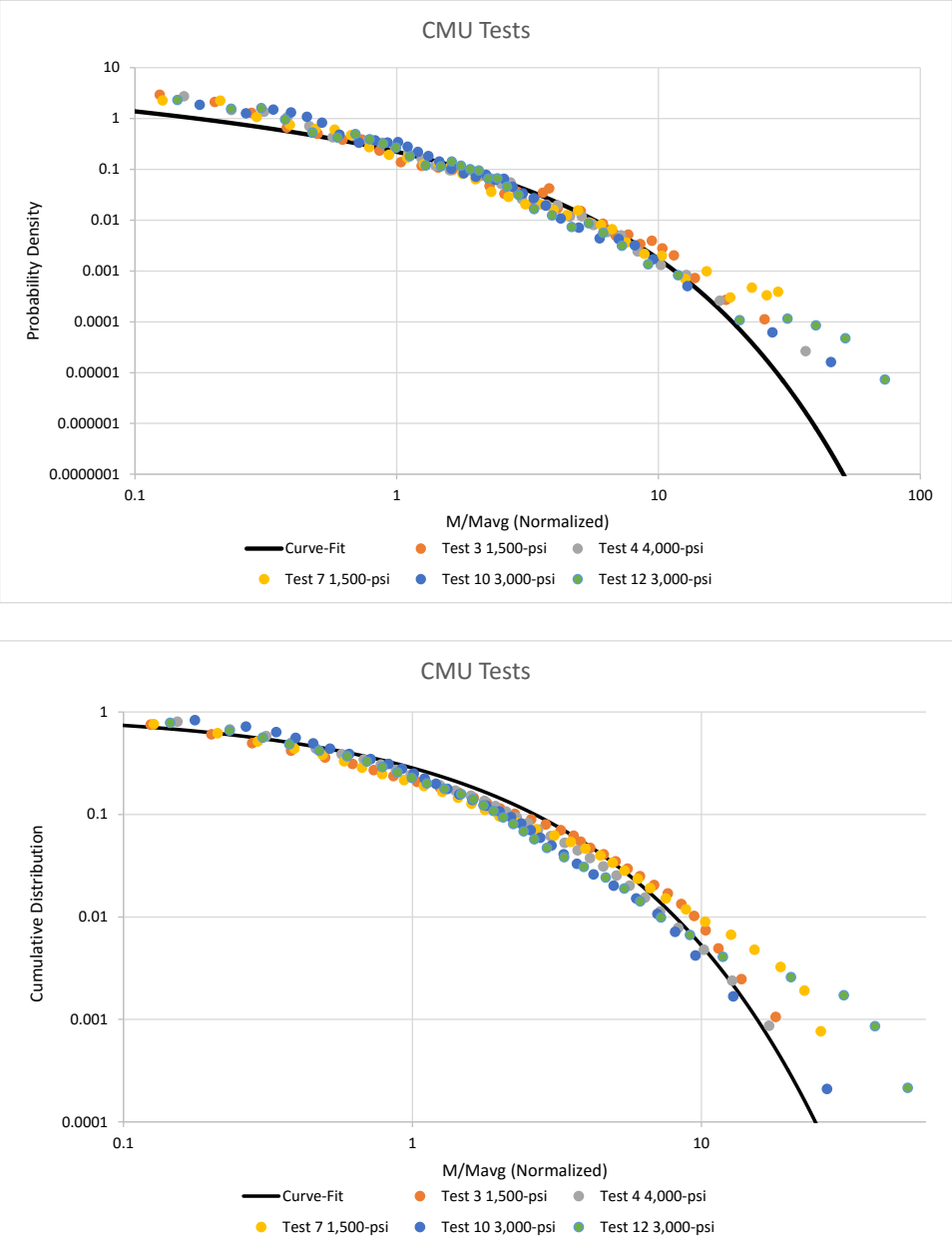

Figure 70. Best-fit Weibull mass distribution for physically-collected test data for PDF (top) and CDF (bottom) for Tests 3, 4, 7, 10 and 12 involving CMU.

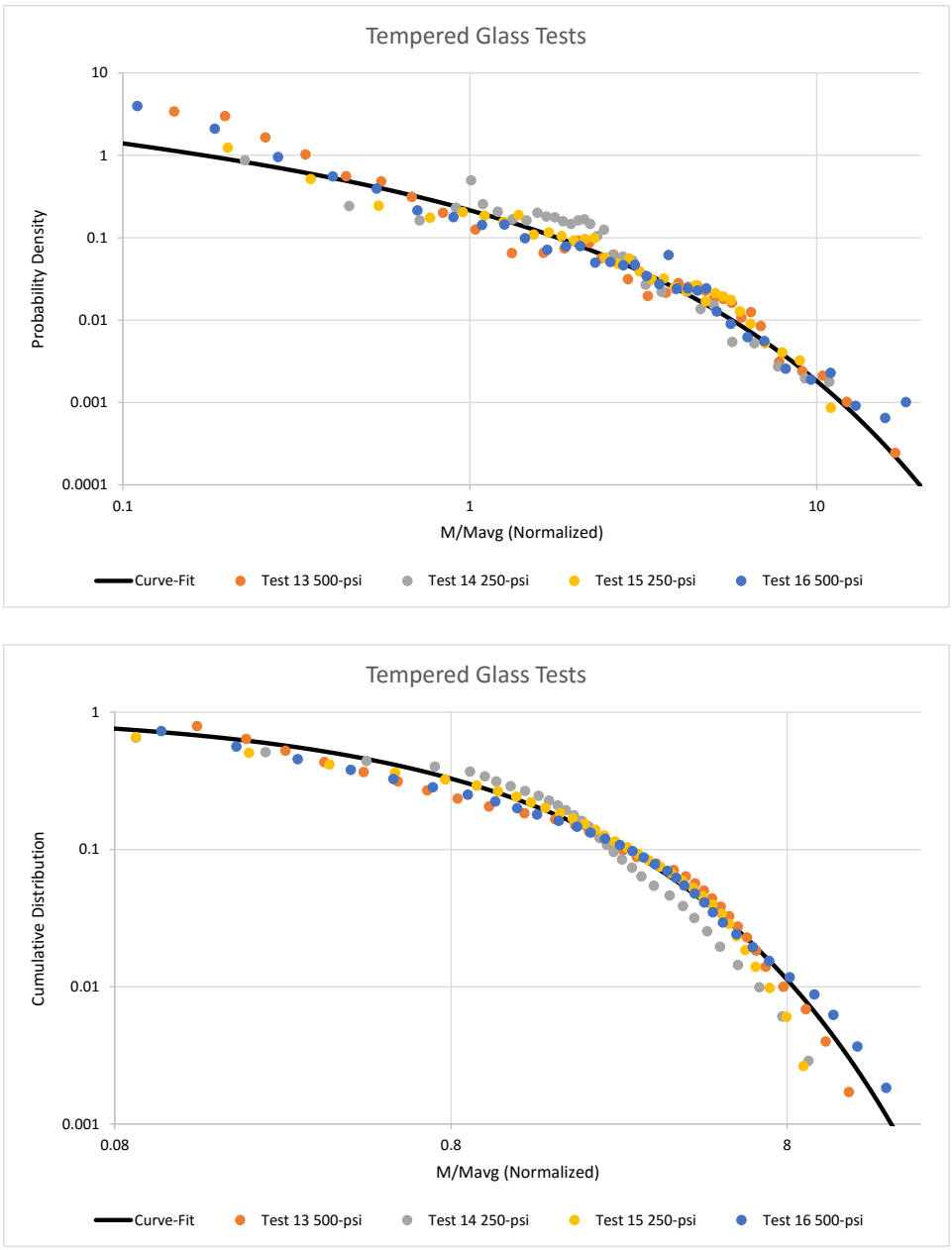

Figure 71. Best-fit Weibull mass distribution for physically-collected test data for PDF (top) and CDF (bottom) for Tests 13-16 involving tempered glass.

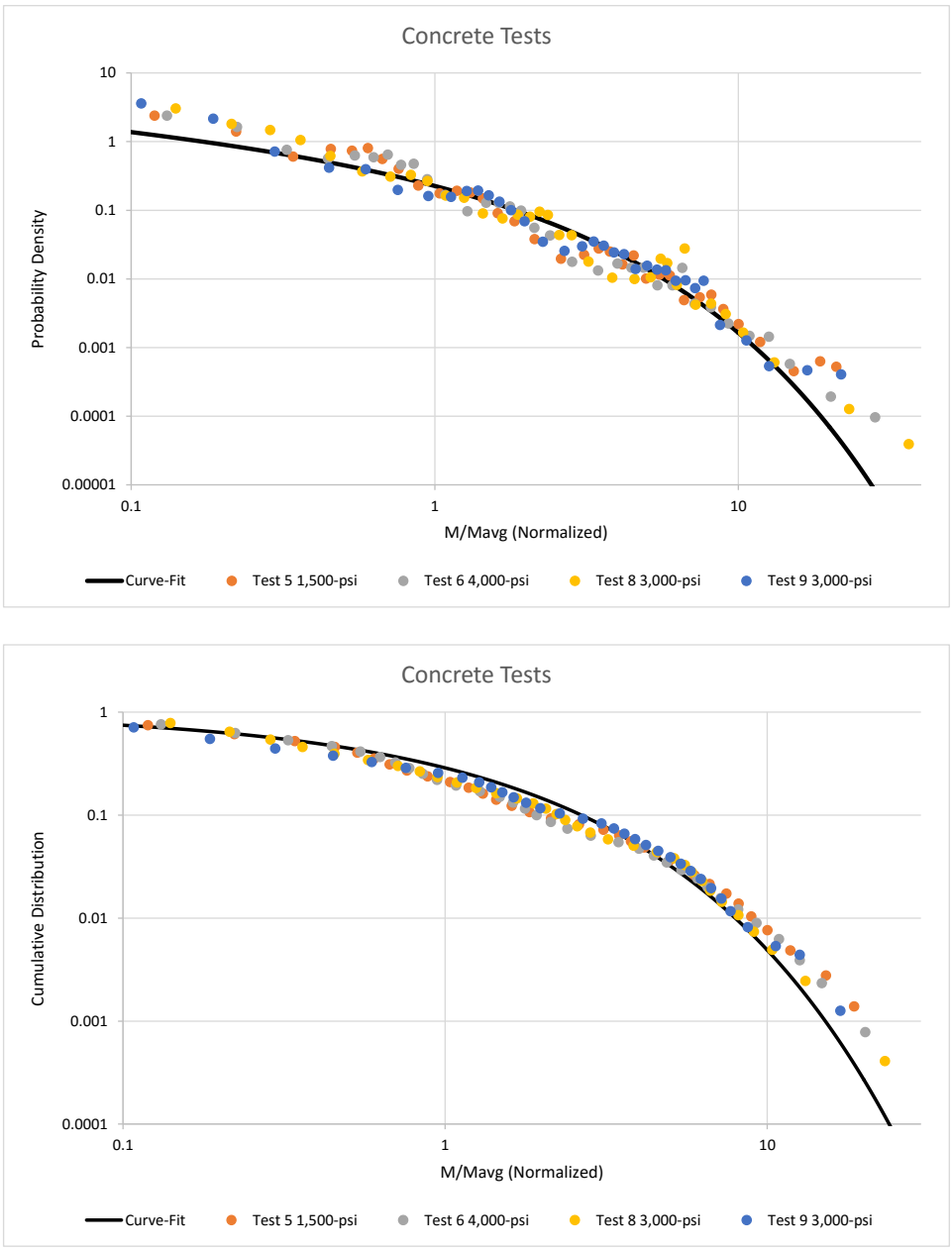

Figure 72. Best-fit Weibull mass distribution for physically-collected test data for PDF (top) and CDF (bottom) for Tests 5, 6, 8, and 9 involving concrete.

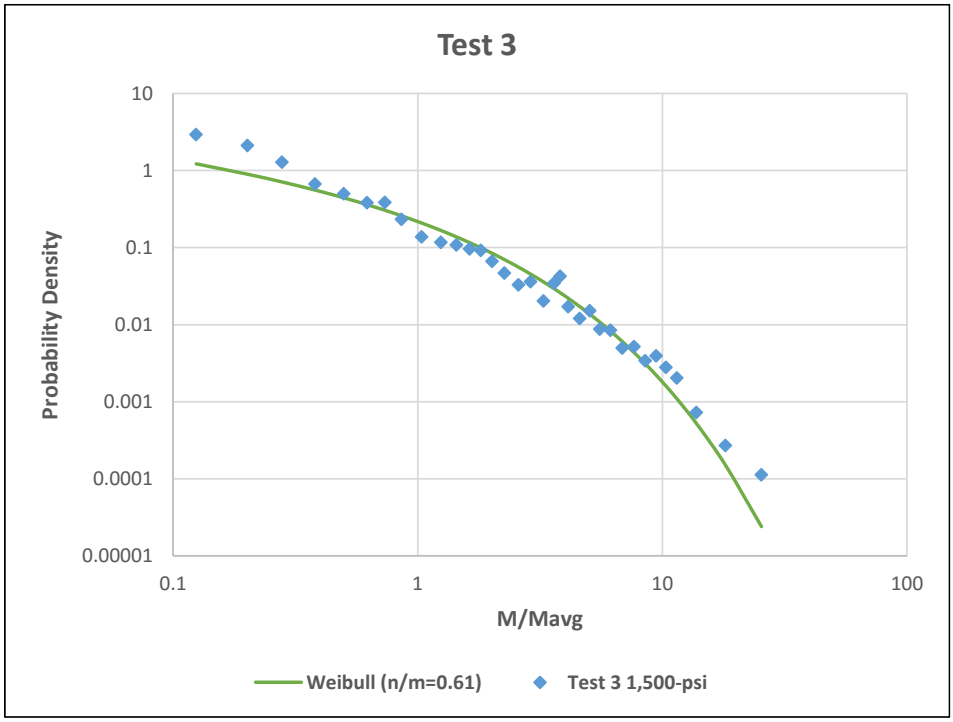

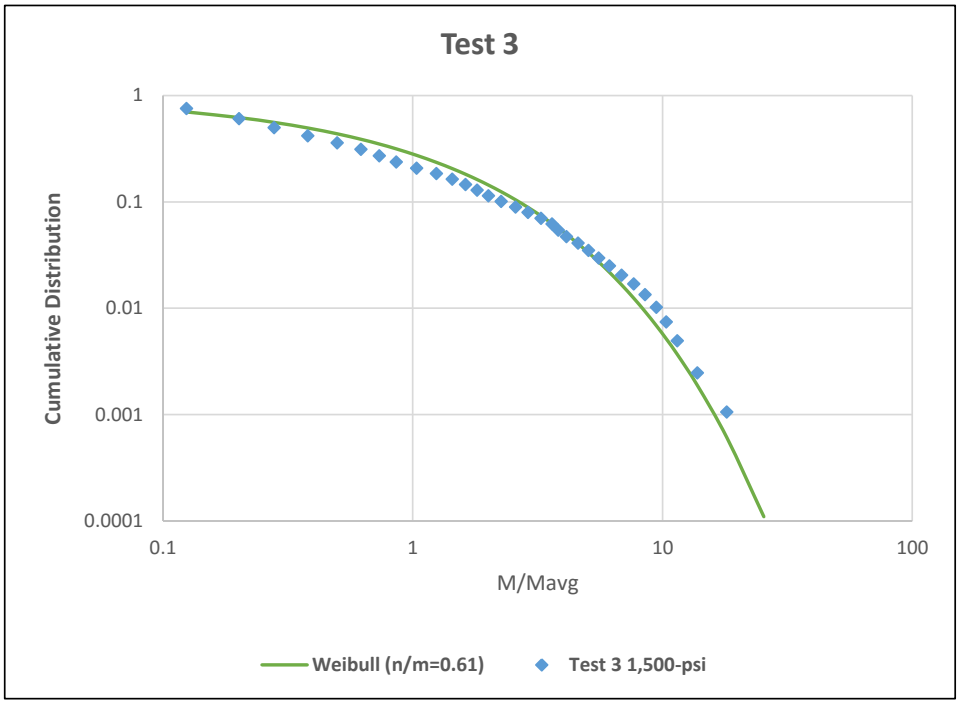

Figure 73. Best-fit Weibull mass distribution for physically-collected test data for PDF (top) and CDF (bottom) for Test 3 involving CMU.

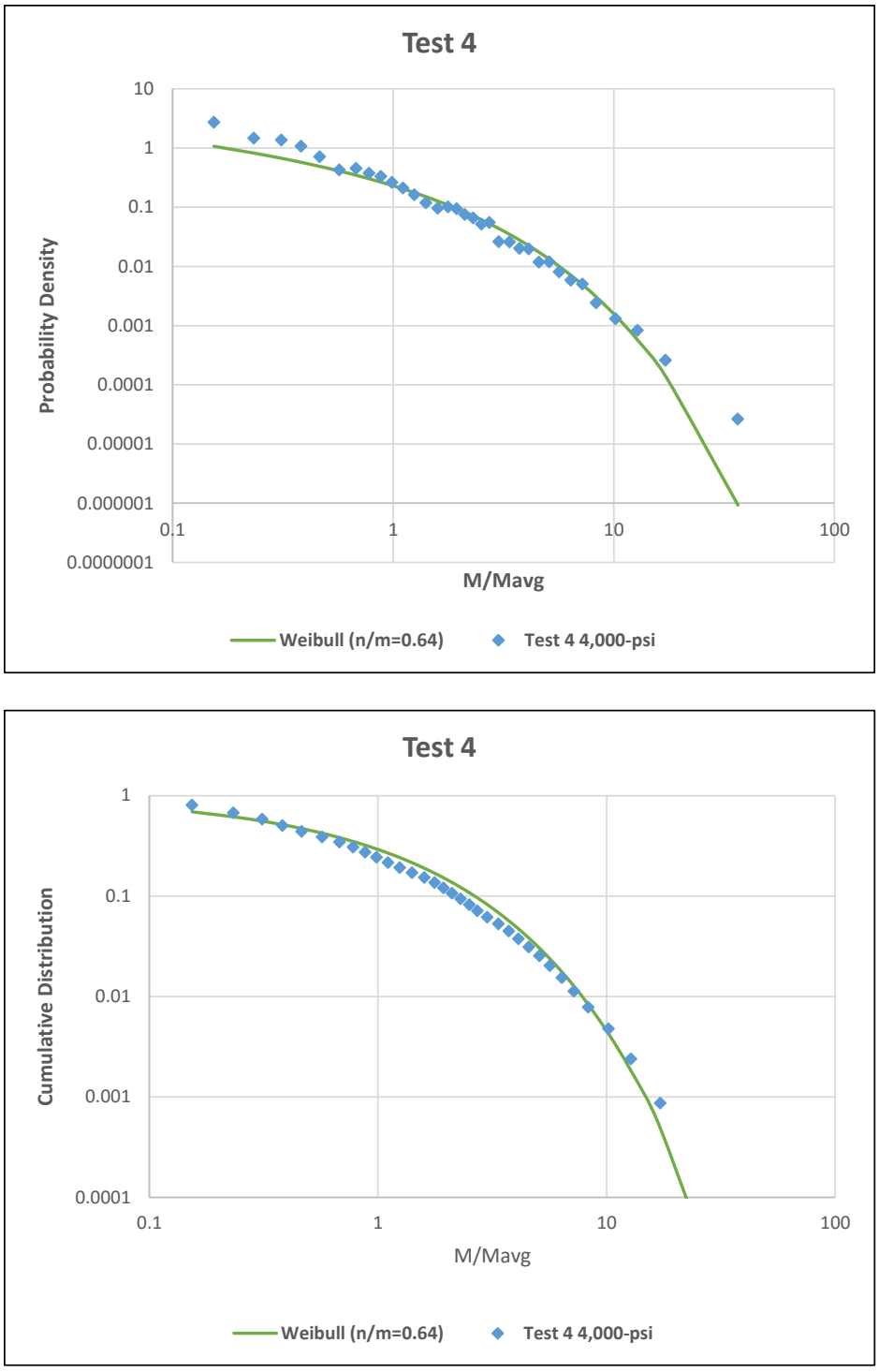

Figure 74. Best-fit Weibull mass distribution for physically-collected test data for PDF (top) and CDF (bottom) for Test 4 involving CMU.

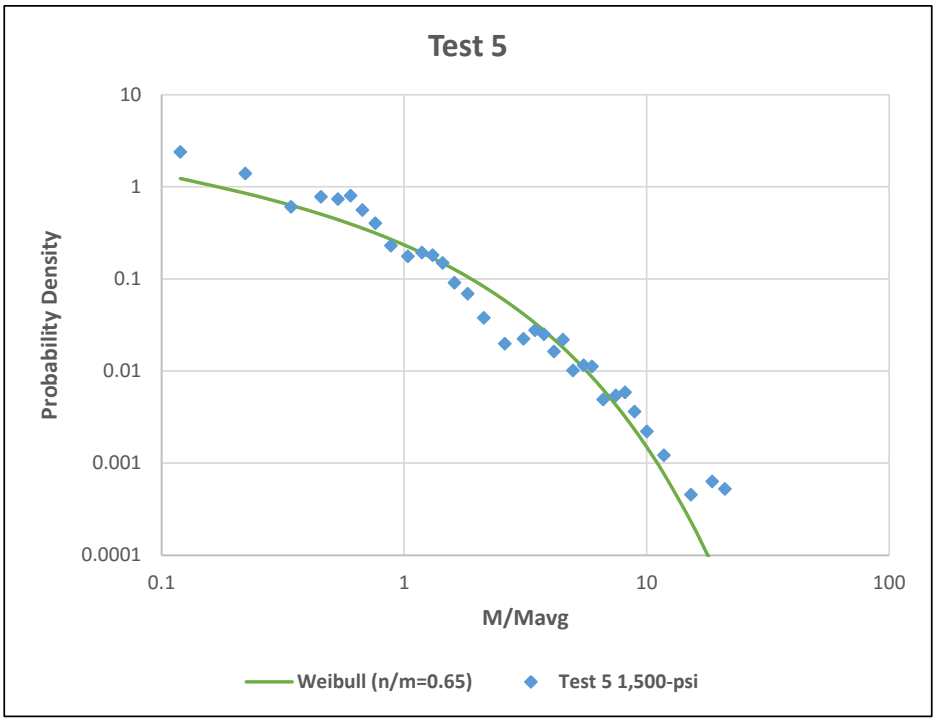

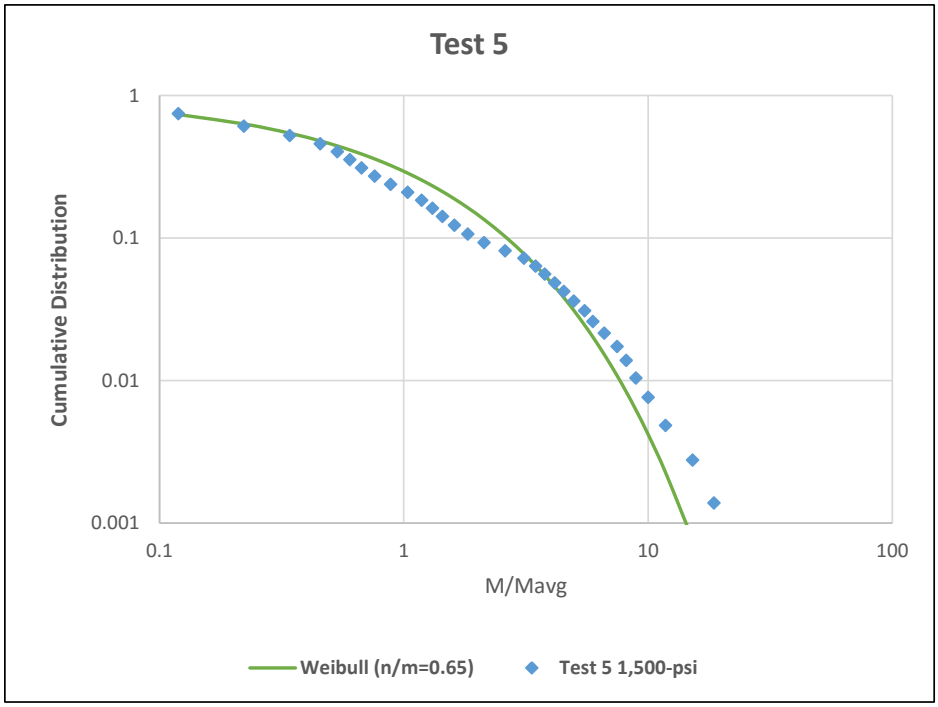

Figure 75. Best-fit Weibull mass distribution for physically-collected test data for PDF (top) and CDF (bottom) for Test 5 involving concrete.

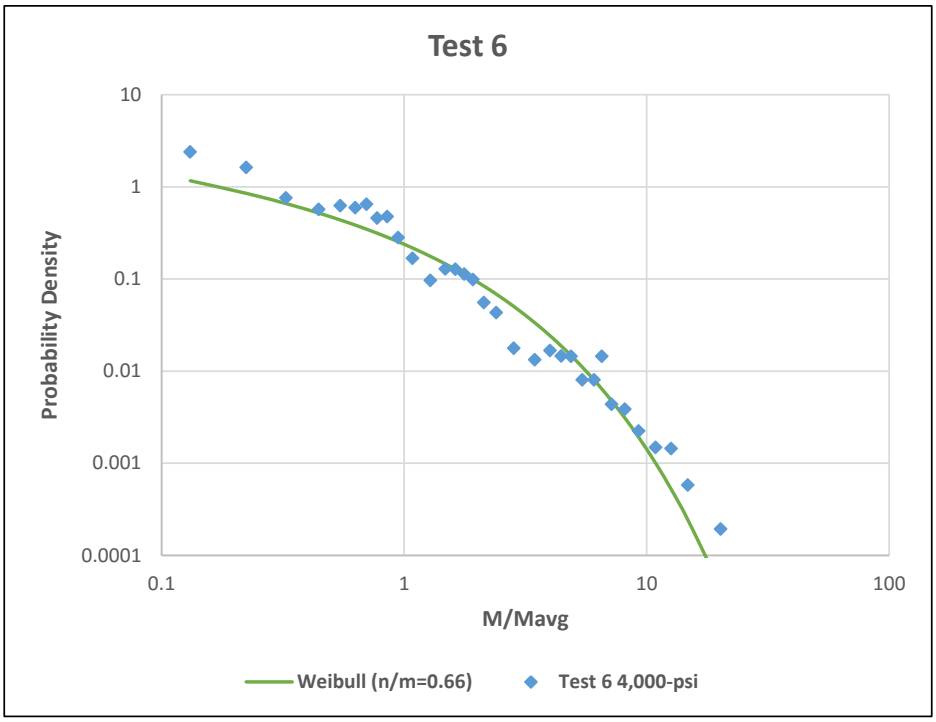

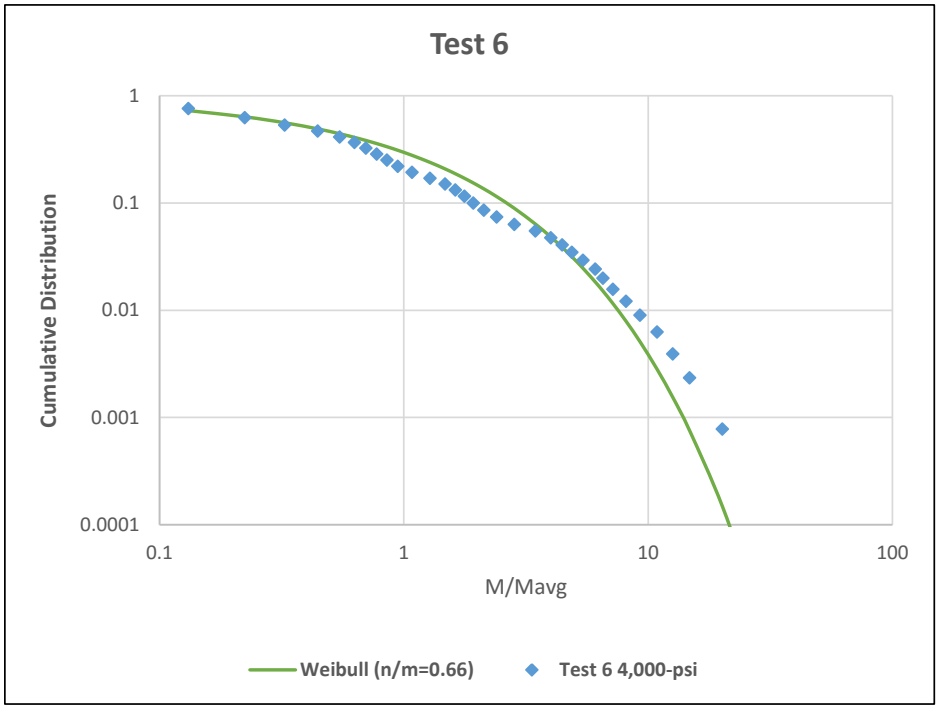

Figure 76. Best-fit Weibull mass distribution for physically-collected test data for PDF (top) and CDF (bottom) for Test 6 involving concrete.

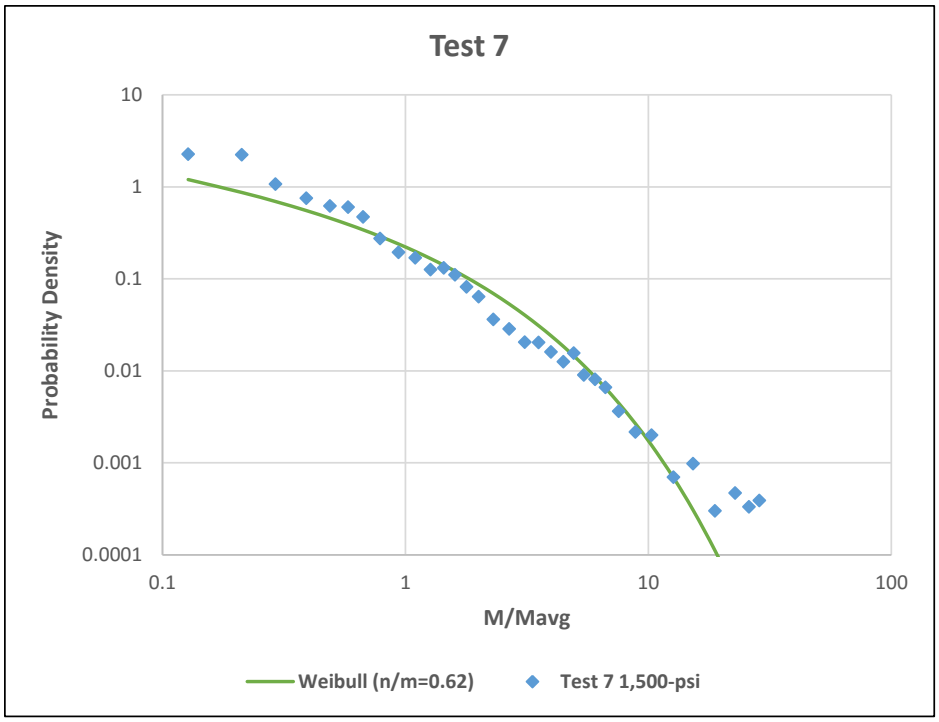

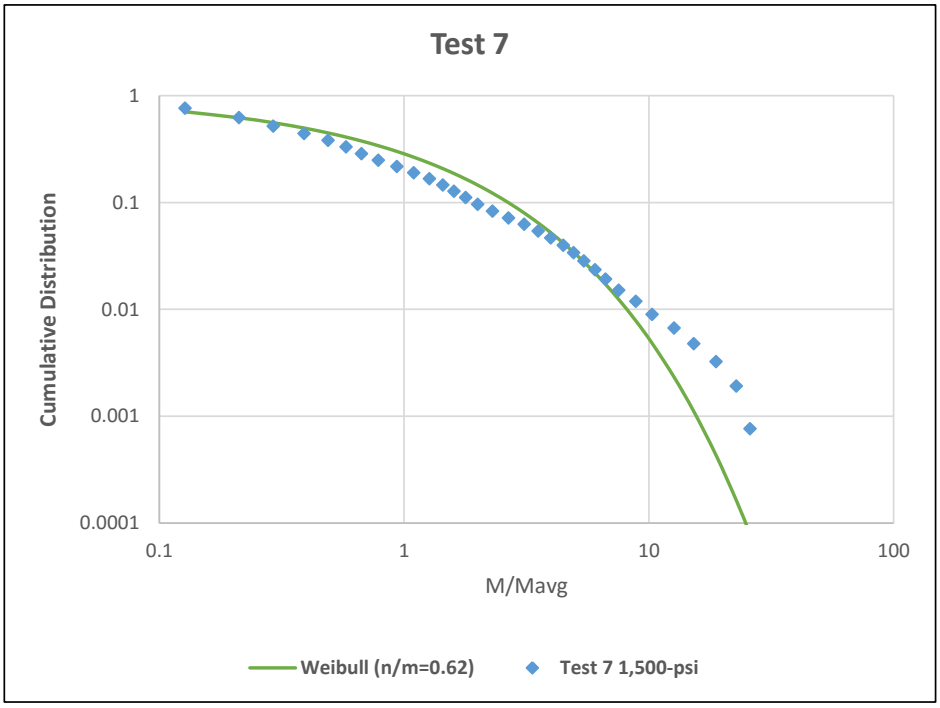

Figure 77. Best-fit Weibull mass distribution for physically-collected test data for PDF (top) and CDF (bottom) for Test 7 involving CMU.

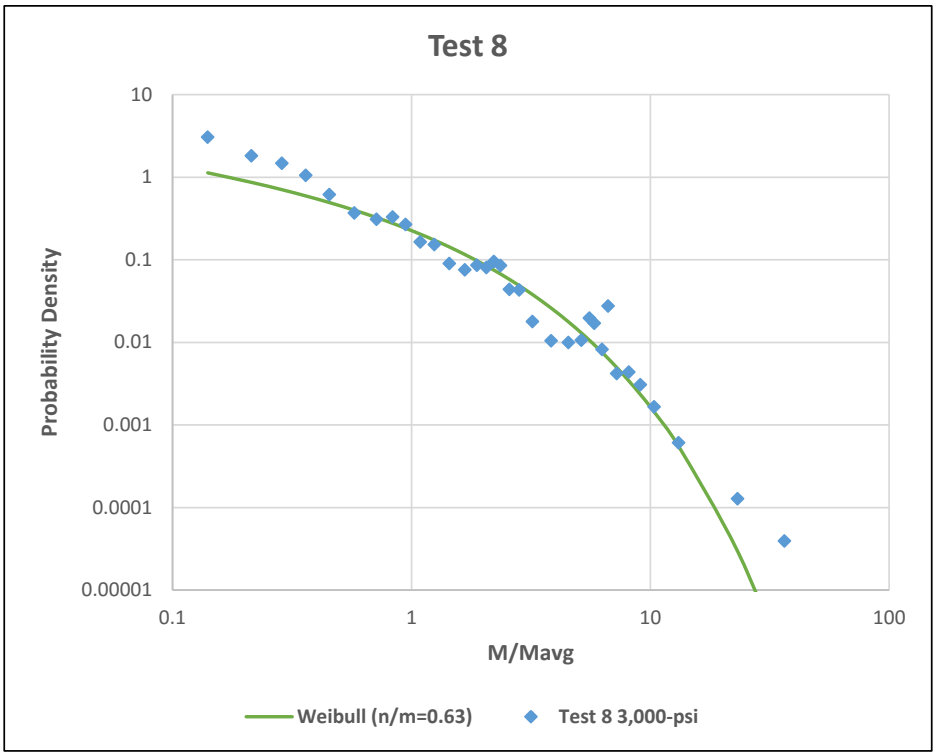

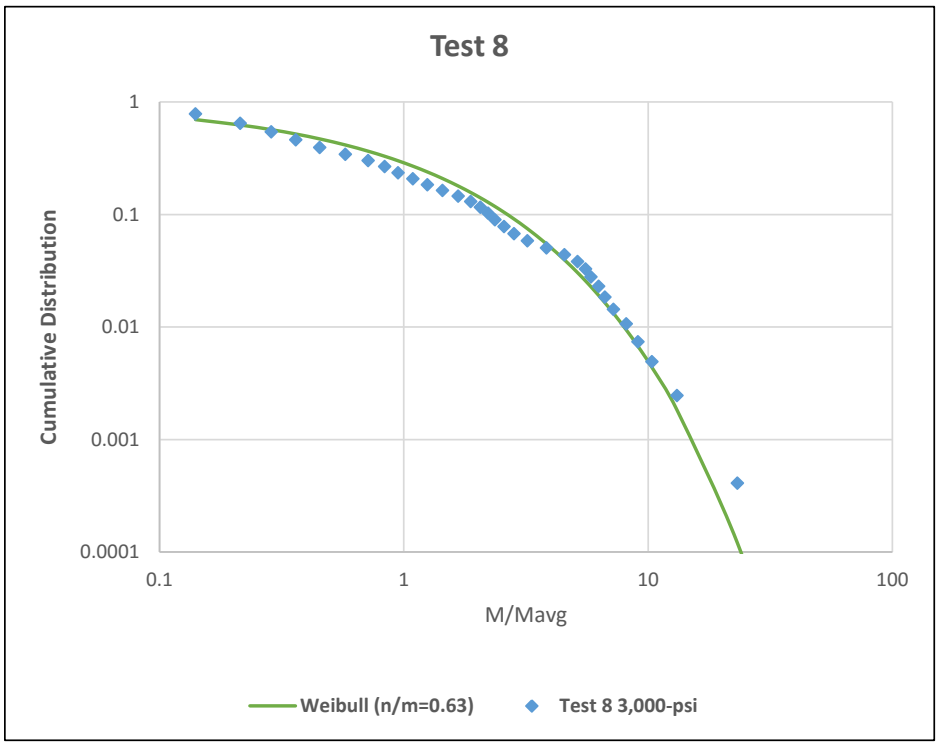

Figure 78. Best-fit Weibull mass distribution for physically-collected test data for PDF (top) and CDF (bottom) for Test 8 involving concrete.

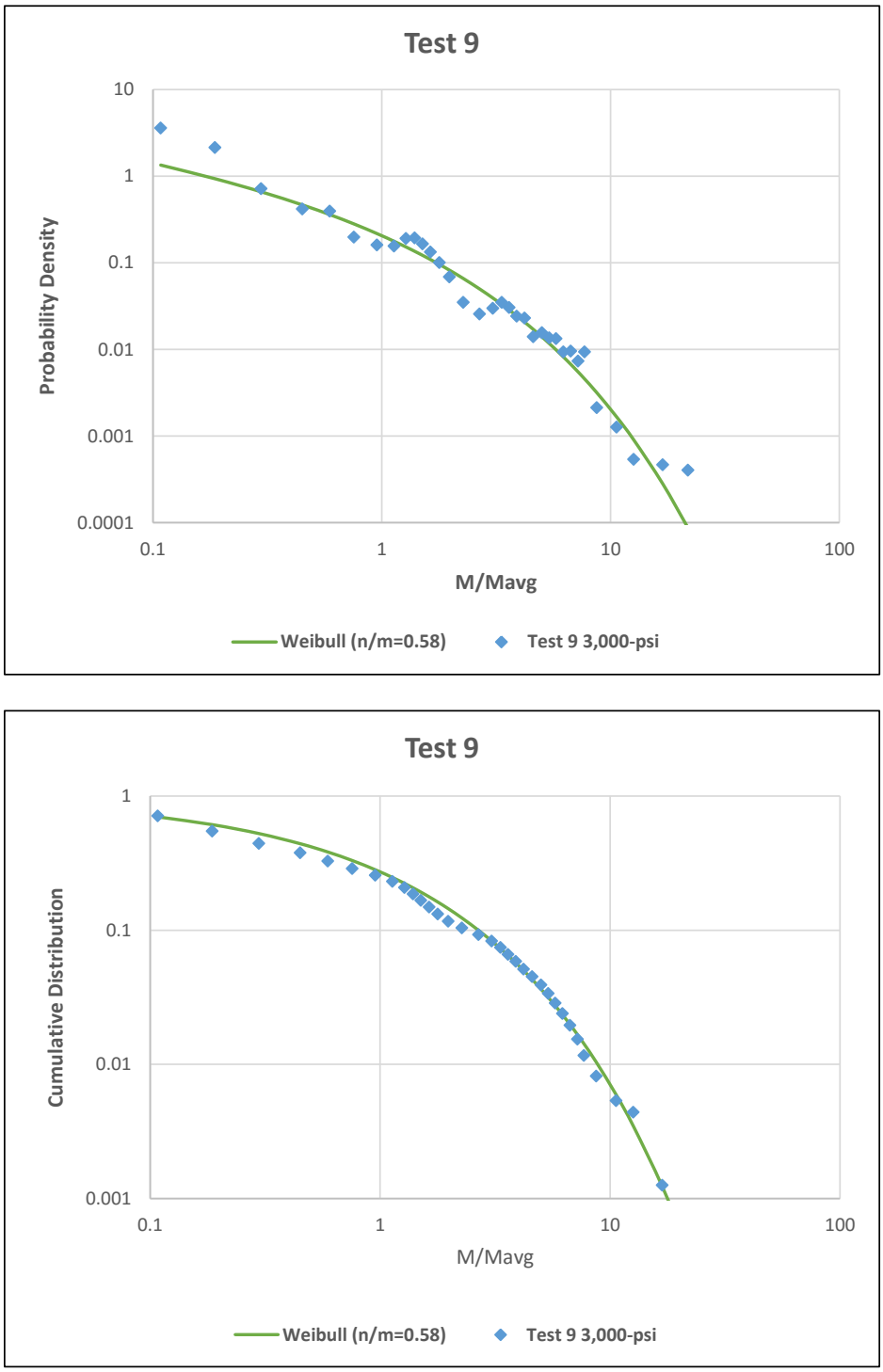

Figure 79. Best-fit Weibull mass distribution for physically-collected test data for PDF (top) and CDF (bottom) for Test 9 involving concrete.

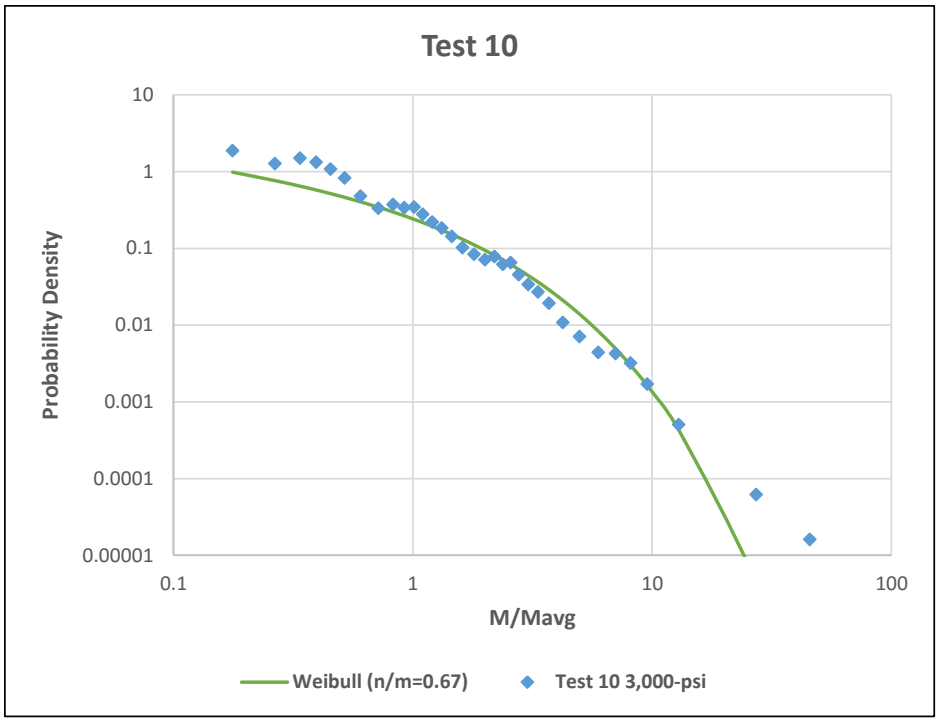

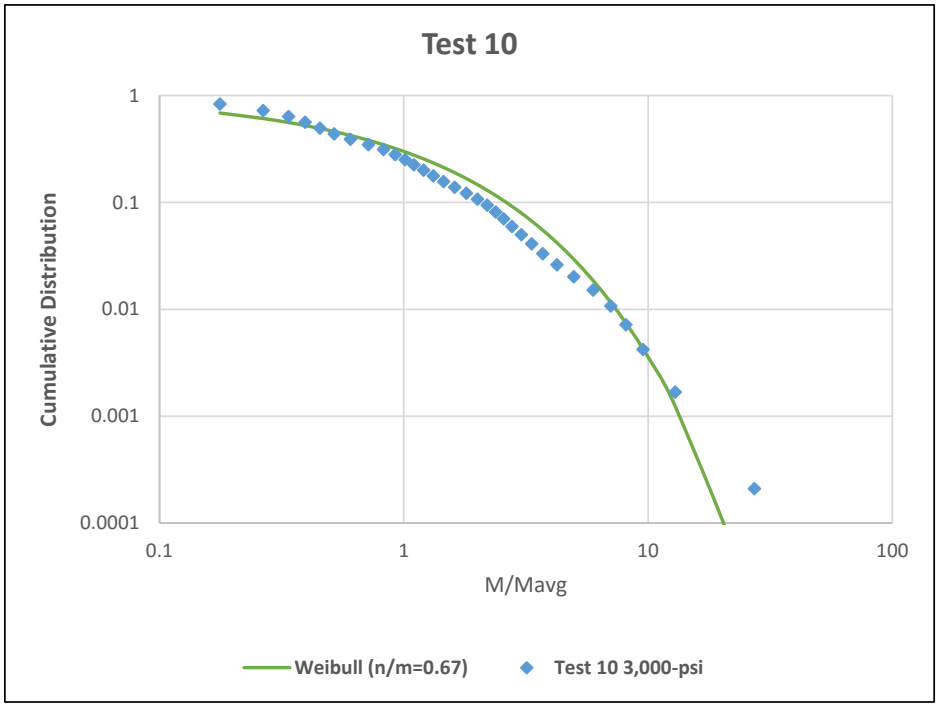

Figure 80. Best-fit Weibull mass distribution for physically-collected test data for PDF (top) and CDF (bottom) for Test 10 involving CMU.

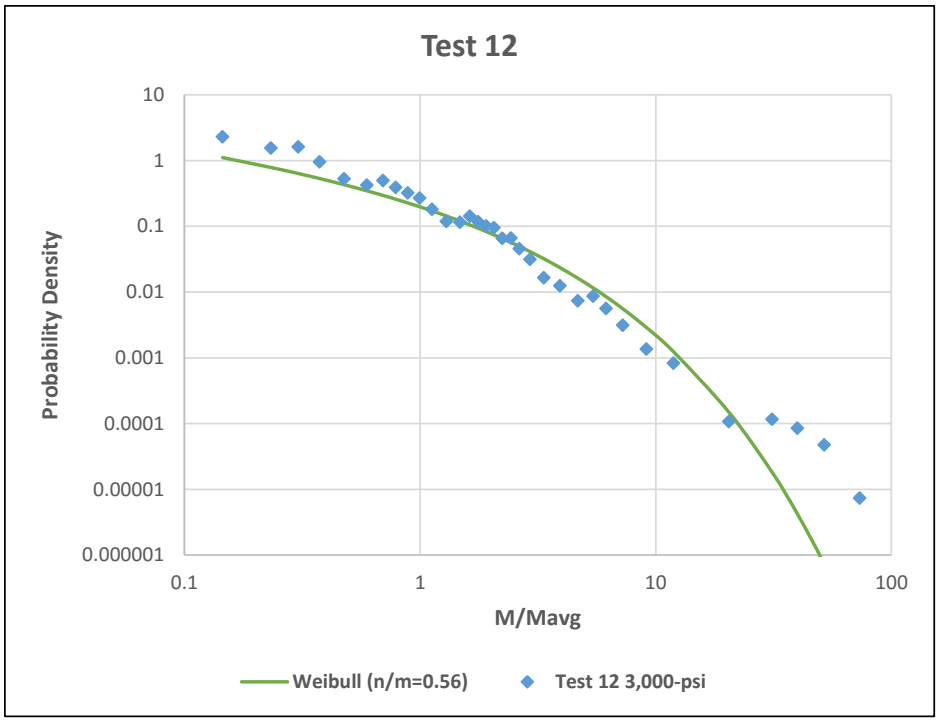

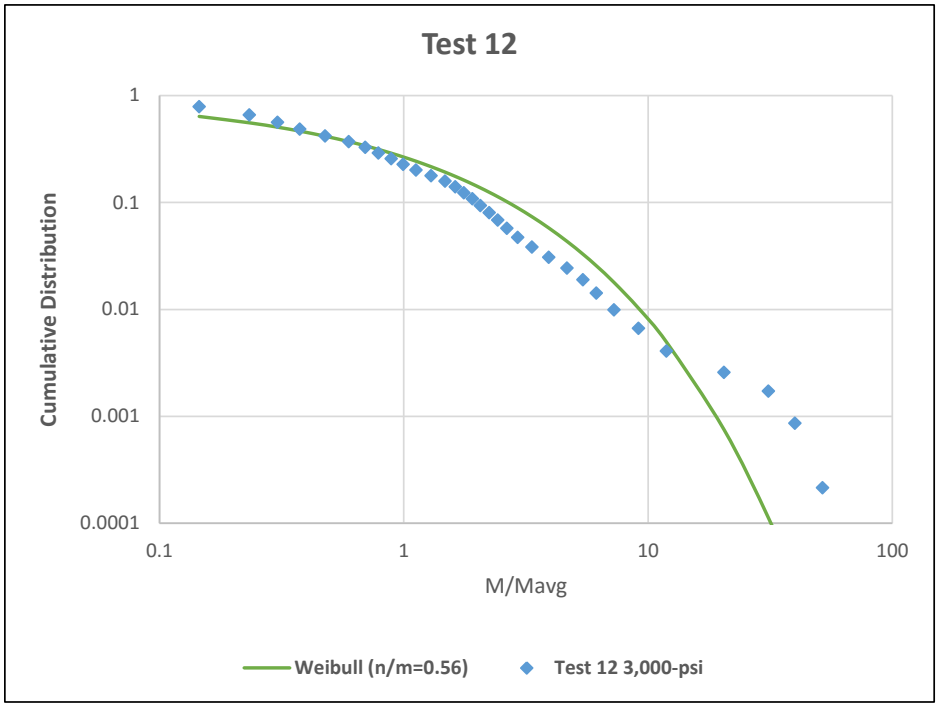

Figure 81. Best-fit Weibull mass distribution for physically-collected test data for PDF (top) and CDF (bottom) for Test 12 involving CMU.

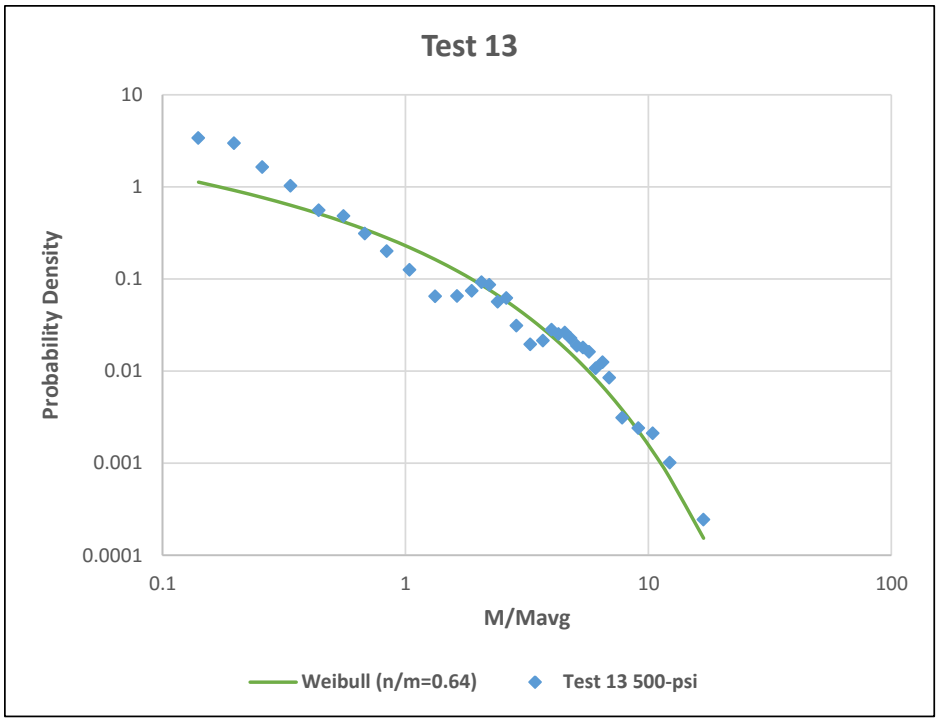

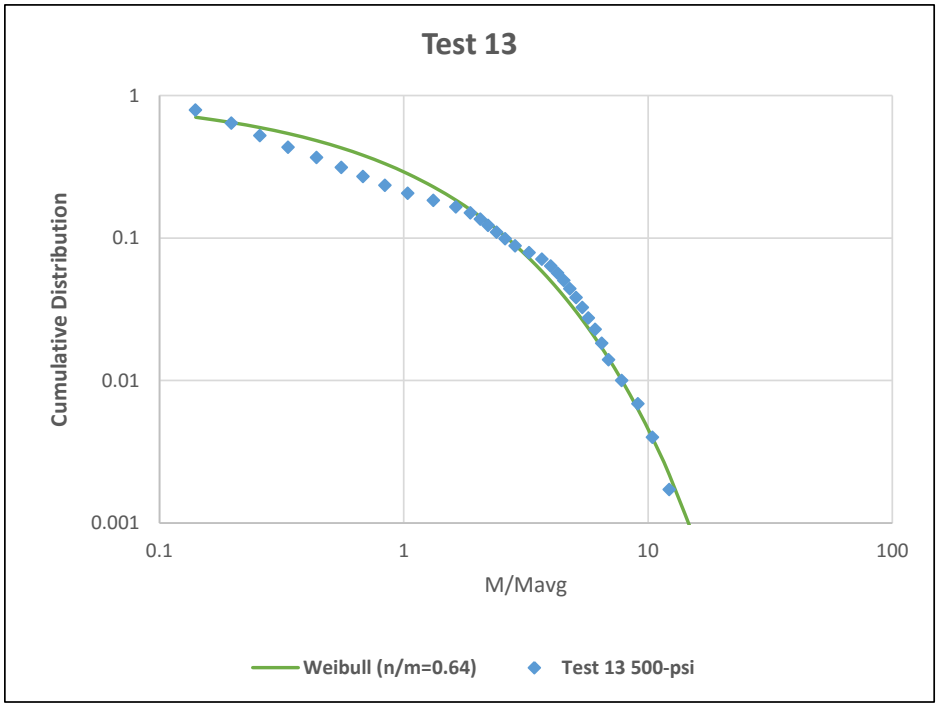

Figure 82. Best-fit Weibull mass distribution for physically-collected test data for PDF (top) and CDF (bottom) for Test 13 involving tempered glass.

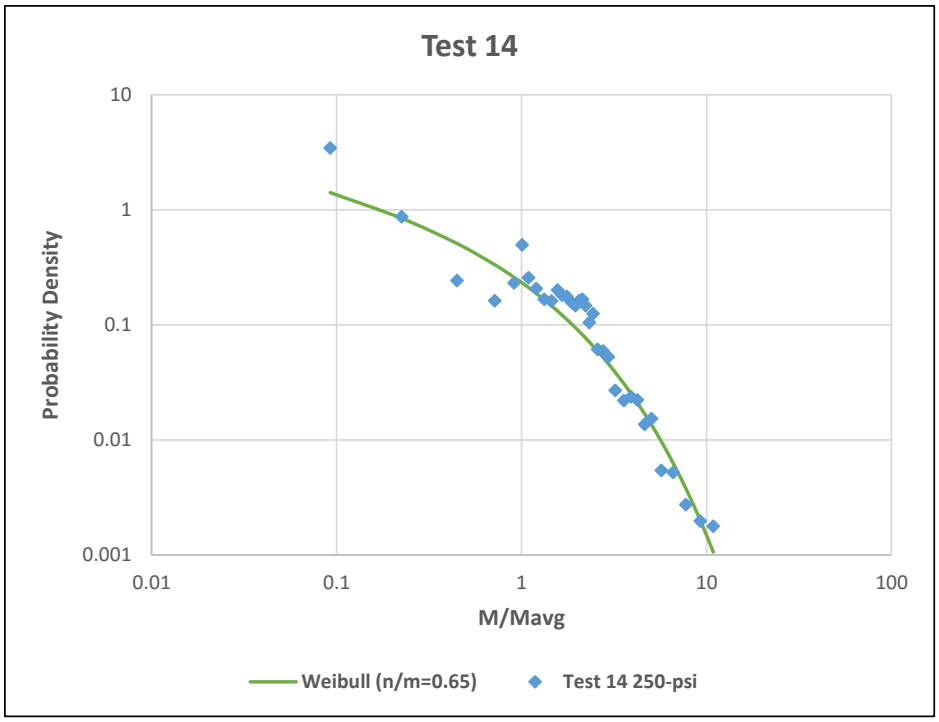

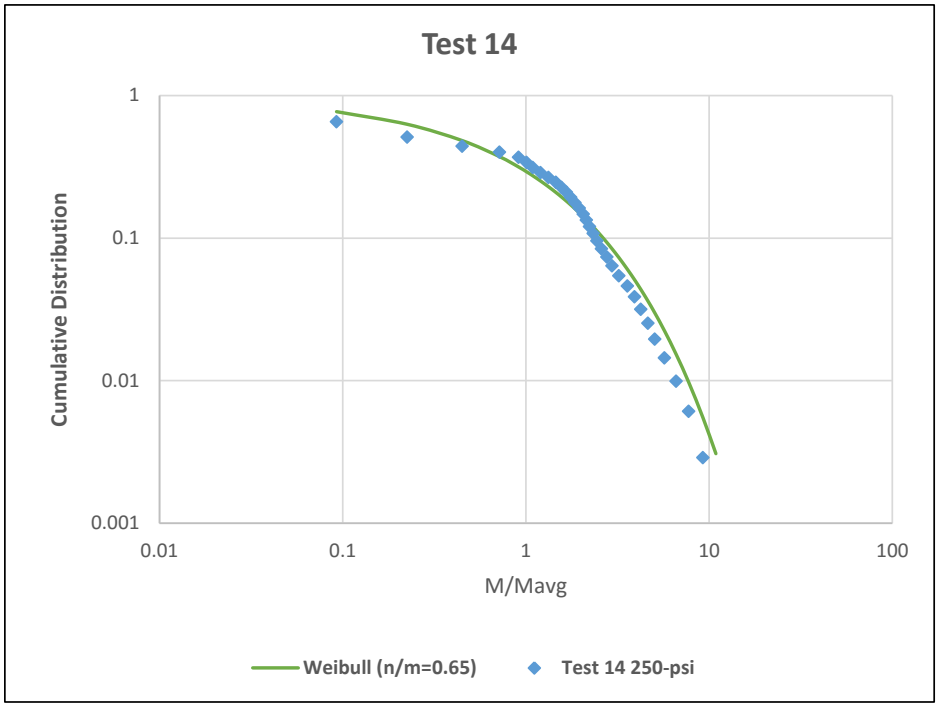

Figure 83. Best-fit Weibull mass distribution for physically-collected test data for PDF (top) and CDF (bottom) for Test 14 involving tempered glass.

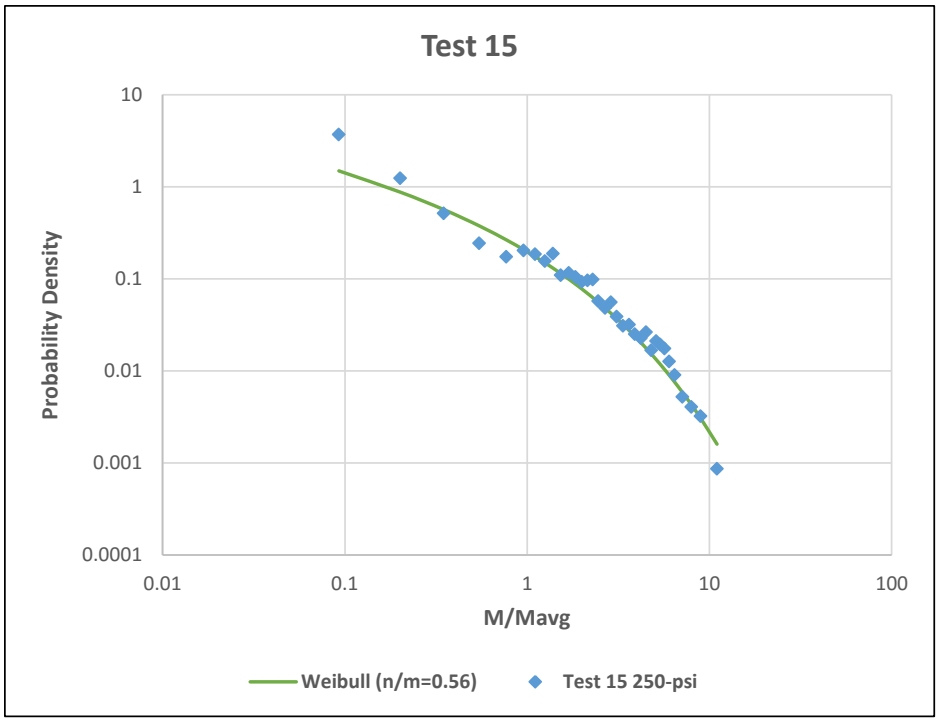

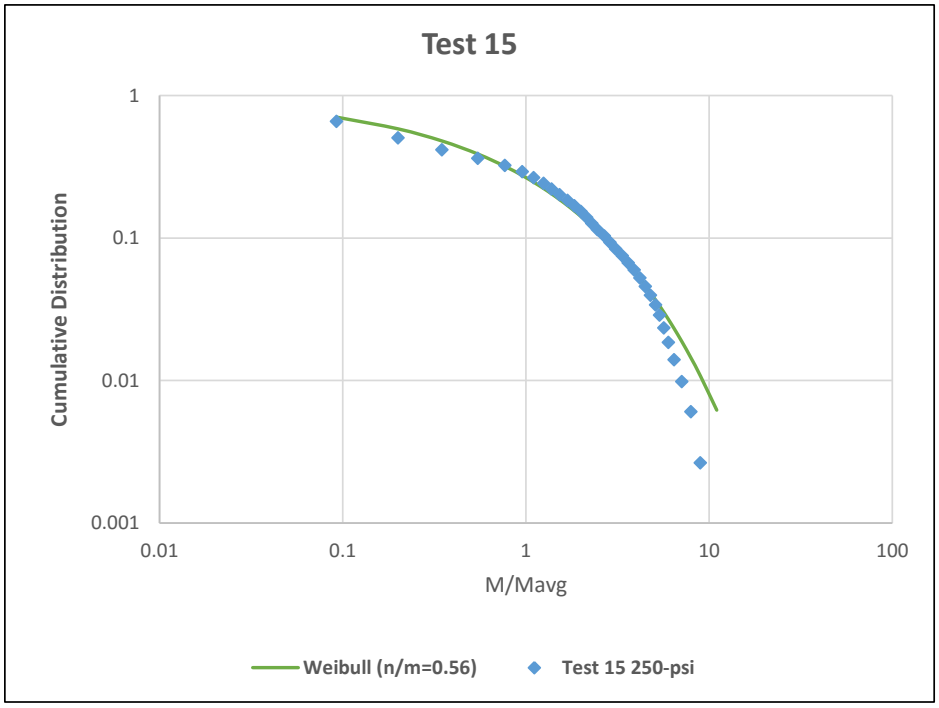

Figure 84. Best-fit Weibull mass distribution for physically-collected test data for PDF (top) and CDF (bottom) for Test 15 involving tempered glass.

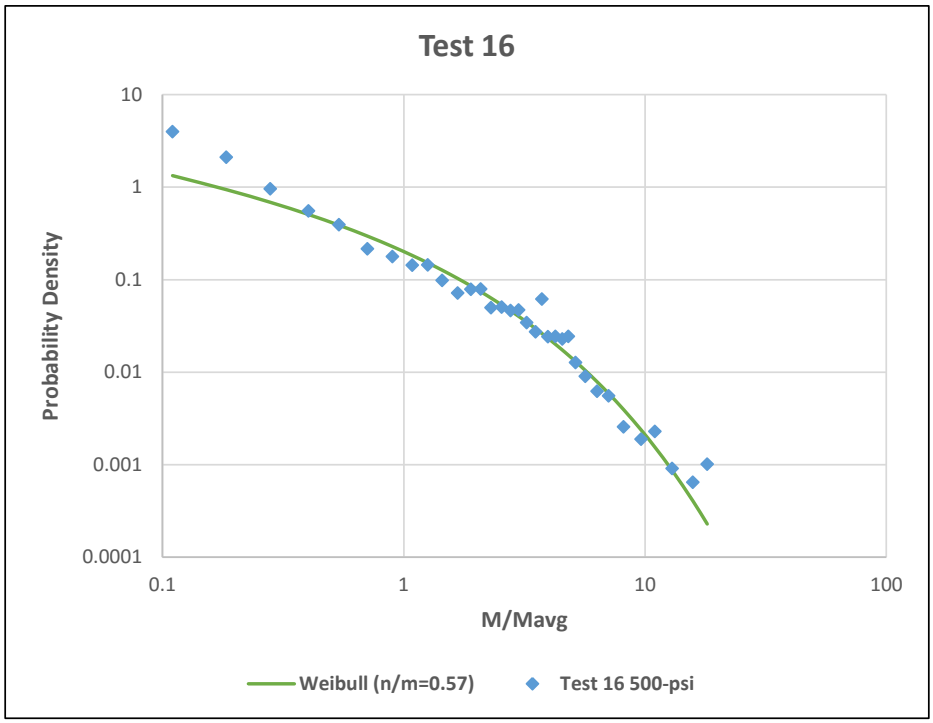

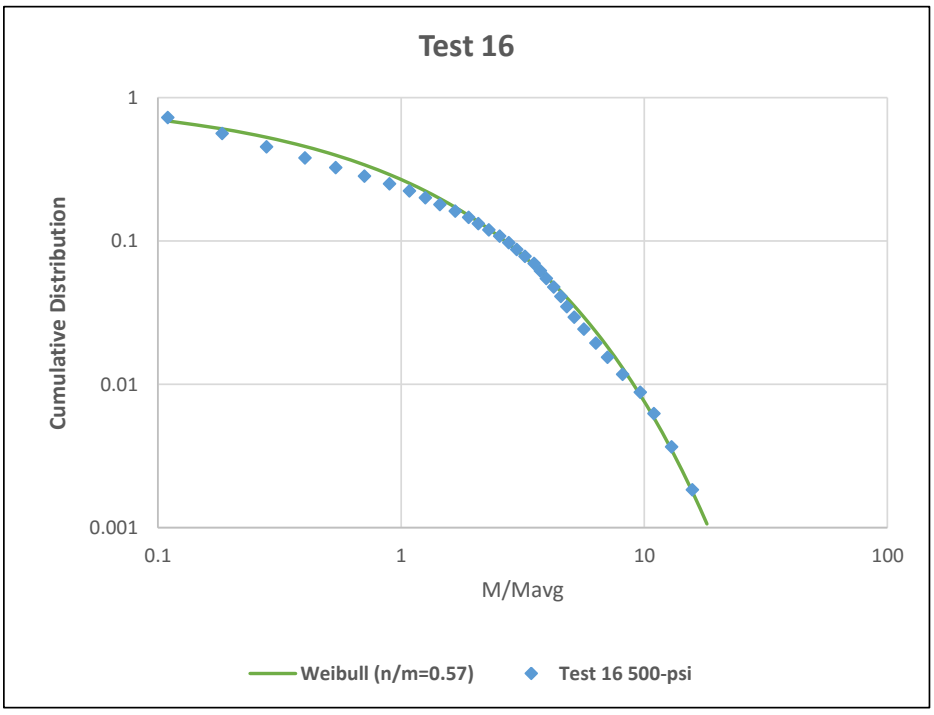

Figure 85. Best-fit Weibull mass distribution for physically-collected test data for PDF (top) and CDF (bottom) for Test 16 involving tempered glass.

As noted earlier, this effort attempted a number of other fits besides Weibull size distributions. For example, Bewick et. al. [11] fitted the physically collected mass data using so-called "modified Gamma" distributions; see also Laney [9]. For another example, Figure 86

shows the best-fit power law for physically-collected mass in the four tempered glass tests. The fit is a power law with $r \approx -2/3$. As noted in Section 4.1.2, this is approximately equal to a Weibull size distribution with $r = -2/3$, at least for fragments significantly larger than the count mean mass. The lesson learned here is that it can be hard to distinguish between Weibull size distributions with $r = +2/3$ and $r = -2/3$, depending on the range, and how the data is viewed.

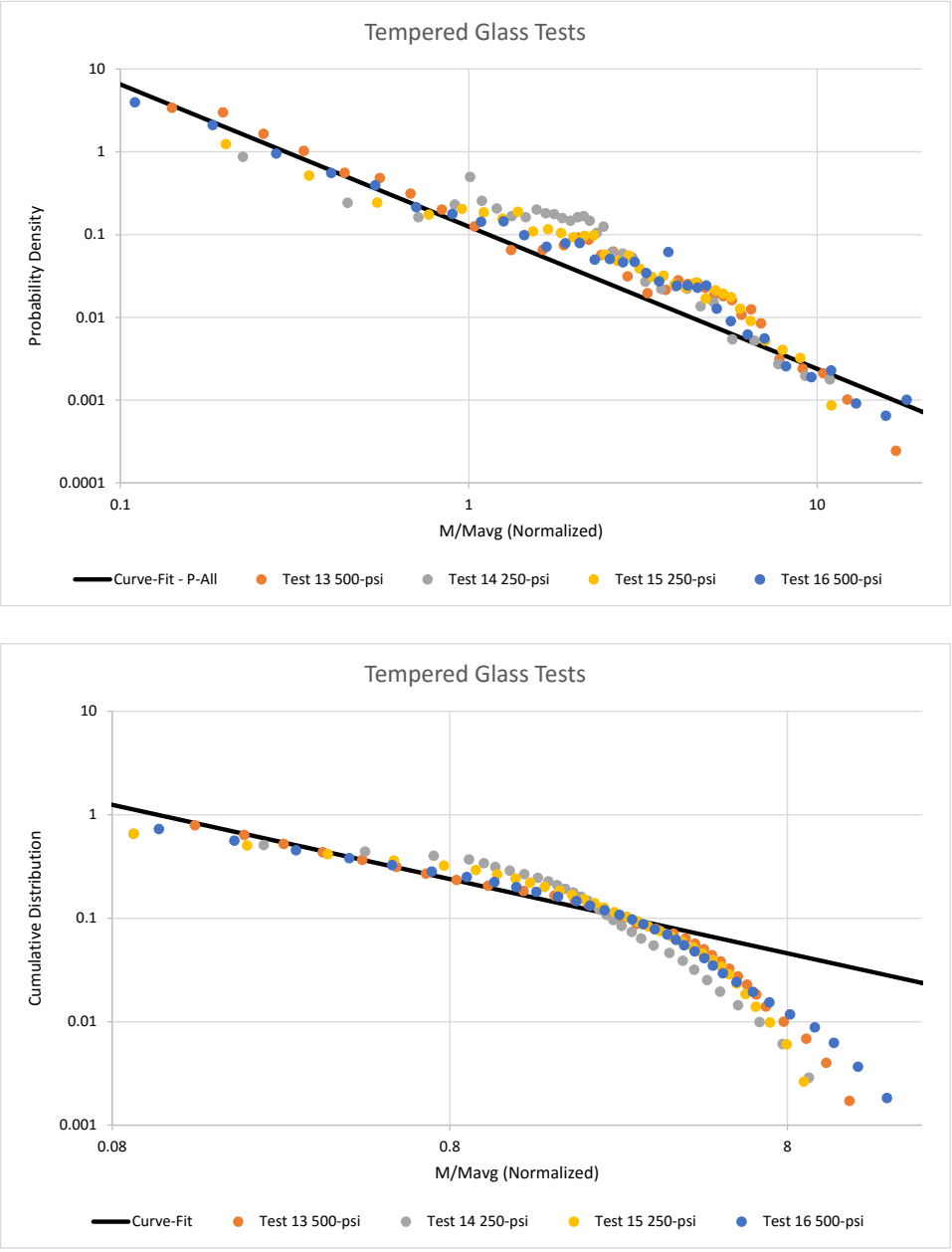

Figure 86. Best-fit power law mass distribution for physically-collected test data for PDF (top) and CDF (bottom) for Tests 13-16 involving tempered glass.

This effort considered piecewise combinations of two Weibull and/or power law size distributions, one for the smaller fragments and one for the larger fragments. In theory, this could help account for dimensional transitions, e.g., the smallest plate glass fragments form in three-dimensions and are rough on all sides, while the largest plate glass fragments form in two-dimensions and thus retain one or two smooths sides from the original sample. However, none of the piecewise combinations considered offered better accuracy than single Weibull size distributions.

5 CONCLUSIONS

Tests were performed in a small-diameter explosively-driven shock tube, which was used to shatter simply-supported plate samples with relatively high-pressure, long-duration blast loads. The plates were constructed from conventional façade construction materials including CMU material, tempered glass, and concrete.

High speed video (HSV) cameras were used to capture the early-time and mid-time fragments. In addition, physical collection was used to capture the late-time fragments. For the benefit of the mid-time side-view HSV, fragments were mechanically filtered with a stripper plate. Even though the stripper plate deflected a large number off-axis fragments, over 50,000 fragments were still physically collected across all 13 shots in this test series. It was not possible to weigh such a large number of fragments by hand. Instead, a new technique was developed, which combines sieving, shadowgraphy, and digital image processing techniques.

The experimental mass histograms were well-fitted by Weibull size distributions. One parameter in the Weibull size distribution, the average fragment size, appears to decrease between early- and late-times, at least for glass. This is probably due to a combination of mid-air collisions between fragments and collisions with the soft-catch collector. However, the other parameter, the Weibull exponent r, appears to stay the same, after a brief fragment formation period lasting less than 1ms. In fact, the same Weibull exponent $r = 2/3$ appeared to apply regardless of experimental conditions such as peak static overpressure and sample material. As described by Laney [8], this universal size distribution can be derived by combining entropy theory with geometric constraints.

As noted in Section 4.1.5, it can be hard to distinguish between Weibull size distributions with $r = 2/3$ and $r = -2/3$, depending on the range of the data and how it is viewed. The Weibull exponent $r = 2/3$ is commonly observed, e.g., [12]. However, the Weibull exponent $r = -2/3$ is even more commonly observed. For example, Piotrowski [13], Hellyer [14], and Ben-Naim & Krapivsky [15] give theoretical derivations for $r = -2/3$ for dynamic systems of objects – such as large numbers of colliding fragments – while Gilvarry [16], Inaoka & Takayasu [17] and Aschwanden et. el. [18] give experimental and computational evidence for $r = -2/3$ for a single fragmenting object.

Comparing the three measurement techniques used in this test series, the late-time physically-collected mass measurements clearly offered the best results. The early-time rear-view HSV offered adequate results, albeit only for 3 of the 13 tests, and then only over a limited size range and with some ambiguity due to finite fragment formation times. The mid-time side-view HSV offered poor results, partly due to a highly-restricted size range and random noise caused by smoke obscuration and limited video resolution, but still obtained Weibull size distributions with $r \approx 2/3$ on average, consistent with the early- and late-time measurements.

6 REFERENCES

[1] E. Williams, S. Akers and P. Reed, "Laboratory Characterization of SAM-35 Concrete," Us Army Corps of Engineers, Engineer Research and Development Center, Vicksburg, MS, September 2006.

[2] Pacific Supply, [Online]. Available: http://pacificsupply.paccoast.com/index.html. [Accessed 15 October 2015].

[3] CR Laurence, [Online]. Available: http://www.crlaurence.com/apps/contentloader/default.aspx?content=www.crlaurence.com/adv/glass_and_glazing/index_us.html. [Accessed October 15 2015].

[4] Jim's Glass Shop, [Online]. Available: http://www.jimsglass.biz/. [Accessed October 2015].

[5] W. Beason and J. Morgan, "Glass Failure Prediction Model," *J. Struct. Eng.*, vol. 110, no. 2, pp. 197-212, 1984.

[6] S. Outal, D. Jeulin and J. Schleifer, "A New Method for Estimating the 3D Size-Distribution Curve of Fragmented Rocks out of 2D Images," *Image Analysis & Stereology*, vol. 27, pp. 97-105, 2008.

[7] D. E. Grady and M. E. Kipp, "Mechanisms of Dynamic Fragmentation: Factors Governing Fragment Size," *Mechanics of Materials,* vol. 4, pp. 311-320, 1985.

[8] C. B. Laney, "Effects of Mixtures on Liquid and Solid Fragment Size Distributions," DTRA-TR-16-52, May 2016.

[9] C. B. Laney, "Transformation and Self-Similarity Properties of Gamma and Weibull Fragment Size Distribution," DTRA-TR-16-6, December 2015.

[10] B. Bewick, M. Barsotti, K. Marchand, M. Sanai and A. Ziemba, "Fragmentation Due To Overloaded Construction Facades," in *Design and Analysis of Protective Structures: Proceedings of the 3rd International Conference on Protective Structures*, 2015.

[11] B. Bewick, G. Rolater, M. Sanai and A. Ziemba, "Debris Hazards Due to Overloaded Conventional Construction Facades," in *Proceedings of the 16th International Symposium for the Interaction of the Effects of Munitions with Structures (ISIEMS)*, 2015.

[12] C. B. Laney, "Relationships between Liquid Atomization and Solid Fragmentation," DTRA-TR-16-9, March 2016.

[13] S. I. Piotrowski, "The Collisions of Asteroids," *Acta Astronomica,* vol. A5, pp. 115-138, 1953.

[14] B. Hellyer, "The Fragmentation of the Asteroids," *Monthly Notices of the Royal Astronomical Society,* vol. 148, pp. 383-390, 1970.

[15] E. Ben-Naim and P. L. Krapivsky, "Fragmentation with a Steady Source," *Physics Letters A,* vol. 275, p. 48–53, 2000.

[16] J. J. Gilvarry, "Fracture of Brittle Solids. I. Distribution Function for Fragment Size in Single Fracture (Theoretical)," *Journal of Applied Physics,* vol. 32, no. 3, pp. 391-399, 1961.

[17] H. Inaoka and H. Takayasu, "Universal Fragment Size Distribution in a Numerical Model of Impact Fracture," *Physica A*, vol. 229, no. 1, pp. 5-25, 1996.

[18] M. J. Aschwanden, N. B. Crosby, M. Dimitropoulou, M. K. Georgoulis, S. Hergarten, J. McAteer, A. V. Milovanov, S. Mineshige, L. Morales, N. Nishizuka, G. Pruessner, R. Sanchez, A. S. Sharma, A. Strugarek and V. Uritsky, "25 Years of Self-Organized Criticality: Solar and Astrophysics," *Space Science Reviews,* vol. 198, no. 1, p. 47–166, 2016.

APPENDIX A: ML EXPERIMENT DEVELOPMENT MODELS

In preparation for the small diameter shock tube experiments that will be used to complete the ML experiments, simulations were performed to examine the boundary condition possibilities and the strain rates to be expected. The objective of the simulations was to study the strain rates that might be achieved in the ML experiments. A ¼ symmetry model of a 16" (406.4-mm) square plate with a 2" (5-cm) thickness corresponding to the concrete and CMU was modeled with a pressure applied to the interior surface of the plate. The load applied was varied from 100-psi (68.9-kPa) up to 72,000-psi (496-MPa), which was predicted to be the upper capacity of SRI's small diameter shock tube. The materials were modeled using the concrete damage model as reported in the accompanying Simulations Report to determine the extent of damage, expected velocities, and estimates of strain rate.

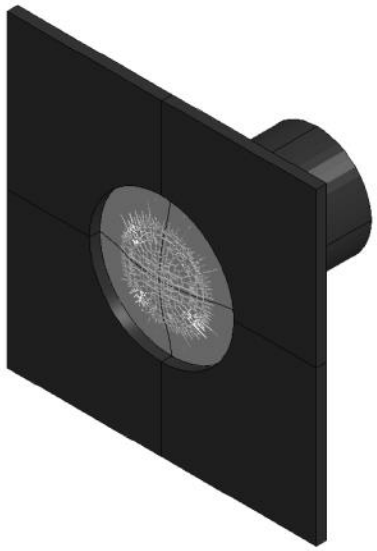

Figure 87. Visual of concrete sample LS-DYNA model.

The simulations were performed for concrete and tempered glass. Concrete was modeled as a 3,500-psi (27.6-MPa) compressive strength concrete. The tempered glass sample was modeled as a ¼" (6.3-mm) plate which is typical of tempered glass thicknesses. Figure 87 and Figure 88 show the simulation setup and an illustration of the progression of damage accumulated by a concrete sample under the shock tube loading. Figure 89 shows the results of the series of simulations. For each simulation, an in-plane velocity gradient was used to determine an average strain rate through the thickness of the plate. The velocity gradient was taken over a 2" radius at the rear face, middle of the sample, and at the front face of the sample. The results were tabulated and plotted. The results show that for ranges where the pressure is high enough to cause material level fragmentation, strain rates that range from 10^2 up to 10^4; two orders of magnitude.

Figure 88. Illustration of ML experiment model setup.

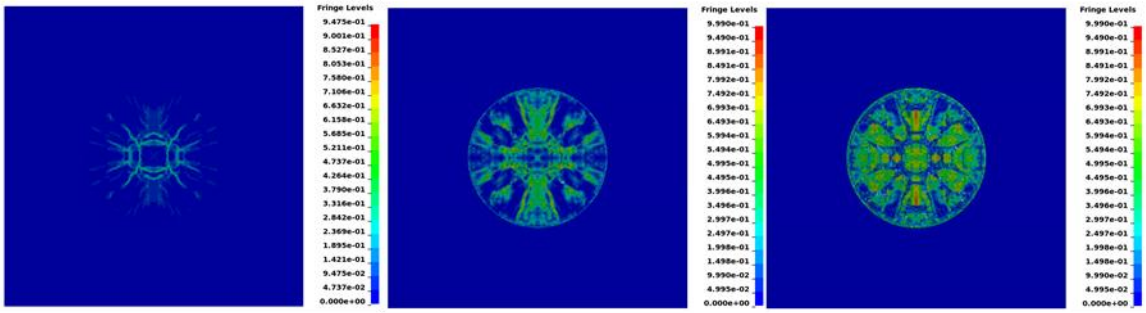

Figure 89. Progression of damage (1=fully damaged) on concrete sample setup for ML experiment sample.

APPENDIX B: CONCRETE AND CMU COMPRESSIVE STRENGTHS

BURNS COOLEY DENNIS, INC.

CONSTRUCTION MATERIALS AND ENGINEERING TESTING SERVICES

278 Commerce Park Drive
RIDGELAND, MS 39157

BUS: (601) 856-2332
FAX: (601) 856-3552

CONCRETE TEST REPORT

TO: Woodward Concrete Construction
101 Stonewall Road
Vicksburg, MS 39180

Earnest Woodward

Report Date: June 20,2014

BCD Project Number: 140352

Set Number: 39309

PROJECT: Protection Engineering Concrete Testing

FIELD TEST CONDITIONS AND RESULTS

		Field Test(s)	Specimens	Additional
Date Sampled:	5/23/2014	Time Sampled:	11:30 AM	
Supplier:	MMC, Inc.	Ticket Number:	4453071	
Mix Number:	V3370202	Water Added (gal.):	0	
Specified Strength (psi):	3,000	* Air Content (%)	4.1	
Specimen Type:	4-in. Diam. Cylinder	Concrete Temp. (° F):	79	
Concrete Quantity,(yd³):	4	Slump (in.):	2.25	
Initial Curing Temperatures, (°F)		Unit Weight (pcf):		
Mininum:		Technician:	C. B.	
Maximum:				

Location: Test Panels

Remarks:

COMPRESSION TEST RESULTS

Sample Number	Test Date	Age Days	Dim1 (in.)	Dim2 (in.)	Area (in.²)	Max Load (lbs)	Strength (psi)	% of Specified Strength	Type Fracture	Comments
1	05/30/2014	7	4.00	3.99	12.57	28,210	2,240	74	5	
2	05/30/2014	7	4.00	3.97	12.5	28,800	2,300	76	5	
3	06/20/2014	28	4.00	4.00	12.57	40,120	3,190	106	5	
4	06/20/2014	28	4.01	4.02	12.63	38,510	3,050	101	5	
5 Hold	06/20/2014	28	0.00	0.00	0		0	0		
6 Hold	06/20/2014	28	0.00	0.00	0		0	0		

Remarks: Tests conducted as required by the following ASTM Standards. ASTM C31, C39, C138, C143, C172, C173 or C231, C1064
* ASTM C231 was used to determine air content unless noted. Aggregate correction factor has not been applied to the air content shown, unless noted in "Remarks". Typical aggregate correction factor values range from 0.2 to 0.6, but must be determined based on mixture proportions and aggregate source.

Comments: We appreciate the opportunity to be of service. If you should have any questions concerning this report, please do not hesitate to call us.

REPORTED BY: _____
Concrete Materials Manager

REVIEWED BY: _____
Engineer

Wallace Kuhl & Associates

CORPORATE OFFICE
3050 Industrial Boulevard
West Sacramento, CA 95691
916.372.1434 phone
916.372.2565 fax

STOCKTON OFFICE
3422 West Hammer Lane, Suite D
Stockton, CA 95219
209.234.7722 phone
209.234.7727 fax

June 13, 2013

Mr. Lance Vasquez
Basalite Concrete Products
lance.vasquez@paccoast.com

Concrete Masonry Unit Laboratory Testing
ON-CALL MASONRY MATERIALS TESTING SERVICES
Dixon, California

As authorized, our firm has performed laboratory testing of 8x8x16 Open End Standard concrete masonry units (CMU) for the subject project to verify the compressive strength and material properties of the concrete block in accordance with ASTM C140-13. The CMU were tested over 28 days after manufacture.

SPECIMEN ID	Mix 725 – Normal Weight (cast 4-6-13)	AVG.
1. Absorption (PCF)	8.5	
	7.7	
	7.9	**8.0**
2. Density (PCF)	131.0	
	134.2	
	131.9	**132.4**
3. Compressive Strength (psi) (by Coupon)	4520	
	4460	
	4440	**4470**
4. Linear Shrinkage (%)	0.046	
	0.056	
	0.038	**0.047**

NOTE: The tested CMU comply with the absorption, density, compressive strength and shrinkage requirements of ASTM C90-12.

Please contact me if you have any questions or require further information.

Wallace – Kuhl & Associates (AASHTO accredited for ASTM E329)

REGISTERED PROFESSIONAL ENGINEER
DAVID A. REDFORD
NO. C 051122
Exp. 9/30/13
CIVIL
STATE OF CALIFORNIA

David A. Redford, P.E.
Senior Engineer

APPENDIX C: SMALL DIAMETER SHOCK TUBE EXPERIMENTS PRESSURE DATA

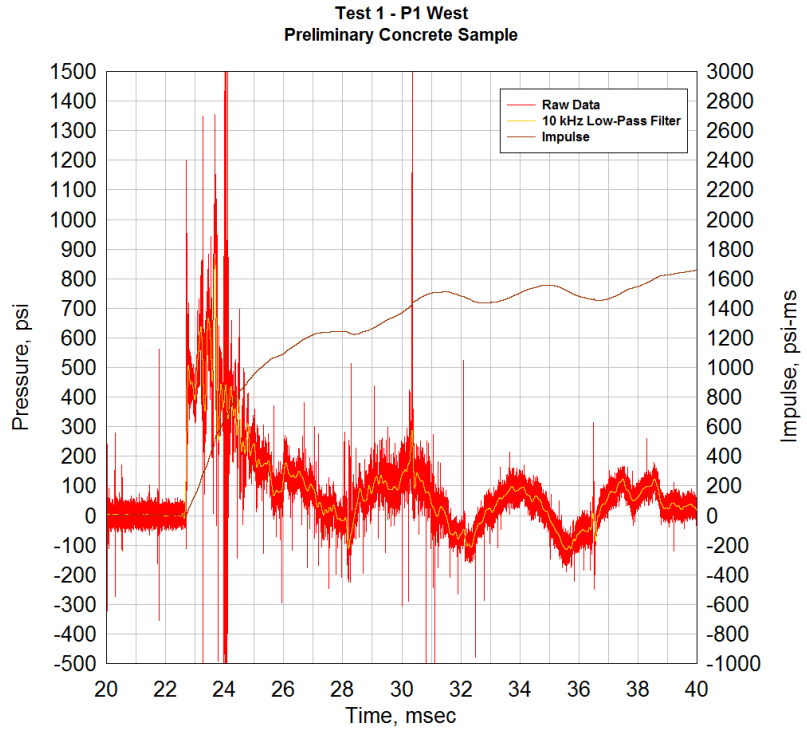

Figure 90. Test 1 P1 west pressure gage data.

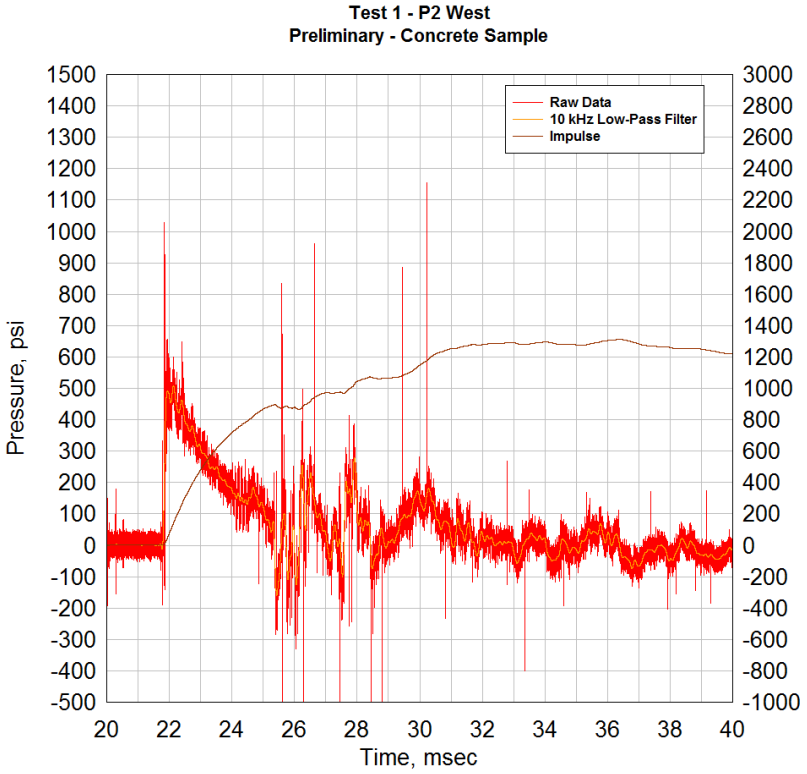

Figure 91. Test 1 P2 west pressure gage data.

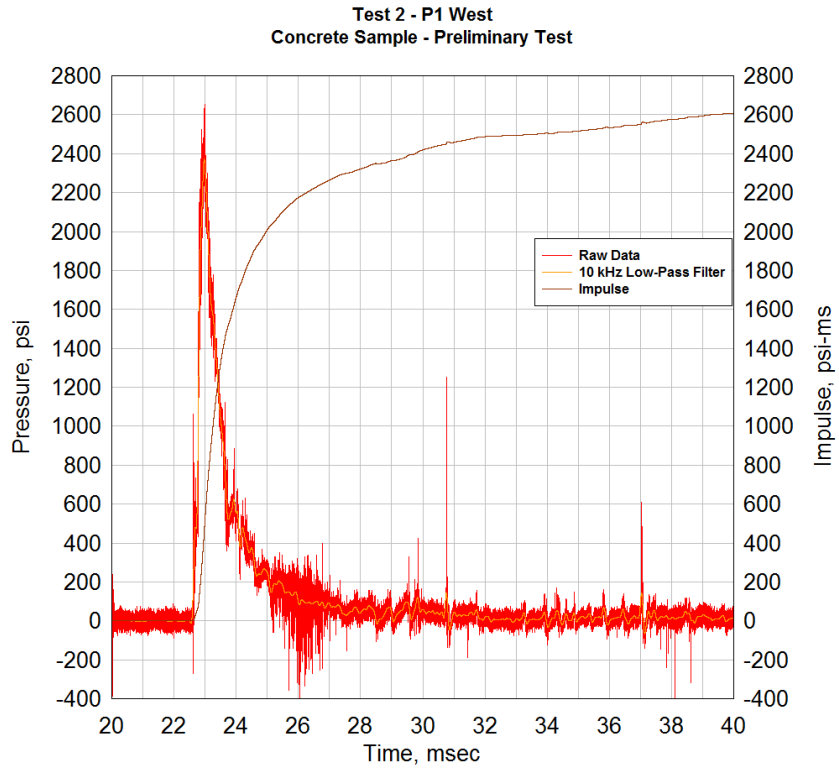

Figure 92. Test 2 P1 west pressure gage data.

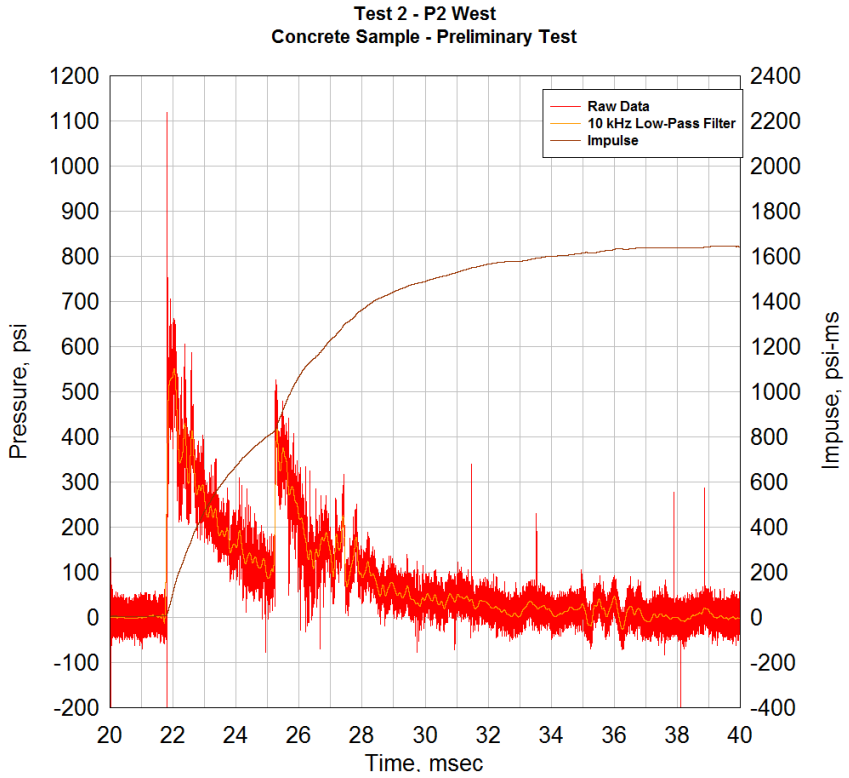

Figure 93. Test 2 P2 west pressure gage data.

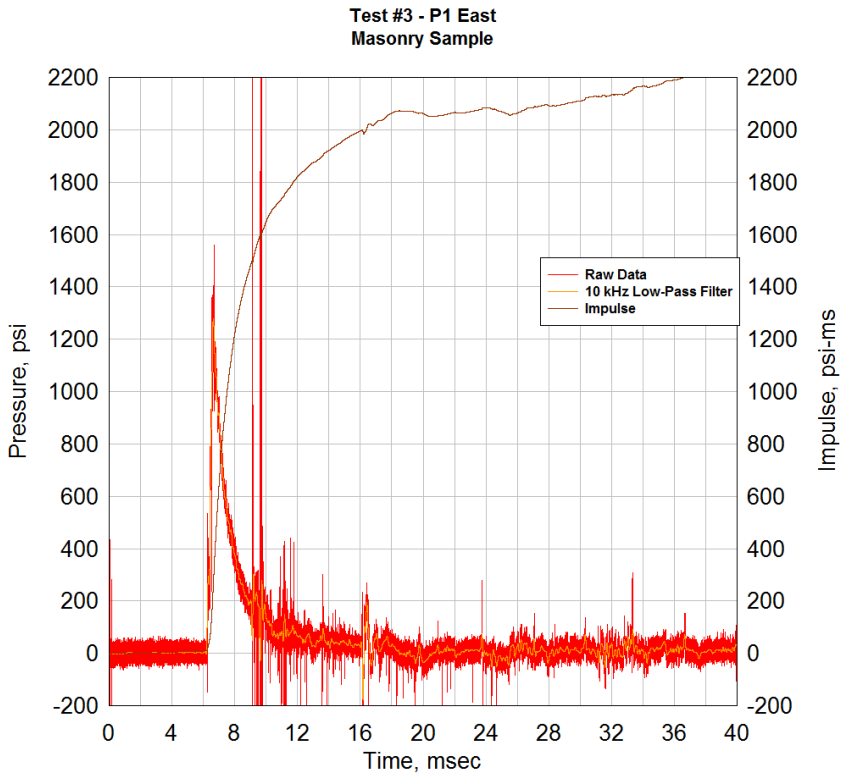

Figure 94. Test 3 P1 east pressure gage data.

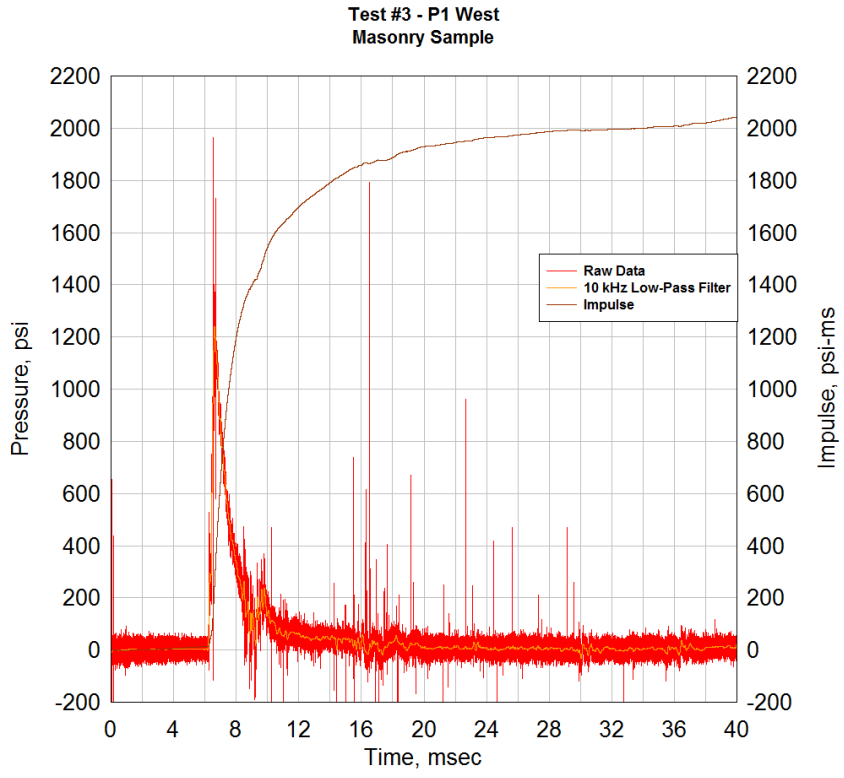

Figure 95. Test 3 P1 west pressure gage data.

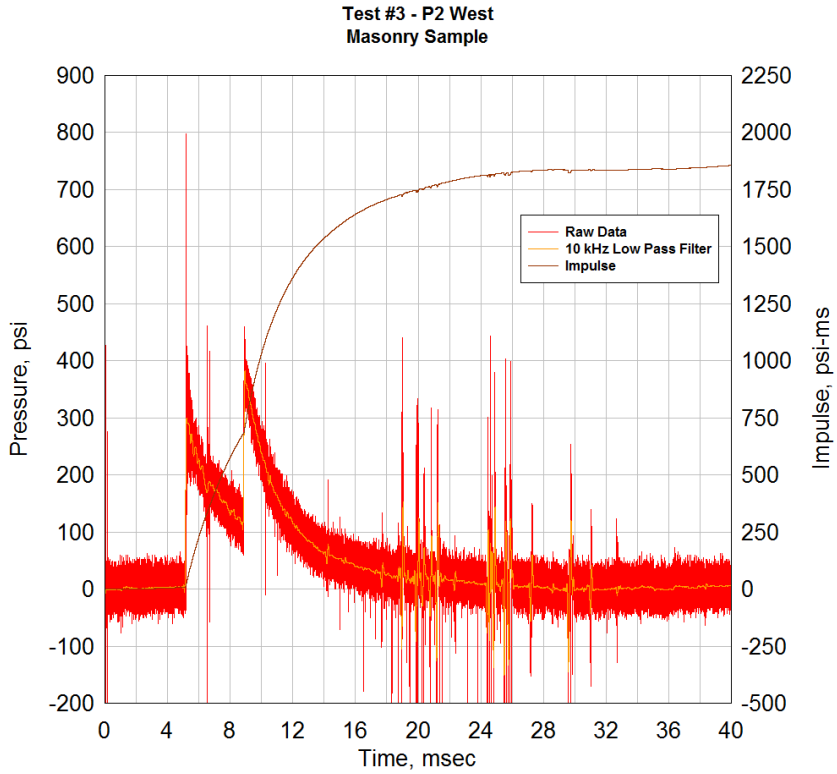

Figure 96. Test 3 P2 west pressure gage data.

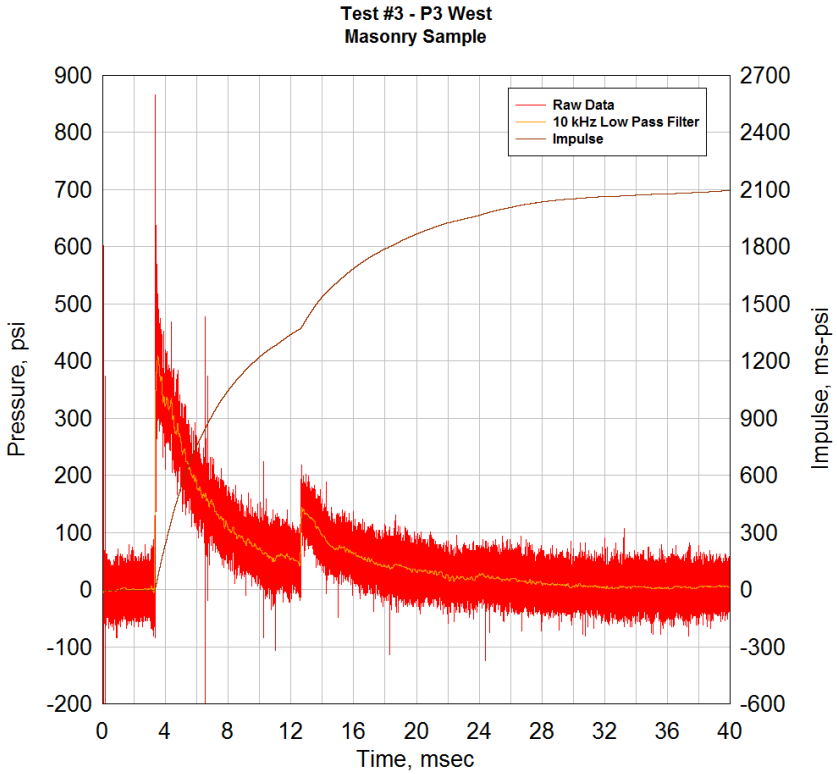

Figure 97. Test 3 P3 west pressure gage data.

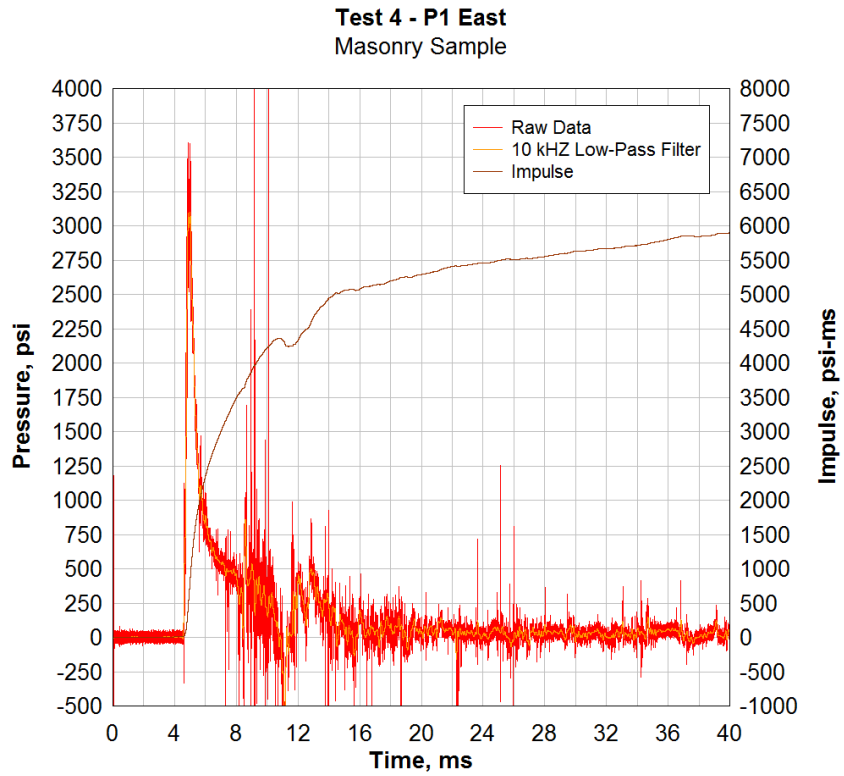

Figure 98. Test 4 P1 east pressure gage data.

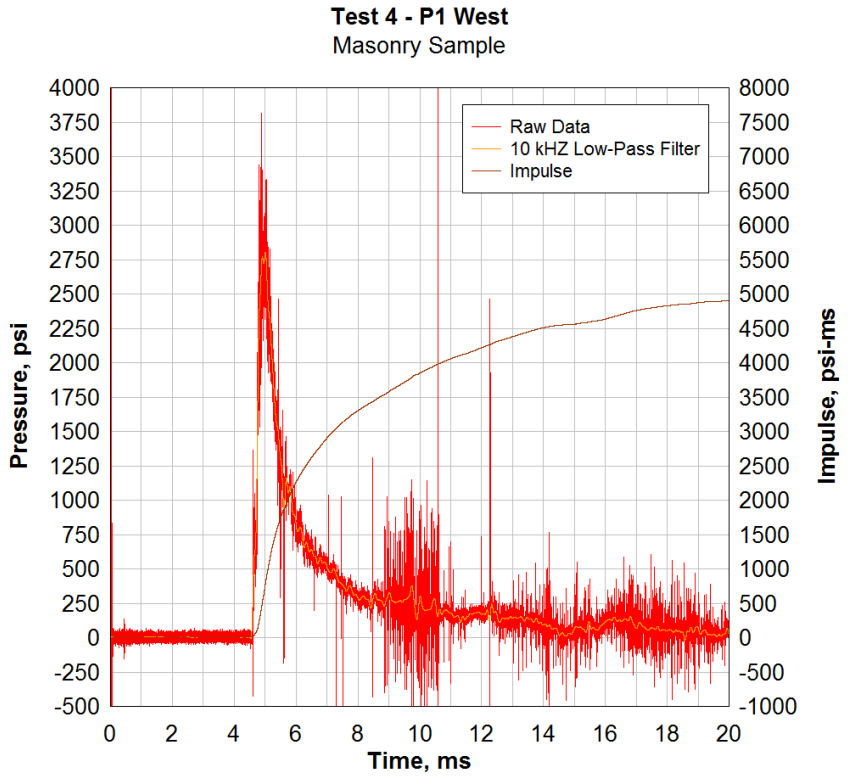

Figure 99. Test 4 P1 west pressure gage data.

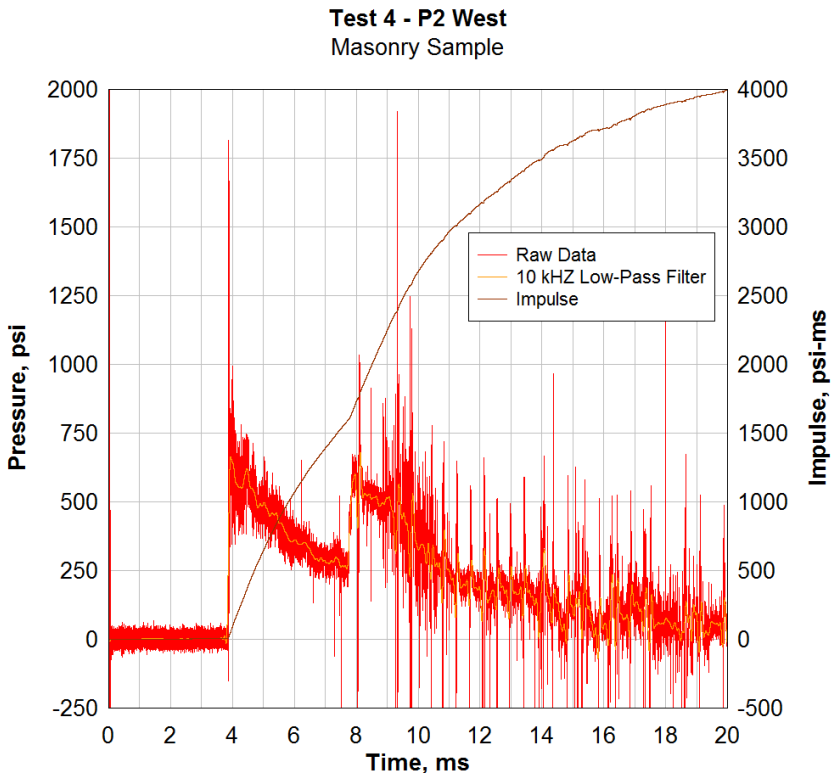

Figure 100. Test 4 P2 west pressure gage data.

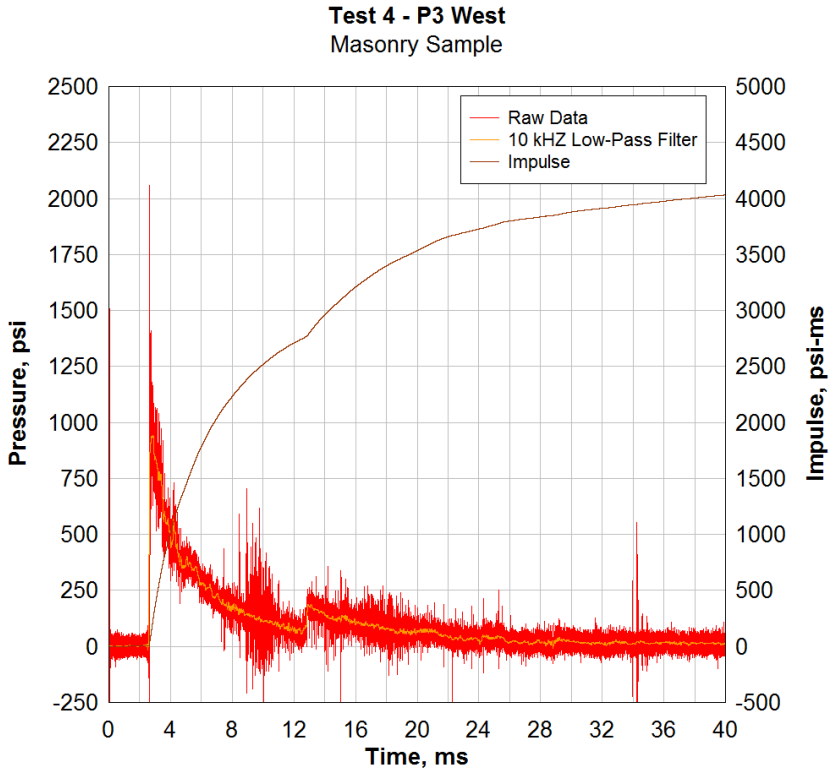

Figure 101. Test 4 P3 west pressure gage data.

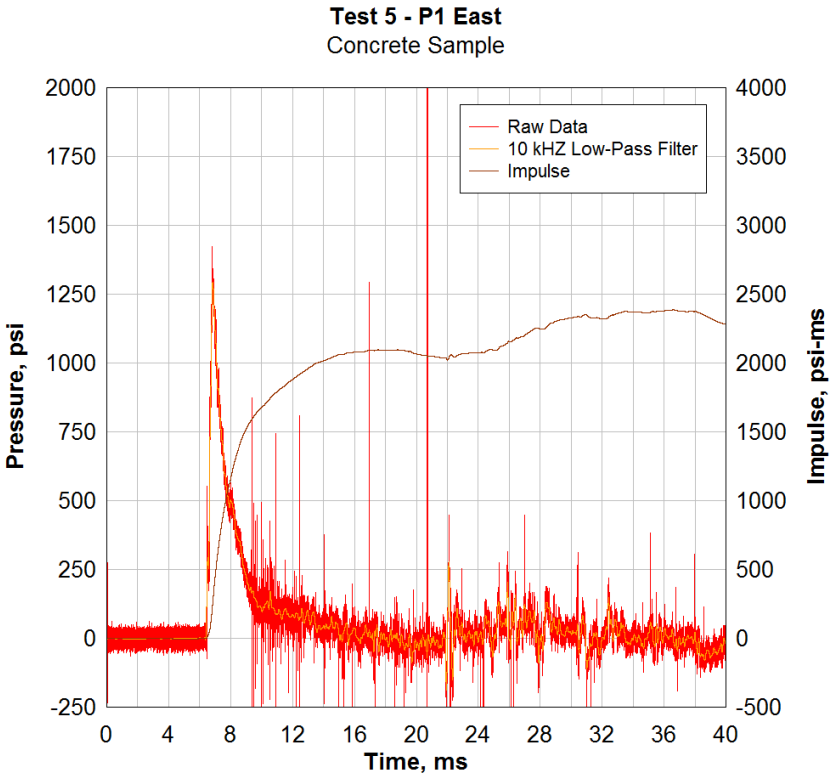

Figure 102. Test 5 P1 east pressure gage data.

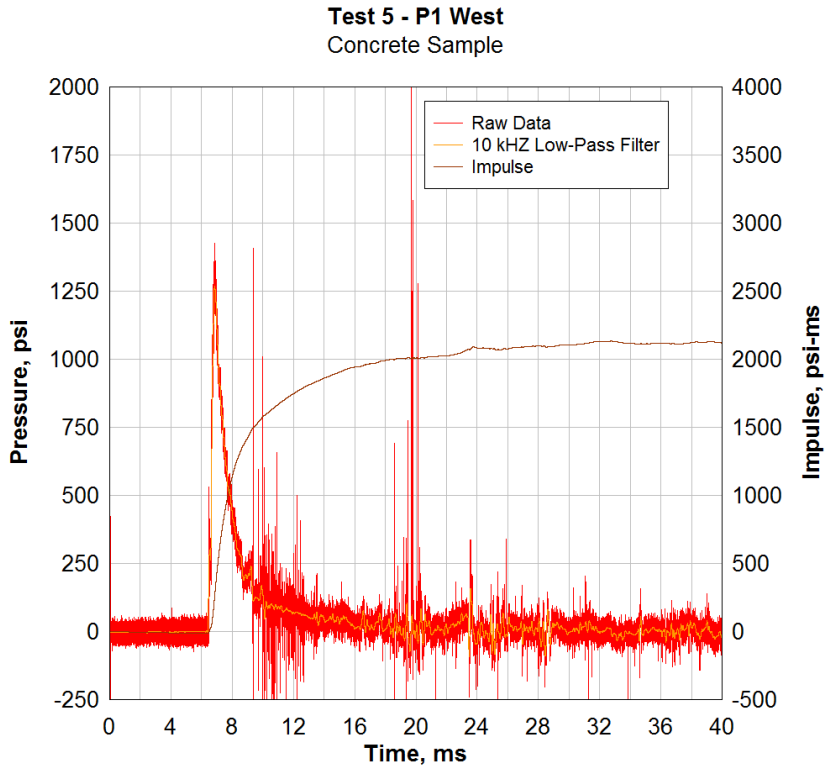

Figure 103. Test 5 P1 west pressure gage data.

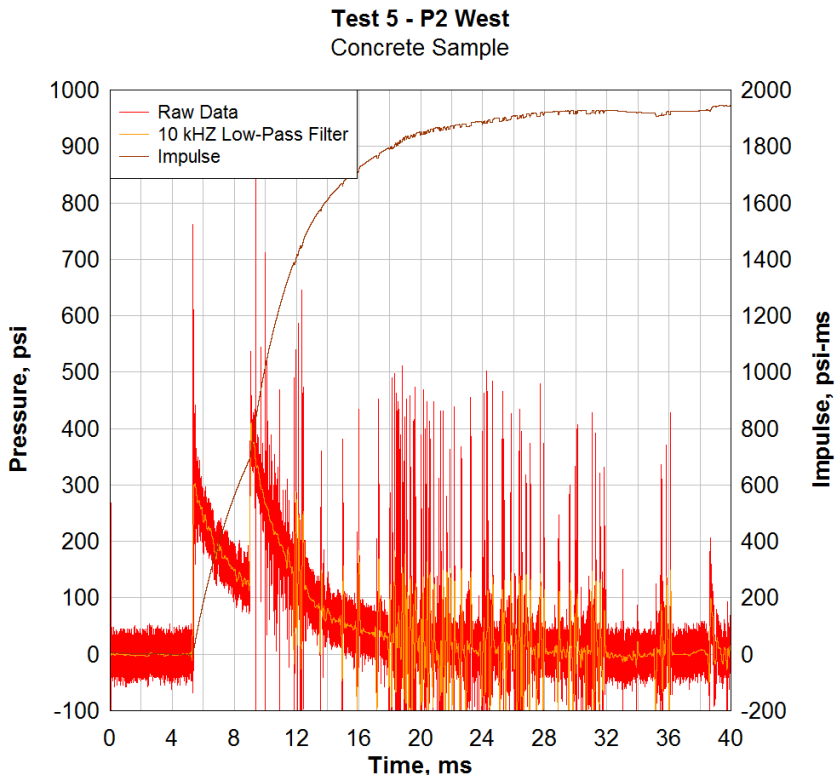

Figure 104. Test 5 P2 west pressure gage data.

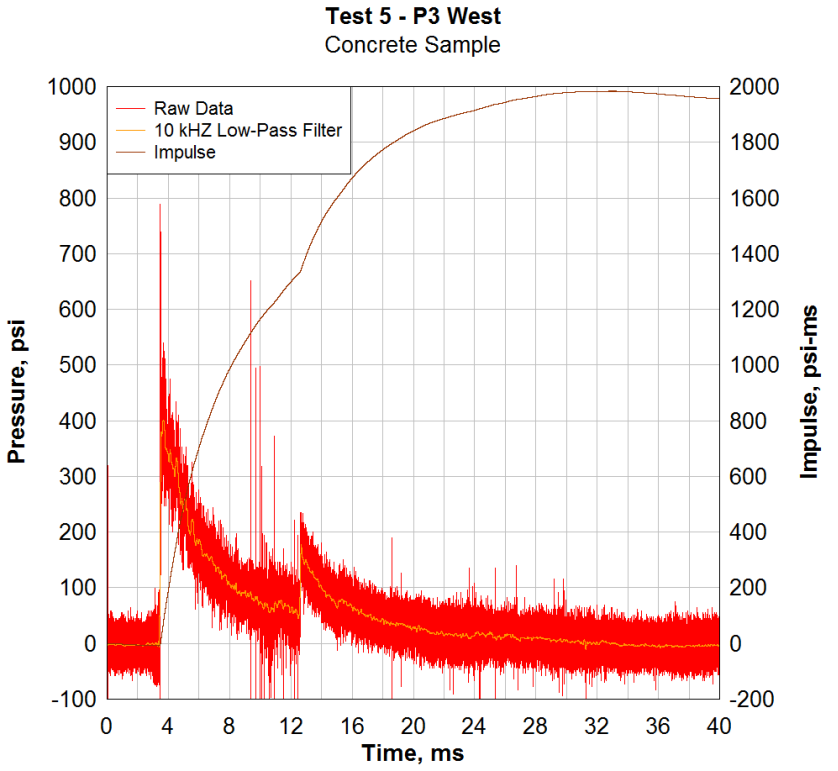

Figure 105. Test 5 P3 west pressure gage data.

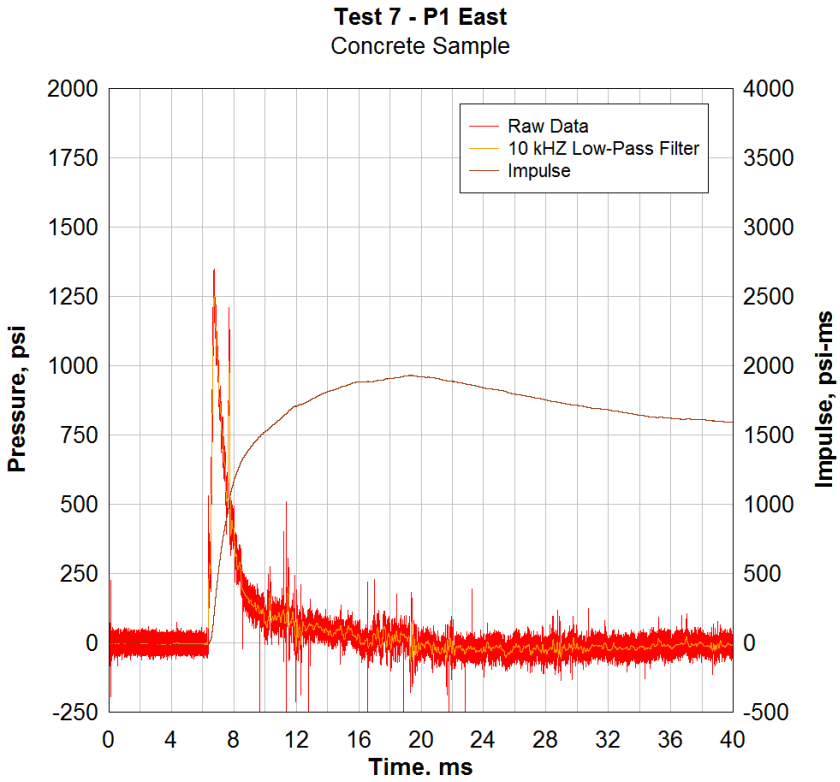

Figure 106. Test 7 P1 east pressure gage data.

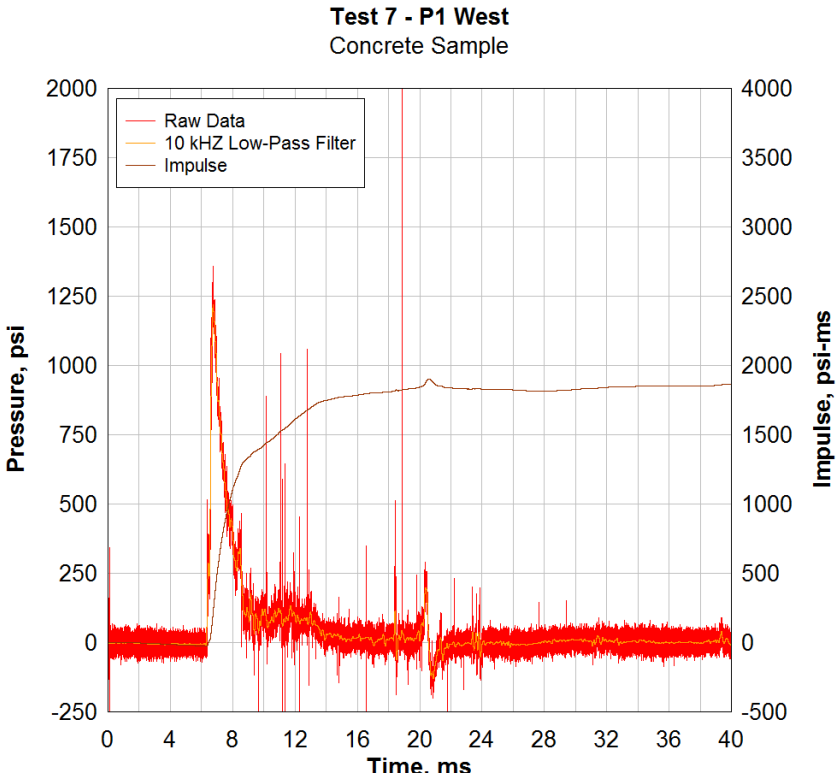

Figure 107. Test 7 P1 west pressure gage data.

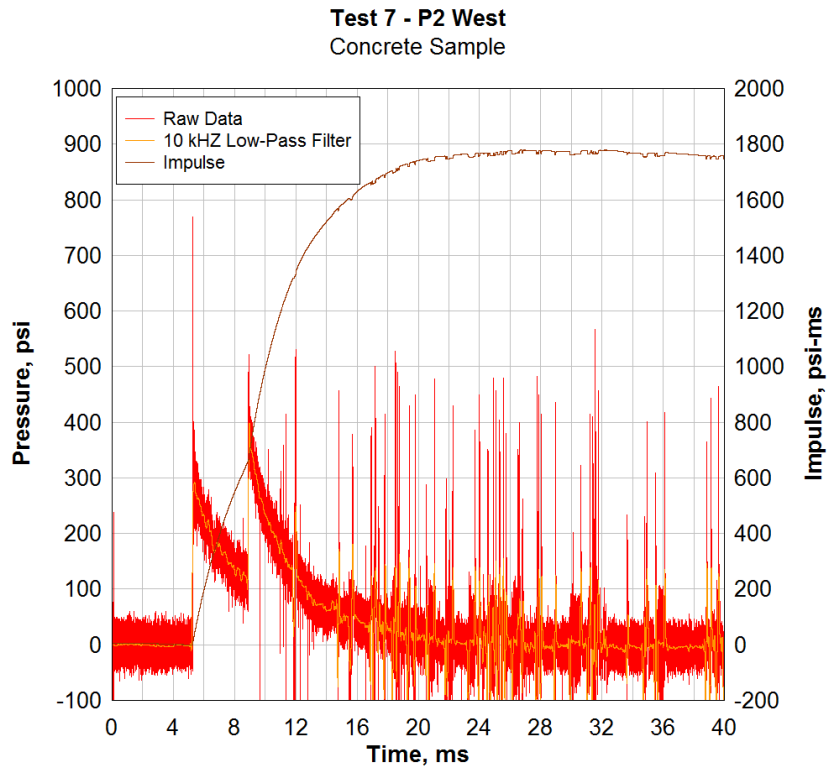

Figure 108. Test 7 P2 west pressure gage data.

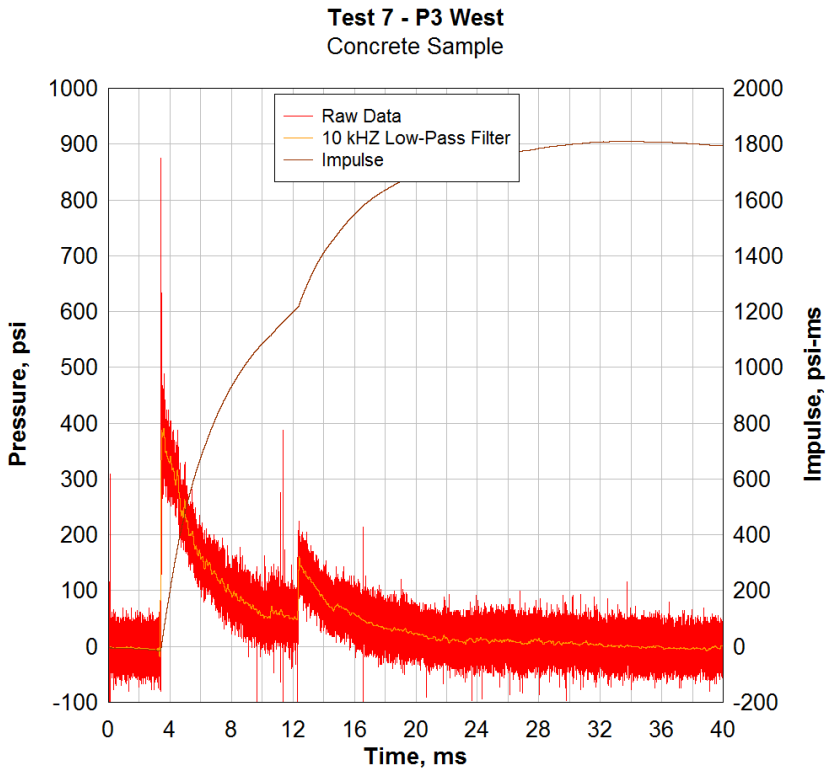

Figure 109. Test 7 P3 west pressure gage data.

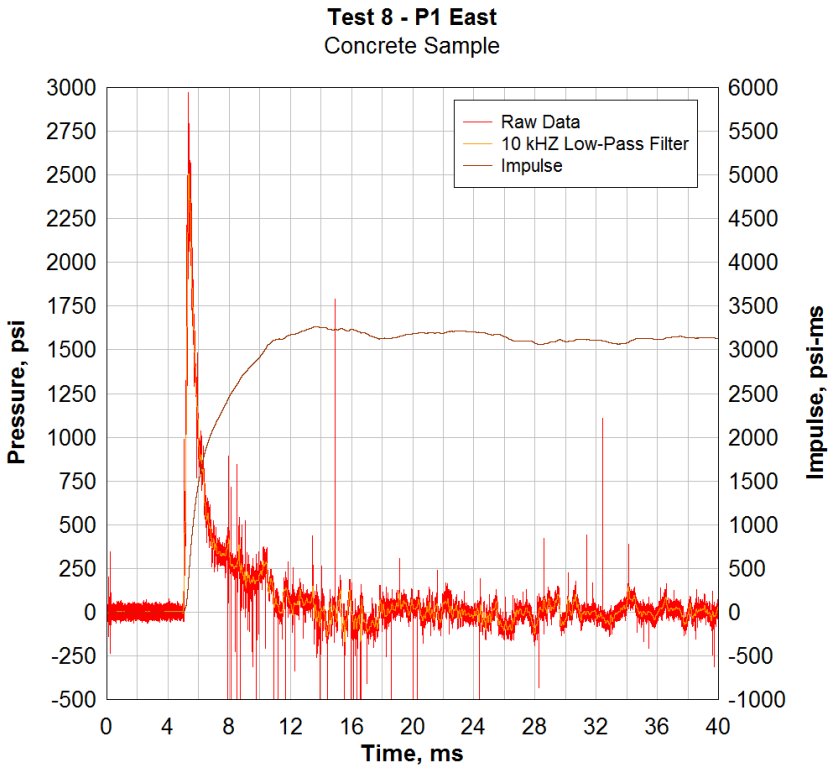

Figure 110. Test 8 P1 east pressure gage data.

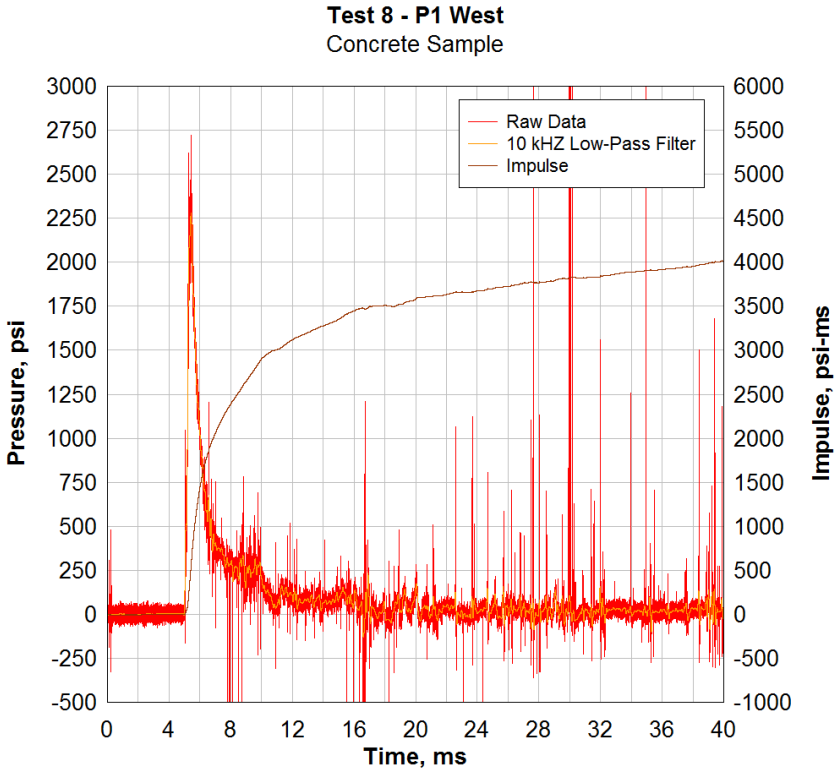

Figure 111. Test 8 P1 west pressure gage data.

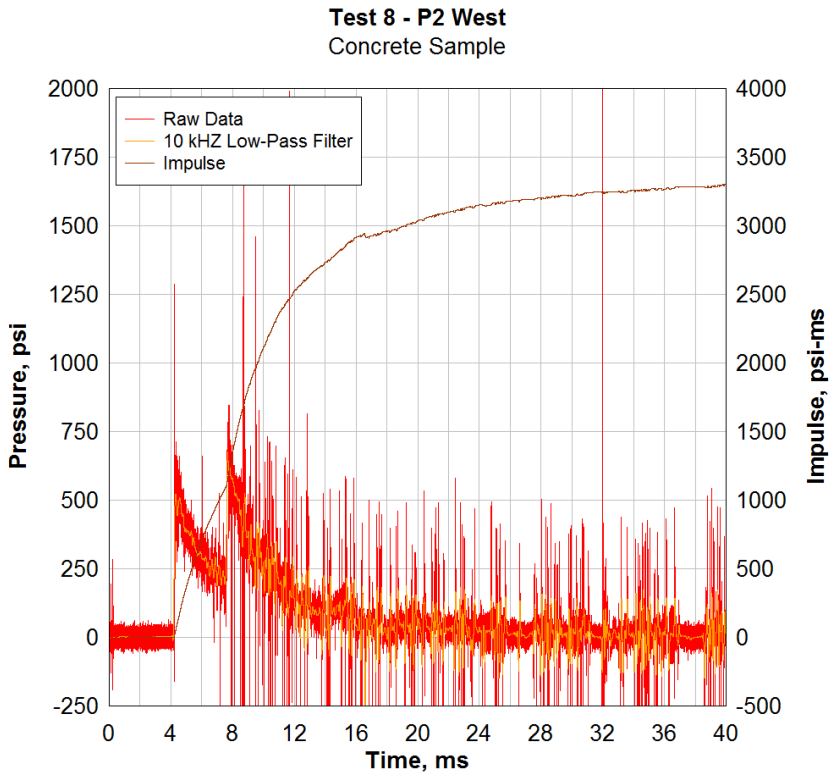

Figure 112. Test 8 P2 west pressure gage data.

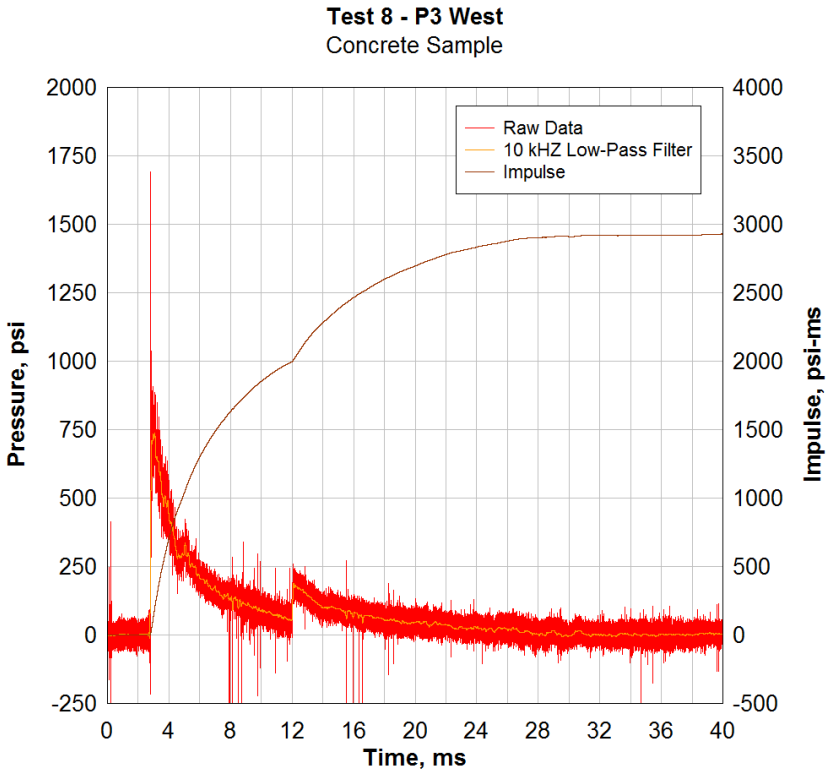

Figure 113. Test 8 P3 west pressure gage data.

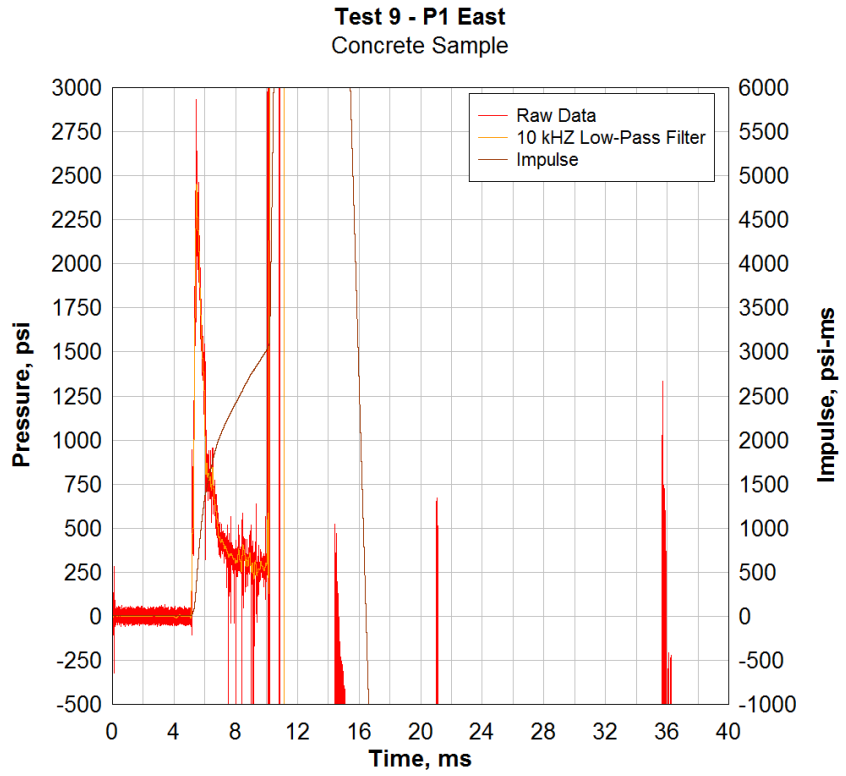

Figure 114. Test 9 P1 east pressure gage data.

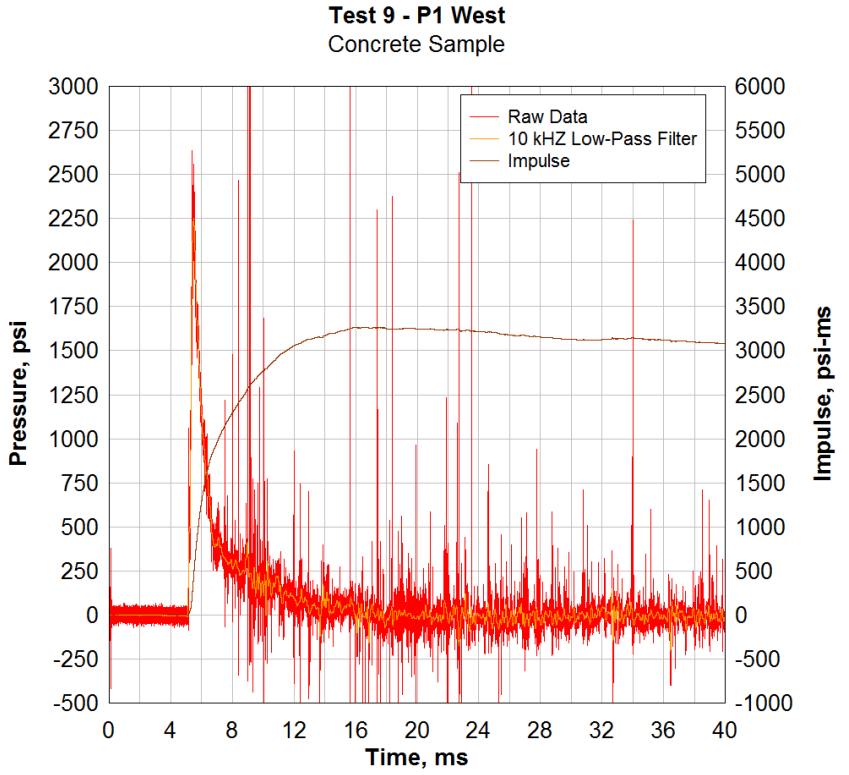

Figure 115. Test 9 P1 west pressure gage data.

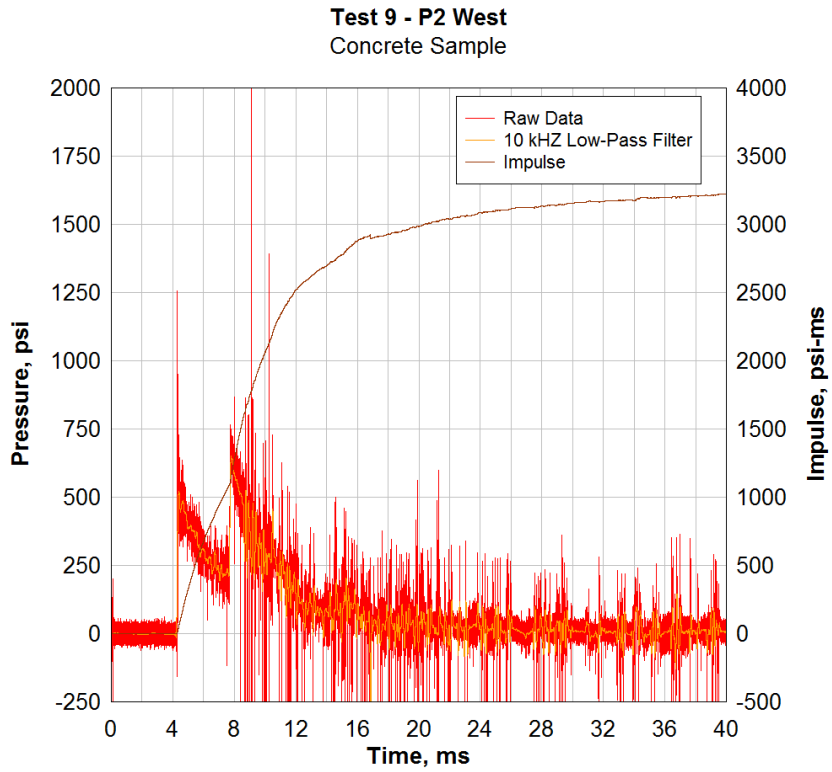

Figure 116. Test 9 P2 west pressure gage data.

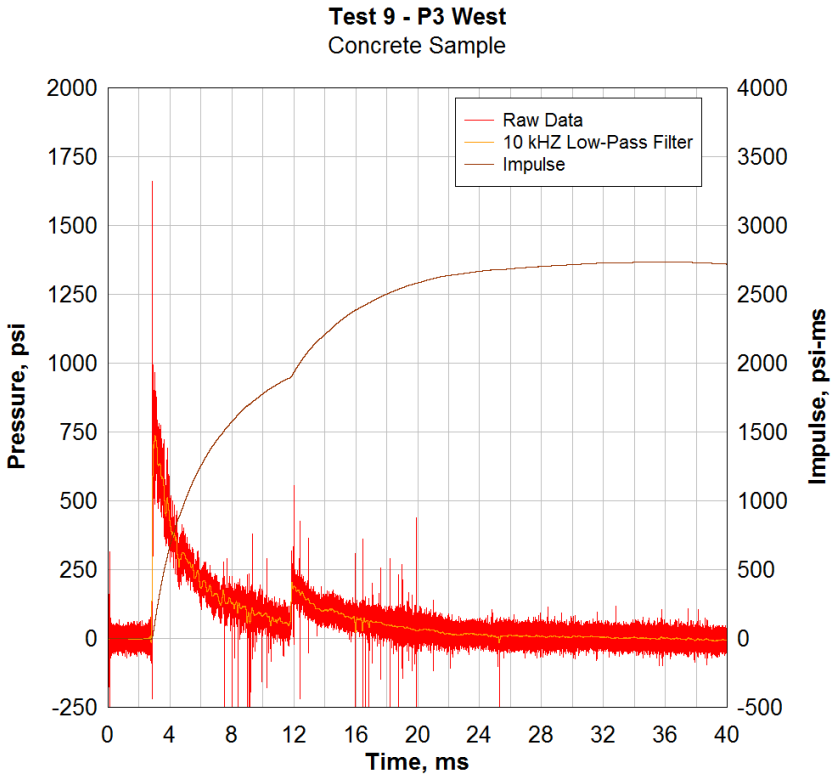

Figure 117. Test 9 P3 west pressure gage data.

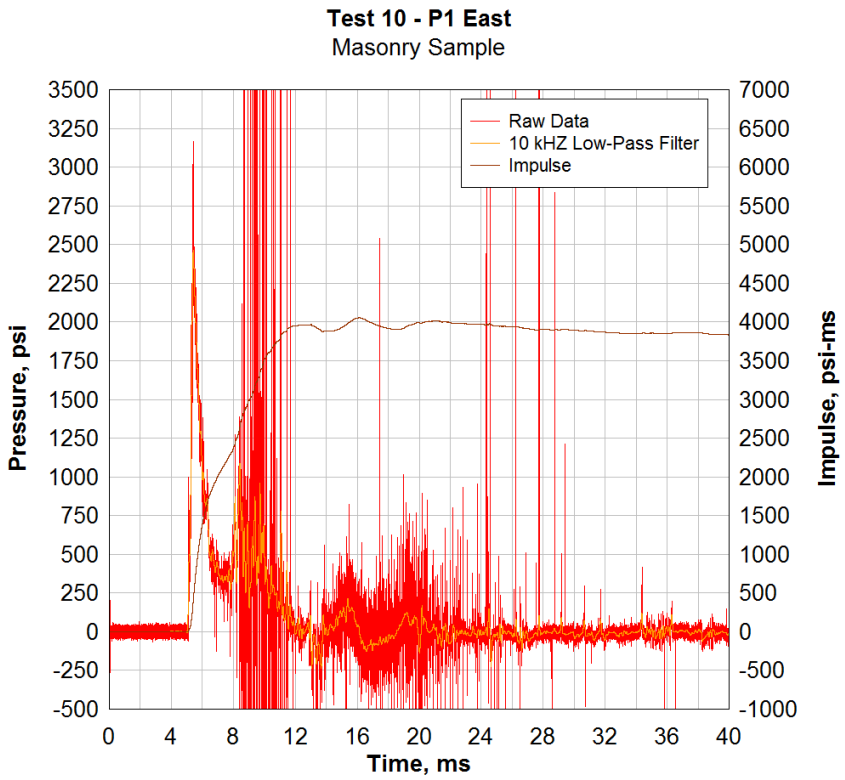

Figure 118. Test 10 P1 east pressure gage data.

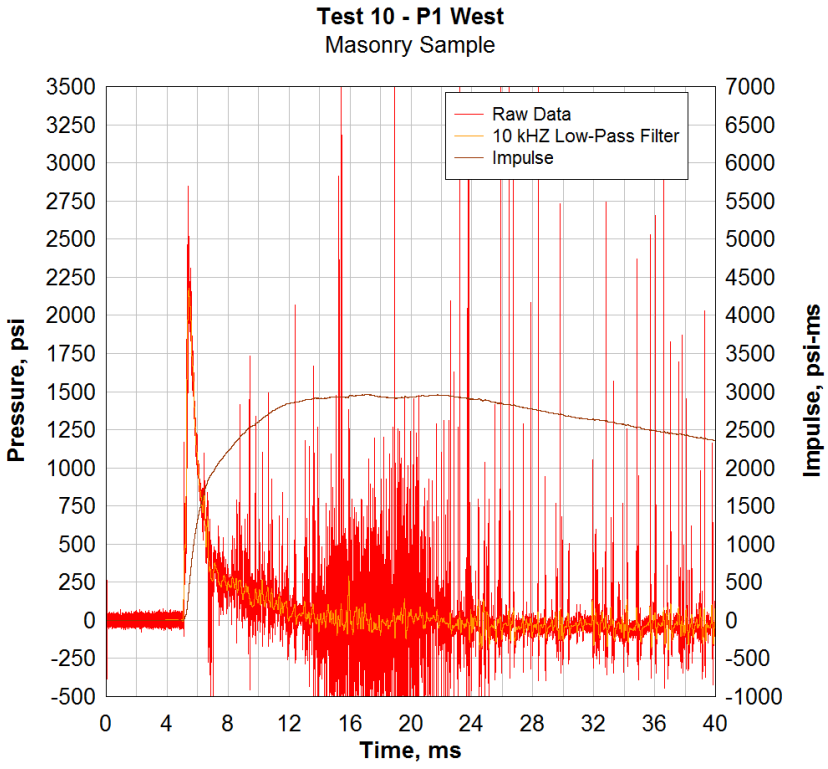

Figure 119. Test 10 P1 west pressure gage data.

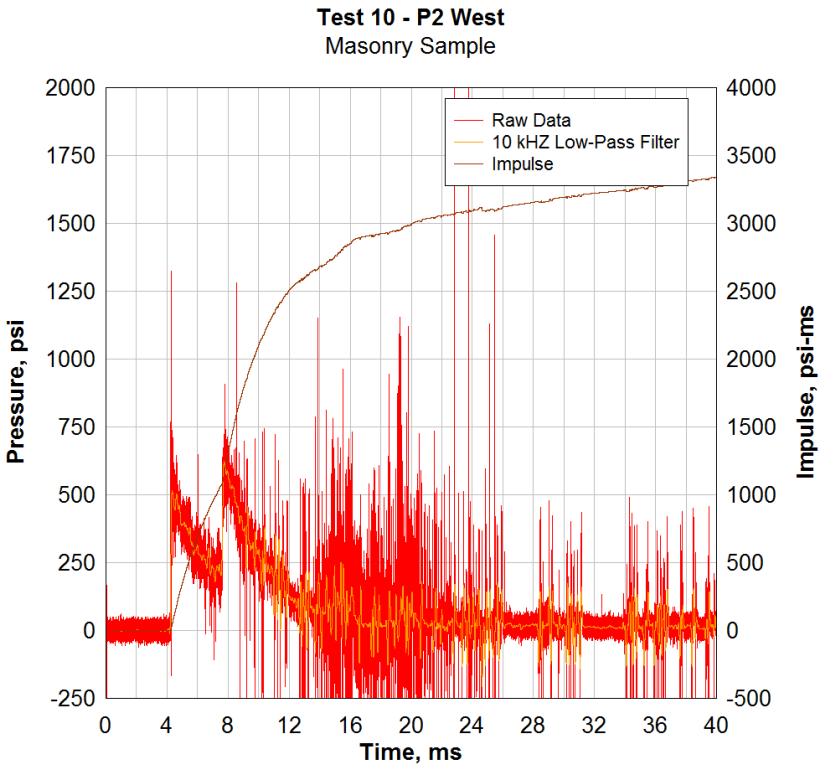

Figure 120. Test 10 P2 west pressure gage data.

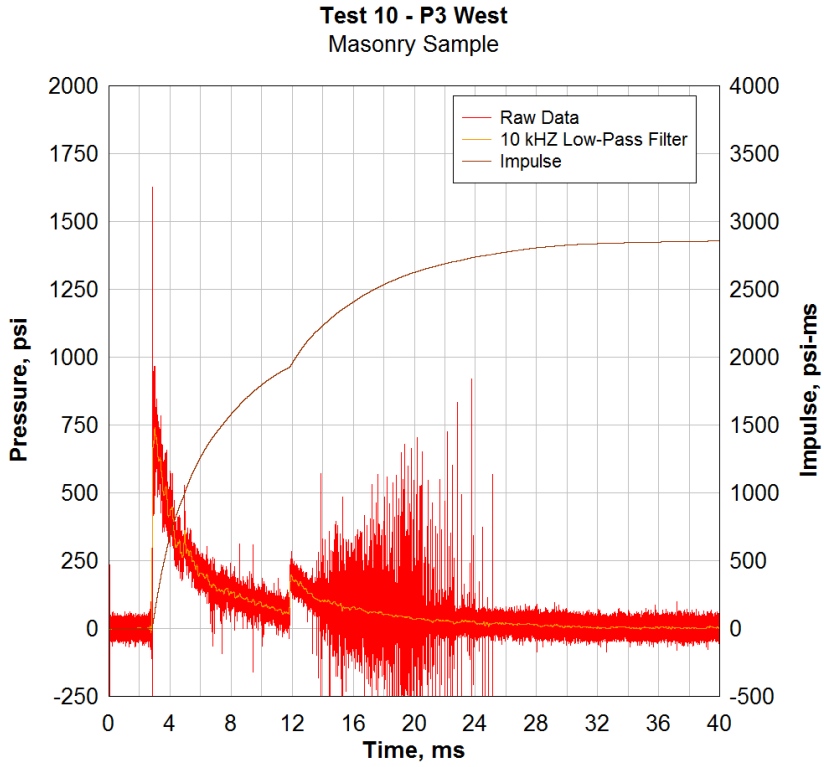

Figure 121. Test 10 P3 west pressure gage data.

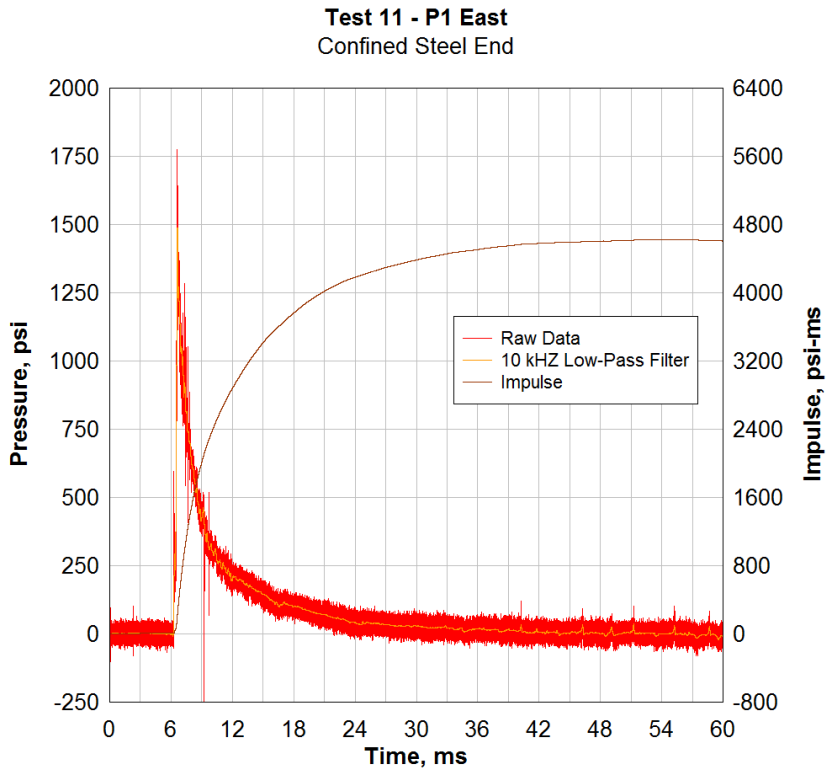

Figure 122. Test 11 P1 east pressure gage data.

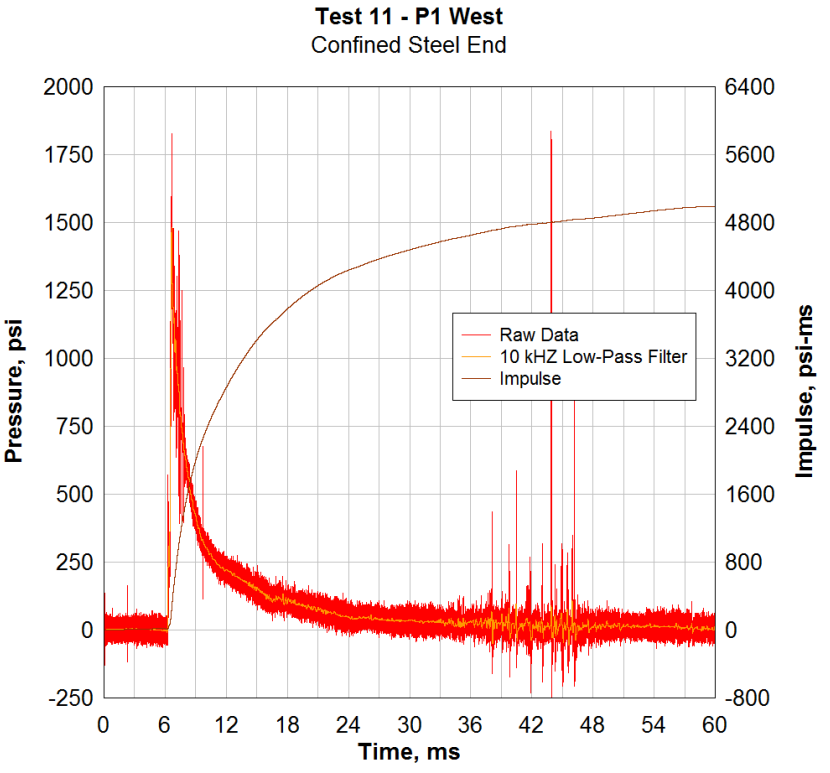

Figure 123. Test 11 P1 west pressure gage data.

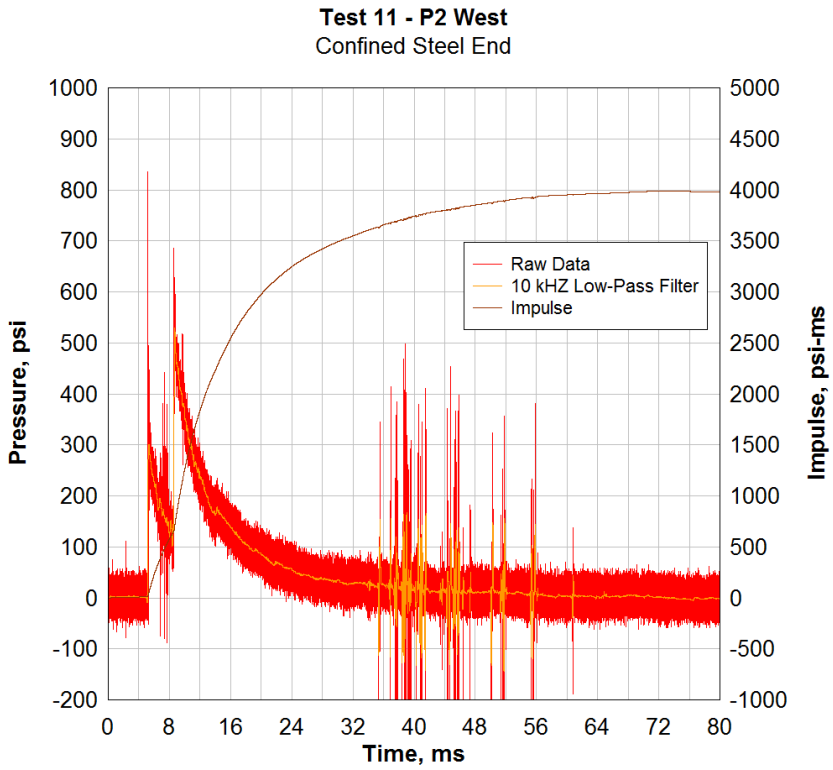

Figure 124. Test 11 P2 west pressure gage data.

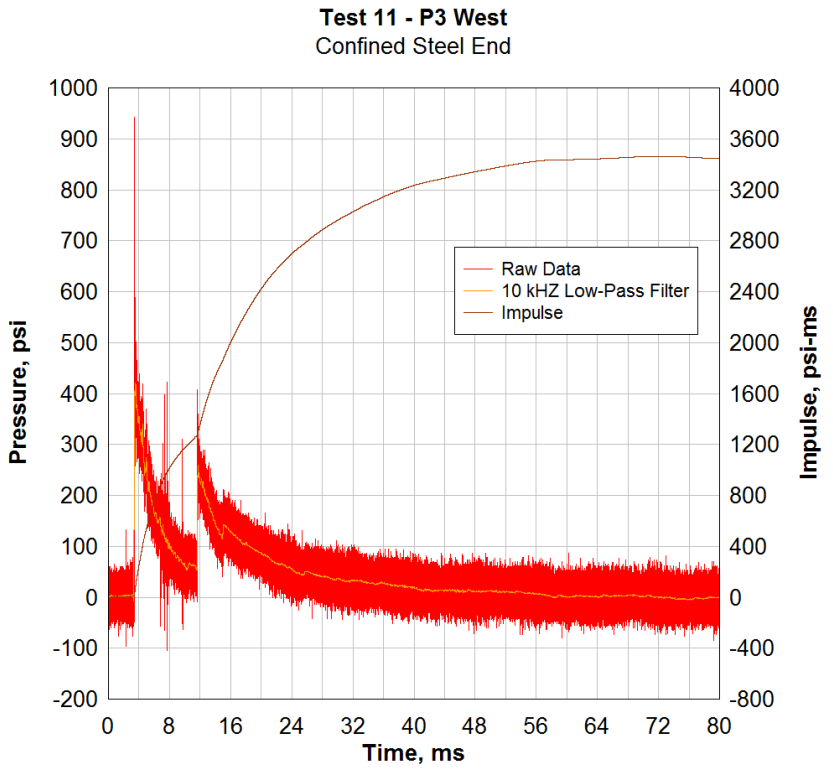

Figure 125. Test 11 P3 west pressure gage data.

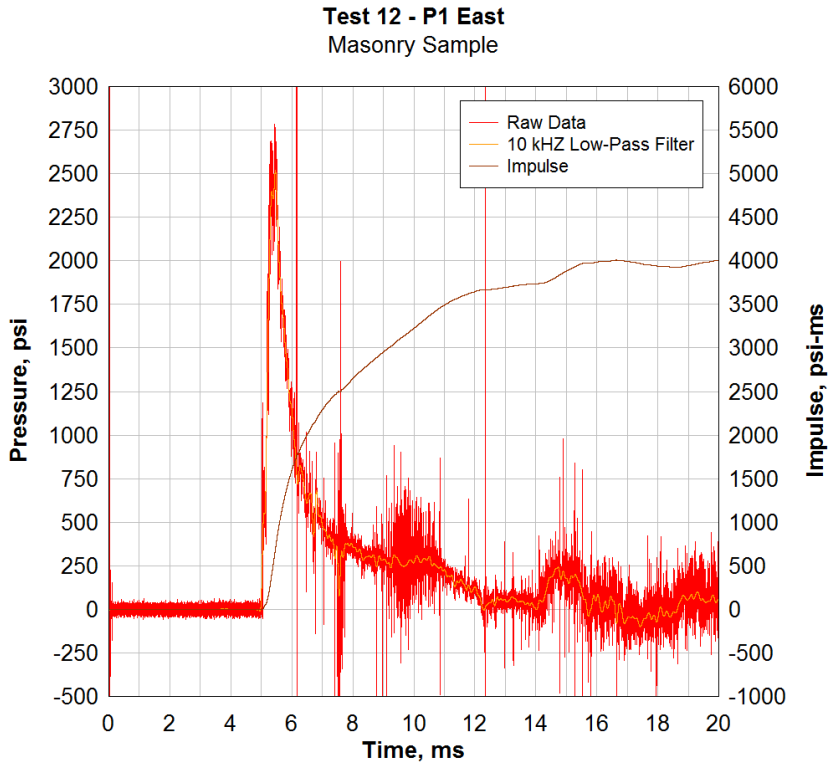

Figure 126. Test 12 P1 east pressure gage data.

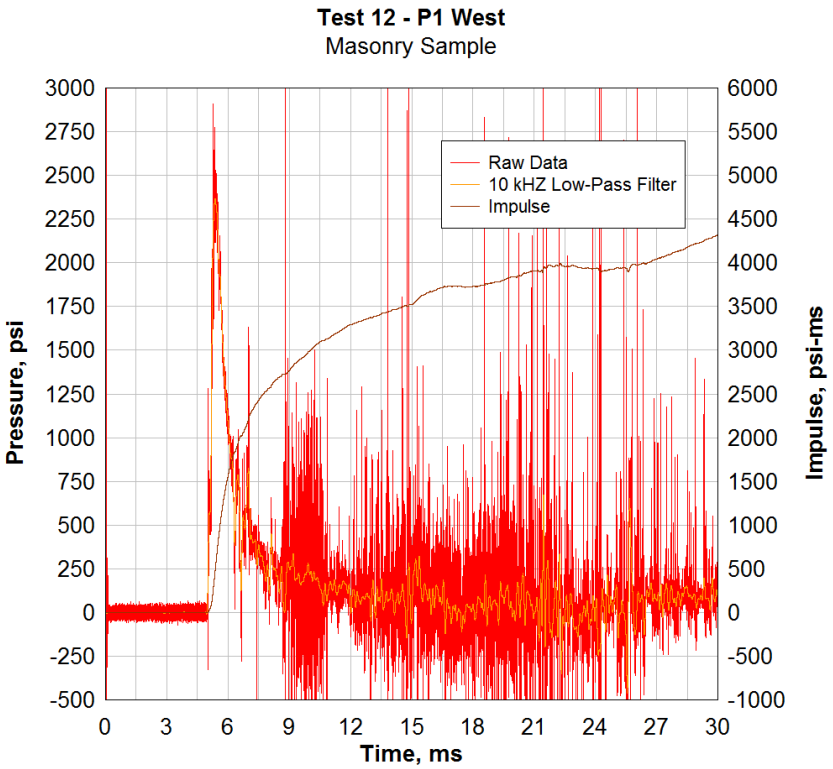

Figure 127. Test 12 P1 west pressure gage data.

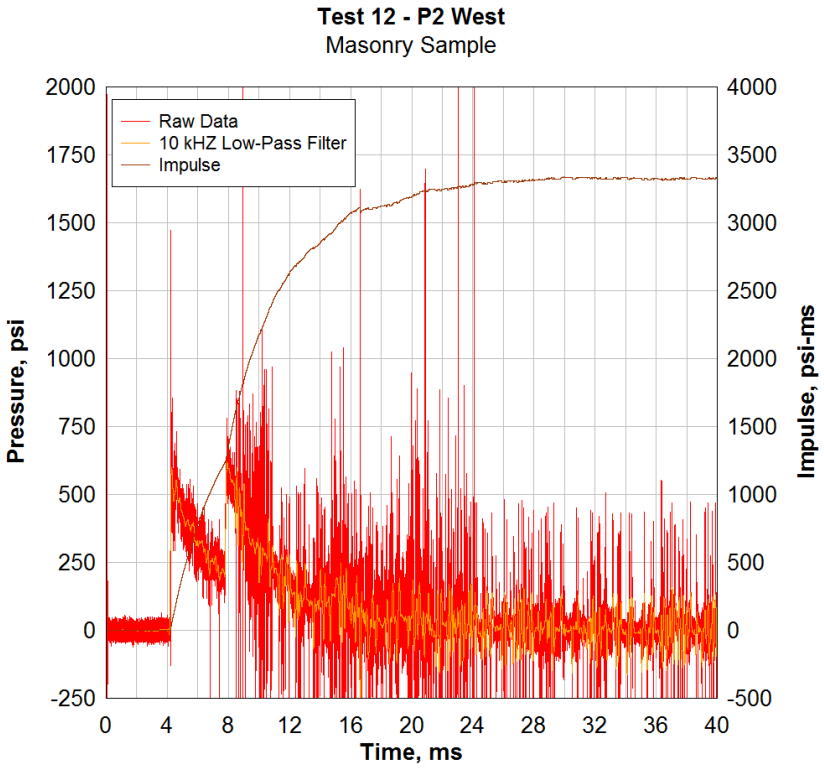

Figure 128. Test 12 P2 west pressure gage data.

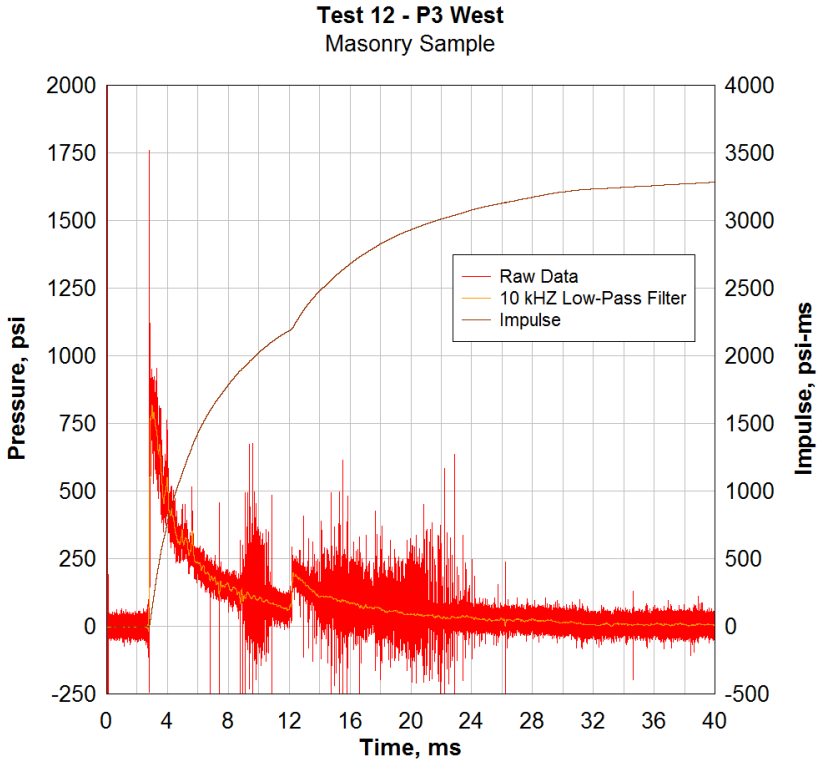

Figure 129. Test 12 P3 west pressure gage data.

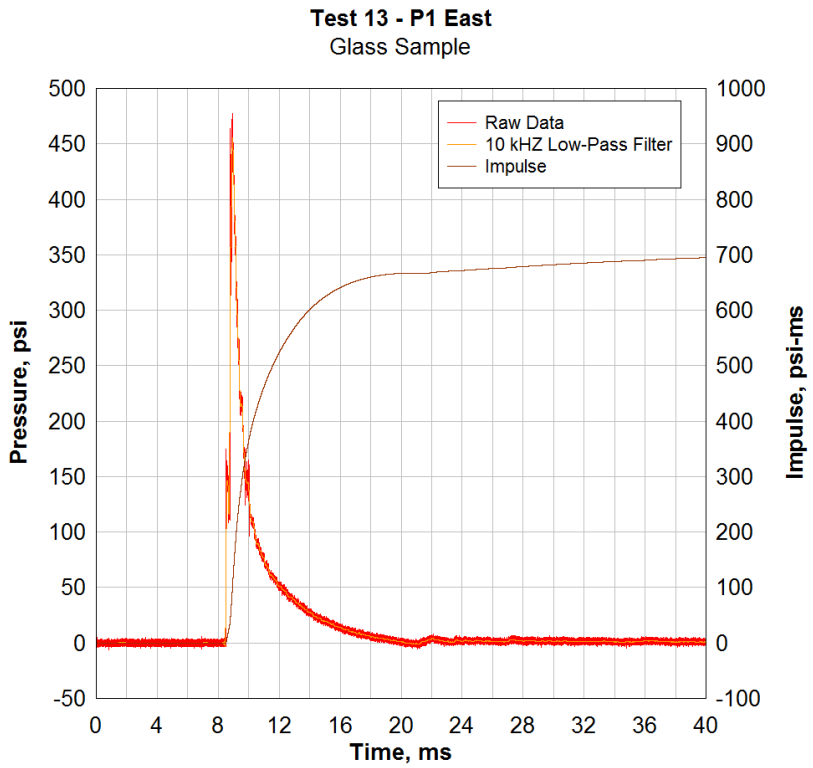

Figure 130. Test 13 P1 east pressure gage data.

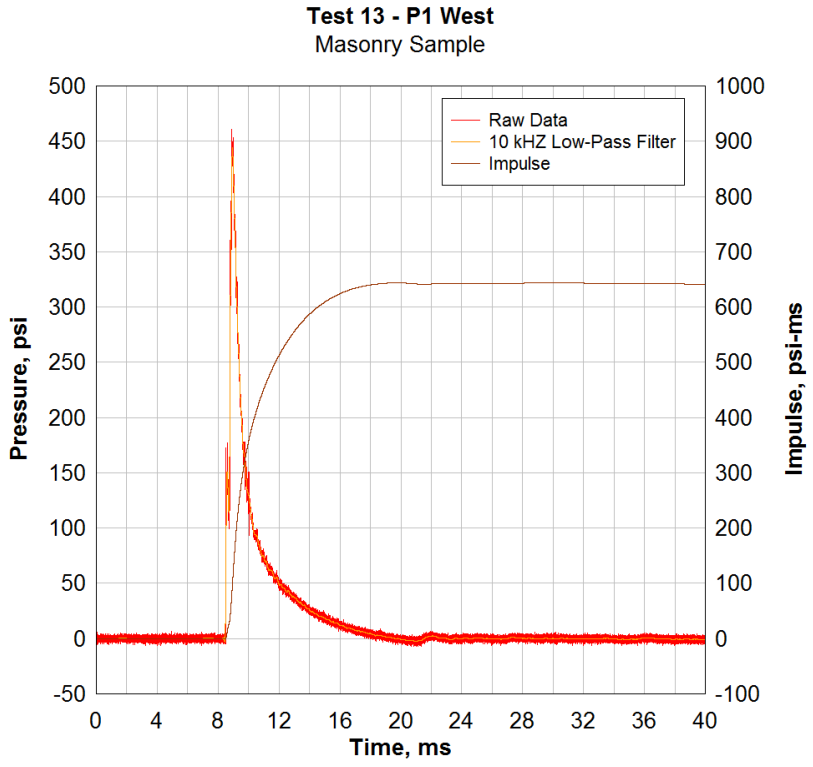

Figure 131. Test 13 P1 west pressure gage data.

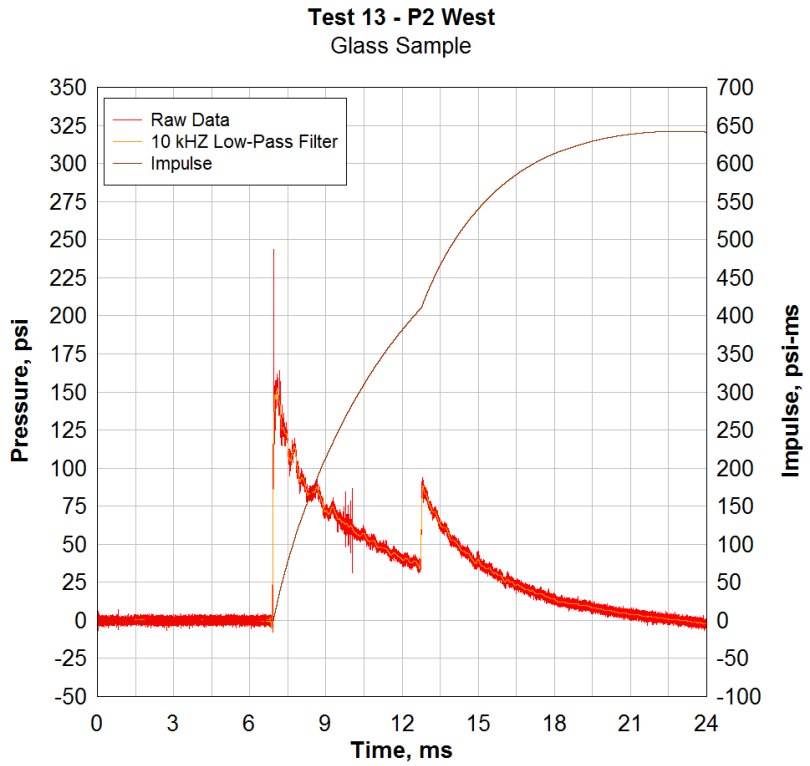

Figure 132. Test 13 P2 west pressure gage data.

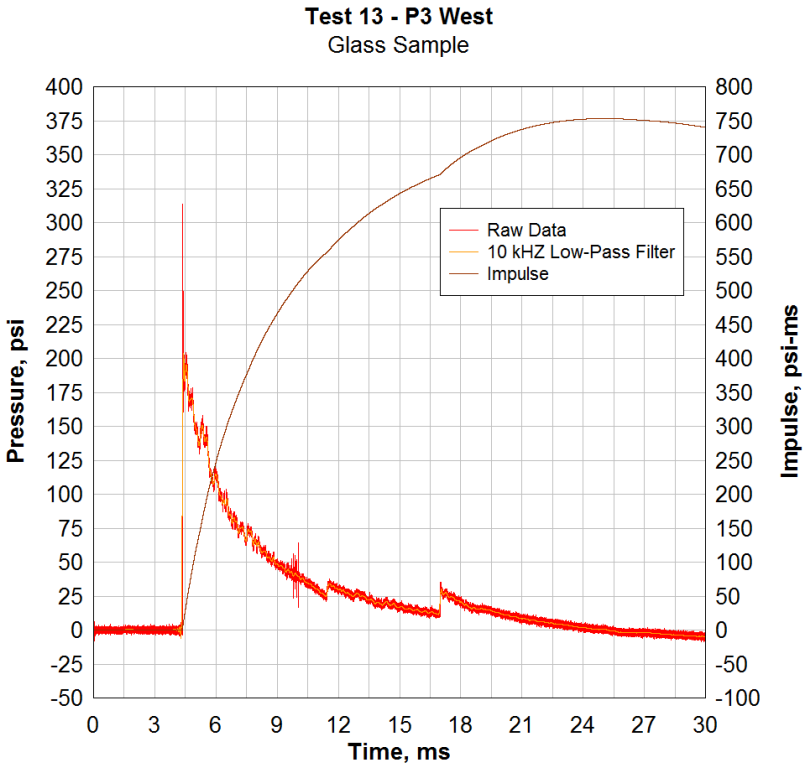

Figure 133. Test 13 P3 west pressure gage data.

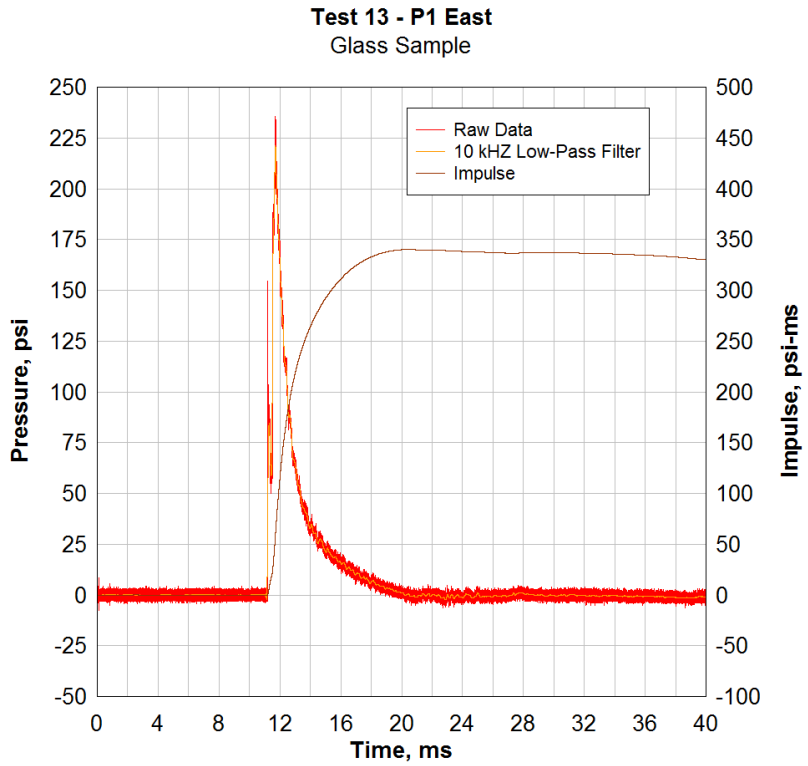

Figure 134. Test 14 P1 east pressure gage data.

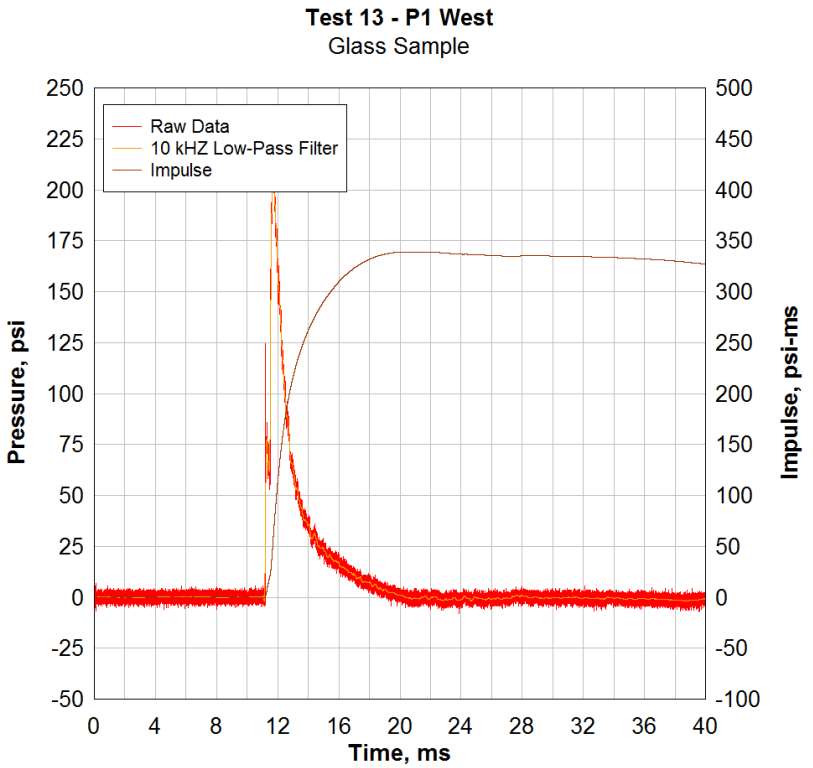

Figure 135. Test 14 P1 west pressure gage data.

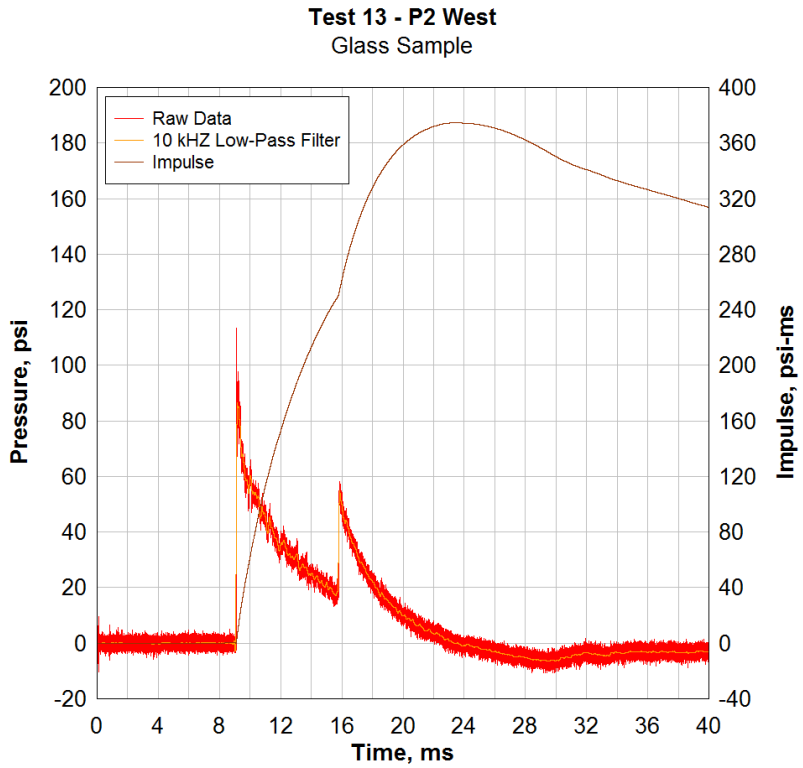

Figure 136. Test 14 P2 west pressure gage data.

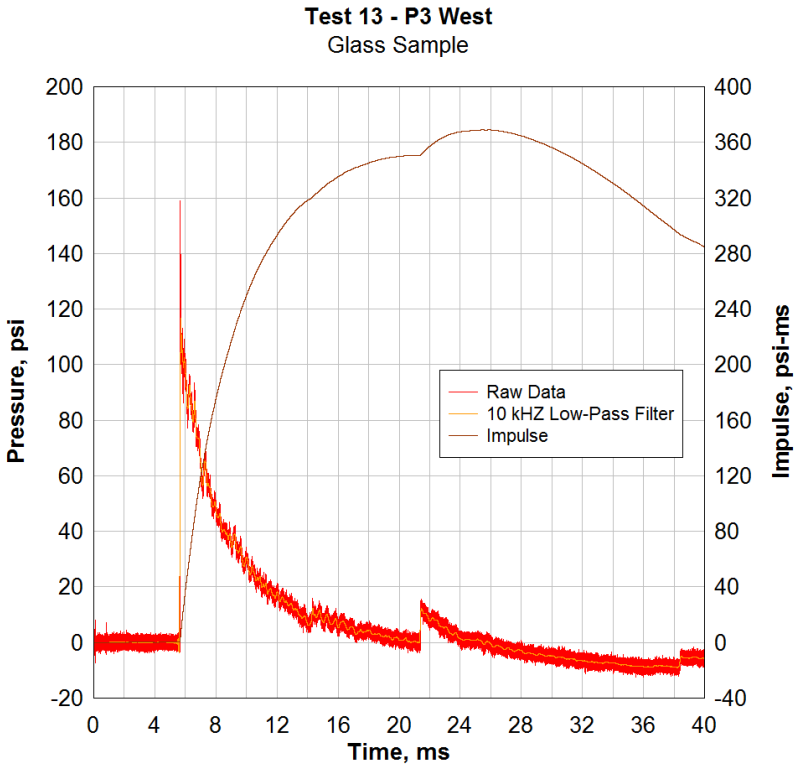

Figure 137. Test 14 P3 west pressure gage data.

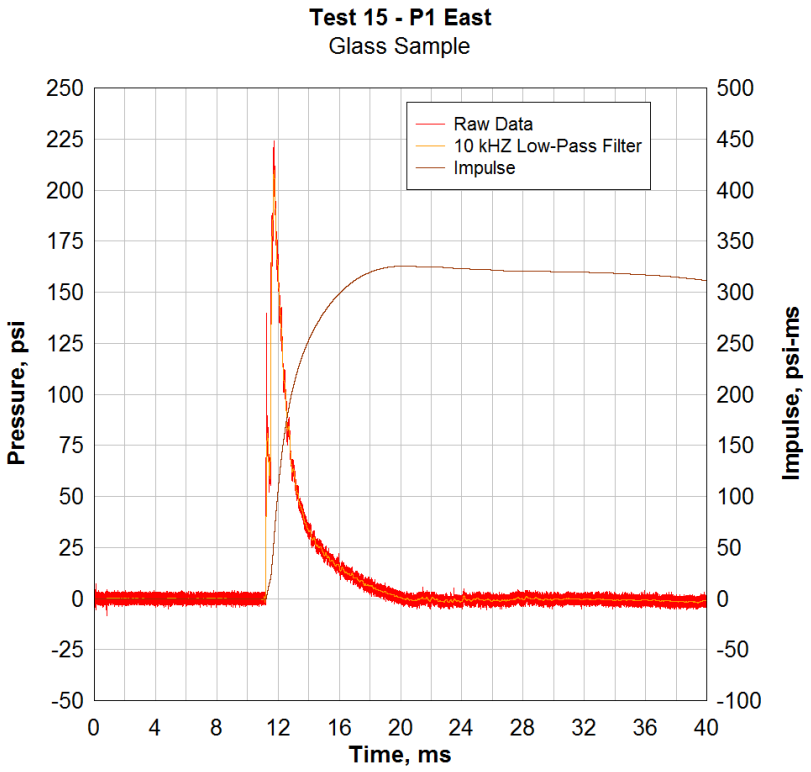

Figure 138. Test 15 P1 east pressure gage data.

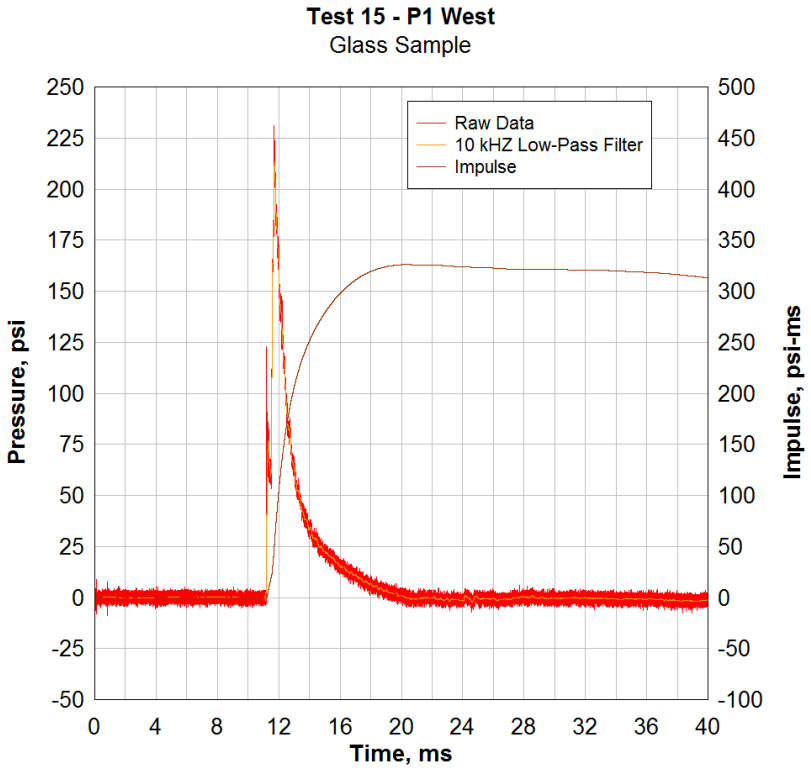

Figure 139. Test 15 P1 west pressure gage data.

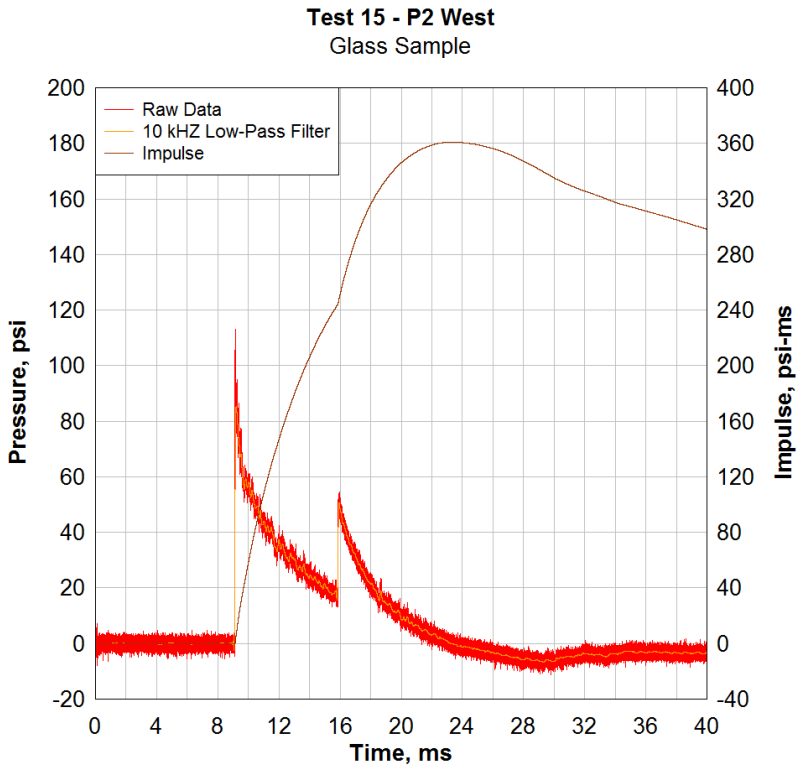

Figure 140. Test 15 P2 west pressure gage data.

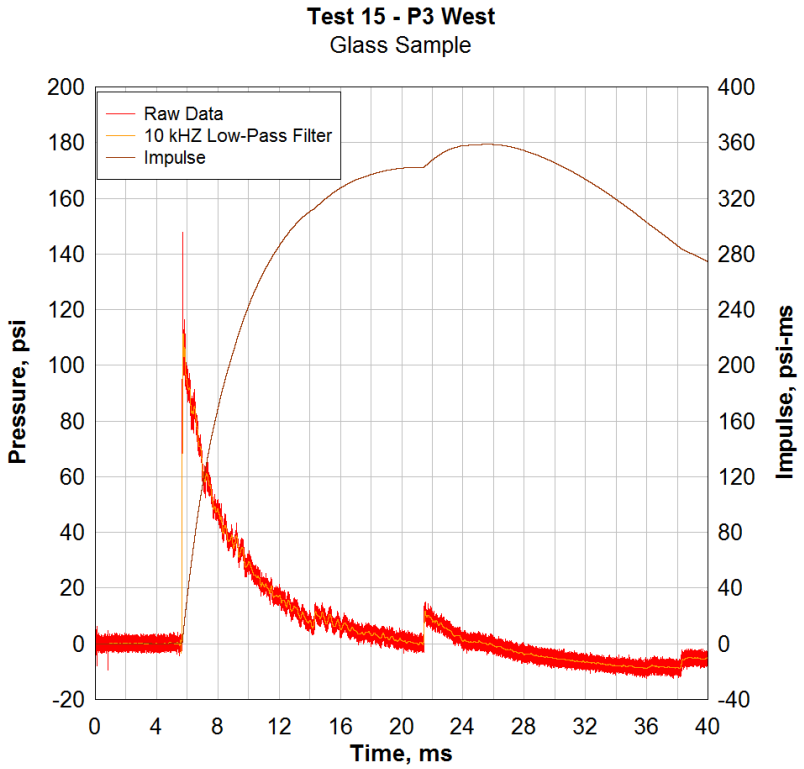

Figure 141. Test 15 P3 west pressure gage data.

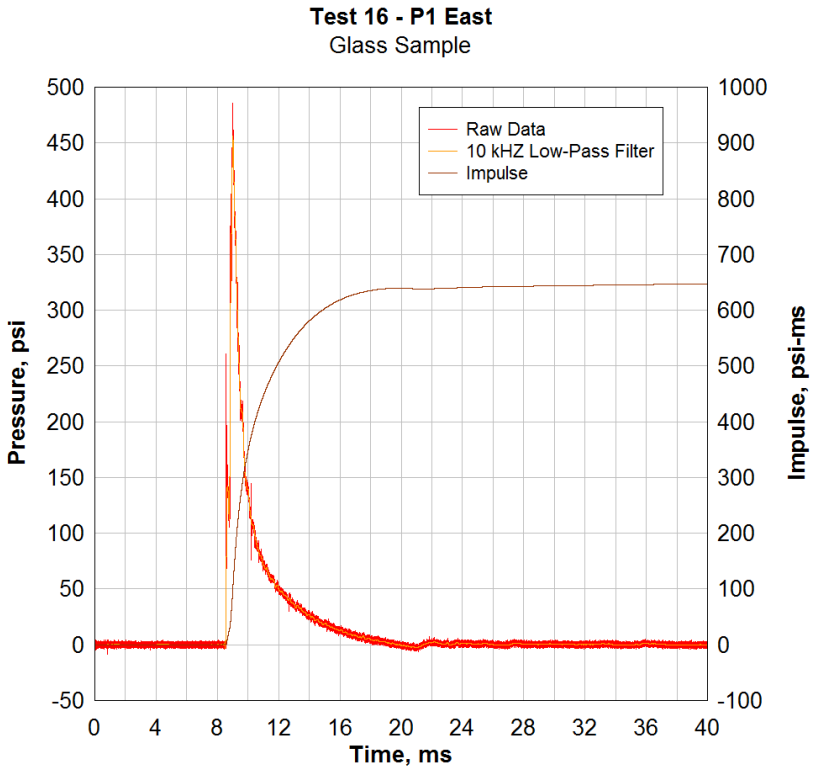

Figure 142. Test 16 P1 east pressure gage data.

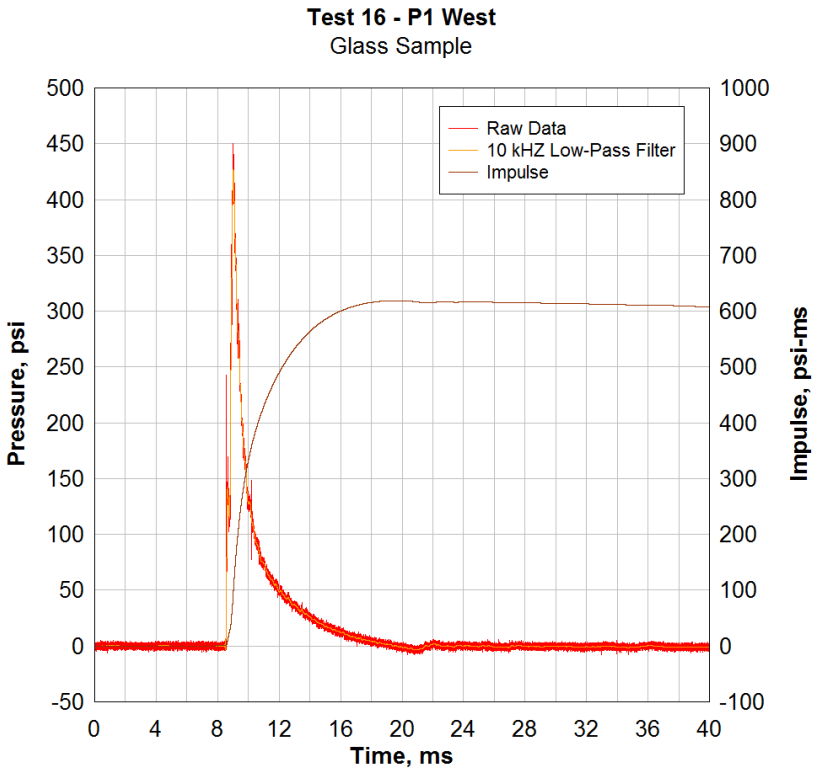

Figure 143. Test 16 P1 west pressure gage data.

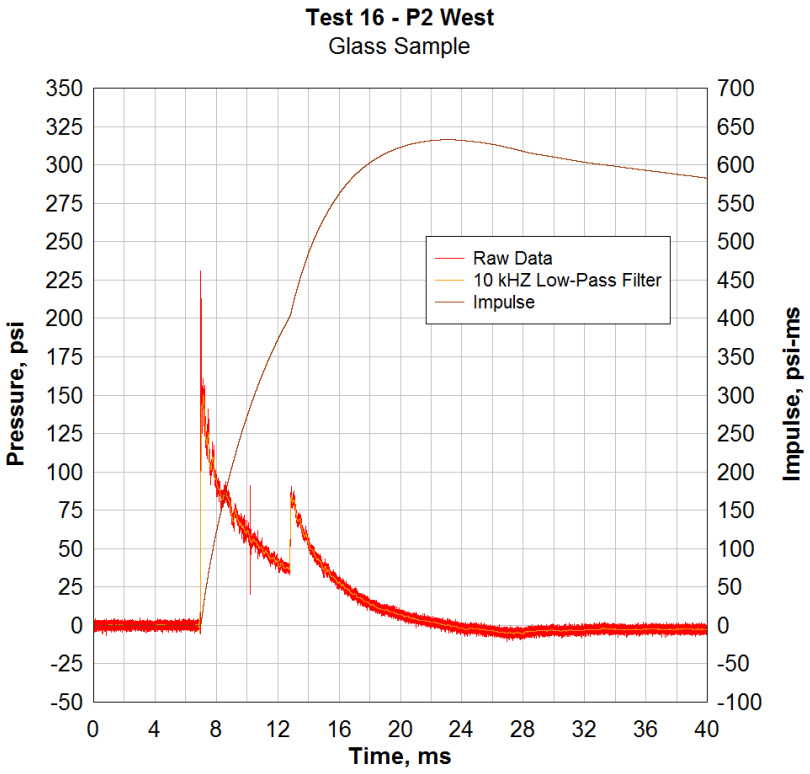

Figure 144. Test 16 P2 west pressure gage data.

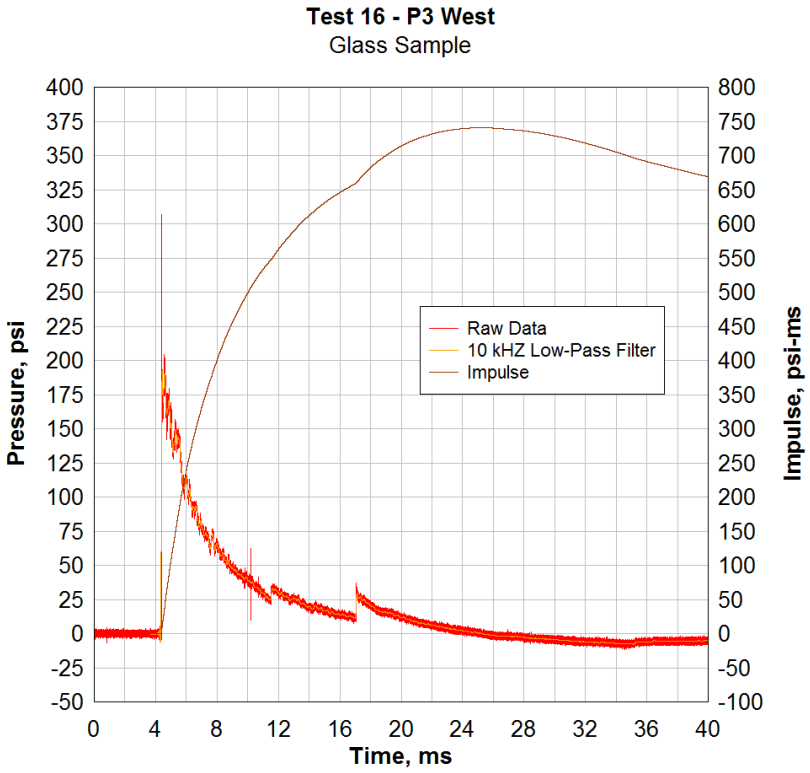

Figure 145. Test 16 P3 west pressure gage data.

DEPARTMENT OF DEFENSE

DEFENSE THREAT REDUCTION
AGENCY
8725 JOHN J. KINGMAN ROAD
STOP 6201
FORT BELVOIR, VA 22060
ATTN: MAJ J. REICHERT

DEFENSE TECHNICAL
INFORMATION CENTER
8725 JOHN J. KINGMAN ROAD,
SUITE 0944
FT. BELVOIR, VA 22060-6201
ATTN: DTIC/OCA

DEPARTMENT OF DEFENSE CONTRACTORS

QUANTERION SOLUTIONS, INC.
1680 TEXAS STREET, SE
KIRTLAND AFB, NM 87117-5669
ATTN: DTRIAC